STATE OF THE CLIMATE IN 2020

GLOBAL OCEANS

G. C. Johnson and R. Lumpkin, Eds.

Special Online Supplement to the *Bulletin of the American Meteorological Society* Vol.102, No. 8, August, 2021

https://doi.org/10.1175/ BAMS-D-21-0083.1
Corresponding author: Rick Lumpkin / rick.lumpkin@noaa.gov

STATE OF THE CLIMATE IN 2020
Global Oceans

Editors

Jessica Blunden
Tim Boyer

Chapter Editors

Freya Aldred
Peter Bissolli
Howard J. Diamond
Matthew L. Druckenmiller
Robert J. H. Dunn
Catherine Ganter
Nadine Gobron
Gregory C. Johnson
Tim Li
Rick Lumpkin
Ademe Mekonnen
John B. Miller
Twila A. Moon
Ahira Sánchez-Lugo
Ted A. Scambos
Carl J. Schreck III
Sharon Stammerjohn
Richard L. Thoman
Kate M. Willett

Technical Editor

Andrea Andersen

***BAMS* Special Editor for Climate**

Michael A. Alexander

American Meteorological Society

Cover credit:
Oil bar and pencil on mat board

Original artwork by Gregory C. Johnson–chapter co-editor

Global Oceans is a chapter from the *State of the Climate in 2020* annual report. This chapter is available from https://doi.org/10.1175/ BAMS-D-21-0083.1. Compiled by NOAA's National Centers for Environmental Information, *State of the Climate in 2020* is based on contributions from scientists from around the world. It provides a detailed update on global climate indicators, notable weather events, and other data collected by environmental monitoring stations and instruments located on land, water, ice, and in space. The full report is available from: https://doi.org/10.1175/2021BAMSStateoftheClimate.1.

How to cite this document:

Citing the complete report:
Blunden, J. and T. Boyer, Eds., 2021: "State of the Climate in 2020". *Bull. Amer. Meteor. Soc.*, **102** (8), Si–S475, https://doi.org/10.1175/2021BAMSStateoftheClimate.1.

Citing this chapter:
Johnson, G. C. and R. L. Lumpkin, Eds., 2021: Global Oceans [in "State of the Climate in 2020"]. *Bull. Amer. Meteor. Soc.*, **102** (8), S143–S198, https://doi.org/10.1175/ BAMS-D-21-0083.1.

Citing a section (example):
Yu, L., P. W. Stackhouse, A. C. Wilber, C. Wen, and R. A. Weller, 2021: Global ocean heat, freshwater, and momentum fluxes [in "State of the Climate in 2020"]. *Bull. Amer. Meteor. Soc.*, **102** (8), S164–S169, https://doi.org/10.1175/ BAMS-D-21-0083.1.

Editor and Author Affiliations (alphabetical by name)

Alin, Simone R., NOAA/OAR Pacific Marine Environmental Laboratory, Seattle, Washington

Amaya, Dillon J., Cooperative Institute for Research in Environmental Sciences, University of Colorado, Boulder, Colorado

Baringer, Molly O., NOAA/OAR Atlantic Oceanographic and Meteorological Laboratory, Miami, Florida

Boyer, Tim, NOAA/NESDIS National Centers for Environmental Information, Silver Spring, Maryland

Brandt, Peter, GEOMAR Helmholtz Centre for Ocean Research Kiel, Kiel, Germany

Carter, Brendan R., Cooperative Institute for Climate, Ocean, and Ecosystem Studies, University of Washington, Seattle, Washington; NOAA/OAR Pacific Marine Environmental Laboratory, Seattle, Washington

Cetinić, Ivona, NASA Goddard Space Flight Center, Greenbelt, Maryland; Universities Space Research Association, Columbia, Maryland

Chambers, Don P., College of Marine Science, University of South Florida, St. Petersburg, Florida

Cheng, Lijing, International Center for Climate and Environment Sciences, Institute of Atmospheric Physics, Chinese Academy of Sciences, Beijing, China

Collins, Andrew U., Cooperative Institute for Climate, Ocean, and Ecosystem Studies, Seattle, Washington, University of Washington,

Cosca, Cathy, NOAA/OAR Pacific Marine Environmental Laboratory, Seattle, Washington

Domingues, Ricardo, Cooperative Institute for Marine and Atmospheric Studies, University of Miami, Miami, Florida; NOAA/OAR Atlantic Oceanographic and Meteorological Laboratory, Miami, Florida

Dong, Shenfu, NOAA/OAR Atlantic Oceanographic and Meteorological Laboratory, Miami, Florida

Feely, Richard A., NOAA/OAR Pacific Marine Environmental Laboratory, Seattle, Washington

Frajka-Williams, Eleanor, National Oceanography Centre, United Kingdom

Franz, Bryan A., NASA Goddard Space Flight Center, Greenbelt, Maryland

Gilson, John, Scripps Institution of Oceanography, University of California San Diego, La Jolla, California

Goni, Gustavo, NOAA/OAR Atlantic Oceanographic and Meteorological Laboratory, Miami, Florida

Hamlington, Benjamin D., Center for Coastal Physical Oceanography, Old Dominion University, Norfolk, Virginia

Herrford, Josefine, GEOMAR Helmholtz Centre for Ocean Research Kiel, Kiel, Germany

Hu, Zeng-Zhen, NOAA/NWS NCEP Climate Prediction Center, College Park, Maryland

Huang, Boyin, NOAA/NESDIS National Centers for Environmental Information, Asheville, North Carolina

Ishii, Masayoshi, Department of Atmosphere, Ocean and Earth System Modeling Research, Meteorological Research Institute, Japan Meteorological Agency, Tsukuba, Japan

Jevrejeva, Svetlana, National Oceanography Centre, Liverpool, United Kingdom

Johnson, Gregory C., NOAA/OAR Pacific Marine Environmental Laboratory, Seattle, Washington

Kennedy, John J., Met Office Hadley Centre, Exeter, United Kingdom

Kersalé, Marion, Cooperative Institute for Marine and Atmospheric Studies, University of Miami, Miami, Florida; NOAA/OAR Atlantic Oceanographic and Meteorological Laboratory, Miami, Florida

Killick, Rachel E., Met Office Hadley Centre, Exeter, United Kingdom

Landschützer, Peter, Max Planck Institute for Meteorology, Hamburg, Germany

Lankhorst, Matthias, Scripps Institution of Oceanography, University of California San Diego, La Jolla, California

Leuliette, Eric, NOAA/NWS NCWCP Laboratory for Satellite Altimetry, College Park, Maryland

Locarnini, Ricardo, NOAA/NESDIS National Centers for Environmental Information, Silver Spring, Maryland

Lumpkin, Rick, NOAA/OAR Atlantic Oceanographic and Meteorological Laboratory, Miami, Florida

Lyman, John M., Joint Institute for Marine and Atmospheric Research, University of Hawaii, Honolulu, Hawaii; NOAA/OAR Pacific Marine Environmental Laboratory, Seattle, Washington

Marra, John J., NOAA/NESDIS National Centers for Environmental Information, Honolulu, Hawaii

Meinen, Christopher S., NOAA/OAR Atlantic Oceanographic and Meteorological Laboratory, Miami, Florida

Merrifield, Mark A., Joint Institute for Marine and Atmospheric Research, University of Hawaii, Honolulu, Hawaii

Mitchum, Gary T., College of Marine Science, University of South Florida, St. Petersburg, Florida

Moat, Ben I., National Oceanography Centre, United Kingdom

Nerem, R. Steven, Colorado Center for Astrodynamics Research, Cooperative Institute for Research in Environmental Sciences, University of Colorado Boulder, Boulder, Colorado

Perez, Renellys C., NOAA/OAR Atlantic Oceanographic and Meteorological Laboratory, Miami, Florida

Purkey, Sarah G., Scripps Institution of Oceanography, University of California San Diego, La Jolla, California

Reagan, James, Earth System Science Interdisciplinary Center/Cooperative Institute for Satellite Earth System Studies–Maryland, University of Maryland, College Park, Maryland; NOAA/NESDIS National Centers for Environmental Information, Silver Spring, Maryland

Sanchez-Franks, Alejandra, National Oceanography Centre, United Kingdom

Scannell, Hillary A., Lamont-Doherty Earth Observatory, Columbia University, Palisades, New York

Schmid, Claudia, NOAA/OAR Atlantic Oceanographic and Meteorological Laboratory, Miami, Florida

Scott, Joel P., NASA Goddard Space Flight Center, Greenbelt, Maryland; Science Application International Corporation, Reston, Virginia

Siegel, David A., University of California–Santa Barbara, Santa Barbara, California

Smeed, David A., National Oceanography Centre, United Kingdom

Stackhouse, Paul W., NASA Langley Research Center, Hampton, Virginia

Sweet, William, NOAA/NOS Center for Operational Oceanographic Products and Services, Silver Spring, Maryland

Thompson, Philip R., Joint Institute for Marine and Atmospheric Research, University of Hawaii, Honolulu, Hawaii

Triñanes, Joaquin A., Laboratory of Systems, Technological Research Institute, Universidad de Santiago de Compostela, Santiago de Compostela, Spain; Cooperative Institute for Marine and Atmospheric Studies, University of Miami; NOAA/OAR Atlantic Oceanographic and Meteorological Laboratory, Miami, Florida

Volkov, Denis L., Cooperative Institute for Marine and Atmospheric Studies, University of Miami, Miami, Florida; NOAA/OAR Atlantic Oceanographic and Meteorological Laboratory, Miami, Florida

Wanninkhof, Rik, NOAA/OAR Atlantic Oceanographic and Meteorological Laboratory, Miami, Florida

Weller, Robert A., Woods Hole Oceanographic Institution, Woods Hole, Massachusetts

Editor and Author Affiliations (alphabetical by name)

Wen, Caihong, NOAA/NWS NCEP Climate Prediction Center, College Park, Maryland
Westberry, Toby K., Oregon State University, Corvallis, Oregon
Widlansky, Matthew J., Joint Institute for Marine and Atmospheric Research, University of Hawaii, Honolulu, Hawaii
Wilber, Anne C., Science Systems and Applications, Inc., Hampton, Virginia
Yu, Lisan, Woods Hole Oceanographic Institution, Woods Hole, Massachusetts
Zhang, Huai-Min, NOAA/NESDIS National Centers for Environmental Information, Asheville, North Carolina

Editorial and Production Team

Allen, Jessicca, Graphics Support, Cooperative Institute for Satellite Earth System Studies, North Carolina State University, Asheville, North Carolina
Andersen, Andrea, Technical Editor, TeleSolv Consulting LLC, NOAA/NESDIS National Centers for Environmental Information, Asheville, North Carolina
Hammer, Gregory, Content Team Lead, Communications and Outreach, NOAA/NESDIS National Centers for Environmental Information, Asheville, North Carolina
Love-Brotak, S. Elizabeth, Lead Graphics Production, NOAA/NESDIS National Centers for Environmental Information, Asheville, North Carolina
Misch, Deborah J., Graphics Support, Innovative Consulting & Management Services, LLC, NOAA/NESDIS National Centers for Environmental Information, Asheville, North Carolina
Riddle, Deborah B., Graphics Support, NOAA/NESDIS National Centers for Environmental Information, Asheville, North Carolina
Veasey, Sara W., Visual Communications Team Lead, Communications and Outreach, NOAA/NESDIS National Centers for Environmental Information, Asheville, North Carolina

3. Table of Contents

*Please refer to Chapter 8 (Relevant datasets and sources) for a list of all climate variables and datasets used in this chapter for analyses, along with their websites for more information and access to the data.

3. GLOBAL OCEANS

G. C. Johnson and R. Lumpkin, Eds.

a. Overview—G. C. Johnson and R. Lumpkin

This chapter details 2020 global patterns in select observed oceanic physical, chemical, and biological variables relative to long-term climatologies, their differences between 2020 and 2019, and puts 2020 observations in the context of the historical record. In this overview we address a few of the highlights, first in haiku, then paragraph form:

La Niña arrives,
shifts winds, rain, heat, salt, carbon:
Pacific—beyond.

Global ocean conditions in 2020 reflected a transition from an El Niño in 2018–19 to a La Niña in late 2020. Pacific trade winds strengthened in 2020 relative to 2019, driving anomalously westward Pacific equatorial surface currents. Sea surface temperatures (SSTs), upper ocean heat content, and sea surface height all fell in the eastern tropical Pacific and rose in the western tropical Pacific. Efflux of carbon dioxide from ocean to atmosphere was larger than average across much of the equatorial Pacific, and both chlorophyll-a and phytoplankton carbon concentrations were elevated across the tropical Pacific. Less rain fell and more water evaporated in the western equatorial Pacific, consonant with increased sea surface salinity (SSS) there. SSS may also have increased as a result of anomalously westward surface currents advecting salty water from the east. El Niño–Southern Oscillation conditions have global ramifications that reverberate throughout the report.

Marine heatwave strikes
northeast Pacific again,
twice in past decade

Anomalously warm SSTs were especially prominent and persistent in the northeast Pacific, coincident with relatively fresh SSS anomalies, both increasing surface buoyancy and strengthening upper-ocean stratification in the remarkable 2019–20 northeast Pacific marine heatwave (MHW; see Sidebar 3.1). The warm SSTs there were over 2 standard deviations above normal in the second half of 2020, on par with the Blob's peak magnitudes of 2013–15, and were associated with ocean heat loss to the atmosphere in 2020. As SSTs rise, MHWs are likely to increase in size, magnitude, and duration, which brings us to long-term context.

Over the decades,
seas rise, warm, acidify,
Earth's climate changes.

Global average SST was 0.39°C above the 1981–2010 average and the third-warmest year on record behind 2016 and 2019, consistent with El Niño years being anomalously warm and La Niña years being anomalously cool, relative to an overall warming trend of 0.10 ± 0.01°C decade^{-1} from 1950 to 2020. Global ocean heat content trends are generally steadier than those of SST, with four out of five analyses indicating a record high for 2020 in the 0–700-m and all five indicating a record high in the 700–2000-m layers, and a total heat increase from 2019 to 2020 in those two layers of 9.3 ± 6.2 ZJ (10^{21} Joules), entirely consistent with the long-term (1993–2020) trend of 0.58 to 0.78 W m^{-2} of excess heat energy applied to the surface area of Earth. While the strength of the Atlantic meridional overturning circulation exhibits no significant trends in the North Atlantic,

a blended satellite/in situ analysis suggests a long-term (1993–2020) strengthening of the South Atlantic subtropical gyre since 1993, consistent with warming in that basin. Global mean sea level was also at a record high in 2020, 91.3 mm above the 1993 mean, with a linear trend of 3.3 ± 0.4 mm yr^{-1}, and a statistically significant acceleration from 1993 to 2020. Anthropogenic carbon storage in the ocean was estimated at 3.0 Pg C yr^{-1} in 2020, somewhat above the 1999–2019 average of 2.33 (±0.52) Pg C yr^{-1}.

b. Sea surface temperatures—B. Huang, Z.-Z. Hu, J. J. Kennedy, and H.-M. Zhang

Sea surface temperature (SST) and its uncertainty over the global oceans (all water surfaces including seas and lakes) in 2020 are assessed using four updated products of SST. These products are the Extended Reconstruction Sea Surface Temperature version 5 (ERSSTv5; Huang et al. 2017, 2020), Daily Optimum Interpolation SST version 2.1 (DOISST; Huang et al. 2021), and two U. K. Met Office Hadley Centre SST products (HadSST.3.1.1.0 and HadSST.4.0.0.0; Kennedy et al. 2011a,b, 2019). SST anomalies (SSTAs) are calculated for each product relative to its own 1981–2010 climatology. ERSSTv5 uses averages of 500-member ensembles at monthly 2° × 2° resolution; HadSST.3.1.1.0 and HadSST.4.0.0.0 use medians of 100-member ensembles at monthly 5° × 5° resolution; and DOISST has daily 0.25° × 0.25° resolution. Magnitudes of SSTAs are compared against SST standard deviations over 1981–2010.

Averaged over the global oceans, ERSSTv5 analysis shows that SSTAs decreased slightly, but not statistically significantly, by 0.02° ± 0.02°C, from 0.41° ± 0.02°C in 2019 to 0.39° ± 0.01°C in 2020. ERSSTv5 uncertainties are determined by a Student's t-test using a 500-member ensemble with randomly drawn parameter values within reasonable ranges in the SST reconstructions (Huang et al. 2015, 2020).

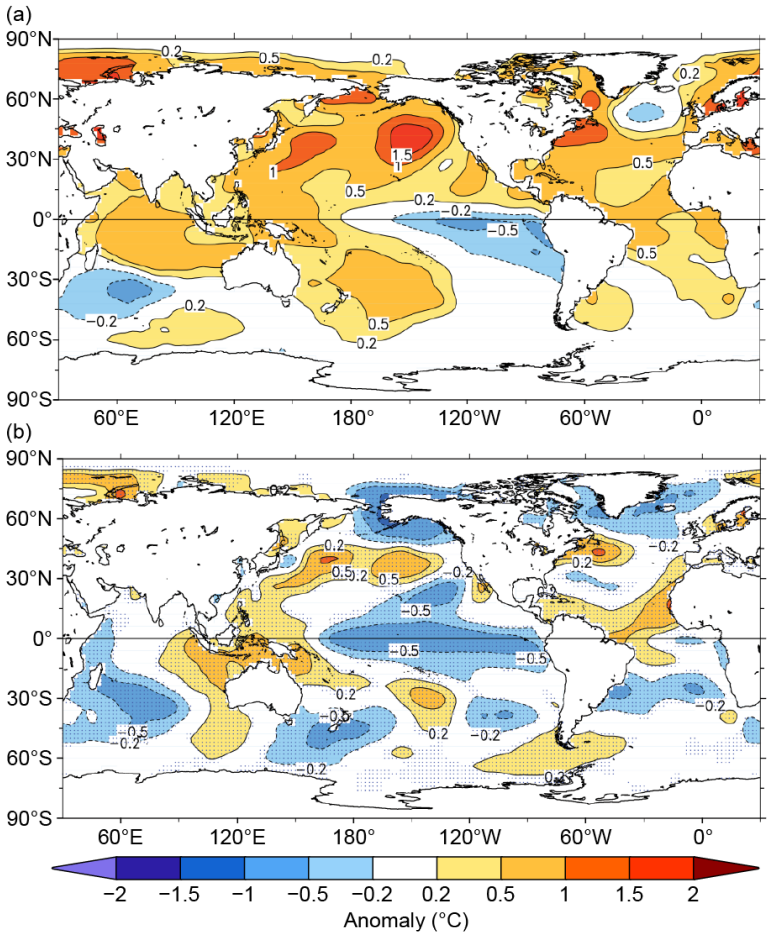

Fig. 3.1. (a) Annually averaged SSTAs (°C) in 2020 and (b) difference of annually averaged SSTAs between 2020 and 2019. Values are relative to a 1981–2010 climatology and SST differences are significant at 95% level in stippled areas.

Annually averaged SSTAs in 2020 (Fig. 3.1a) were mostly above average, between +0.5°C and +1.5°C across much of the North Pacific, between +0.2°C and +0.5°C in the western South Pacific, and between −0.2°C and −0.5°C in the eastern tropical Pacific. In the Atlantic, SSTAs were between +0.2°C and +1.0°C except south of Greenland (−0.2°C), a pattern linked to a slowdown in the Atlantic meridional overturning circulation (AMOC; Caesar et al. 2018). In the Indian Ocean, SSTAs were +0.5°C north of 25°S and between −0.2°C and −0.5°C in the western South Indian Ocean. Along the Arctic coasts, SSTAs were between +0.5°C to +1.0°C.

In comparison with averaged SST in 2019 (Fig. 3.1b), the averaged SST in 2020 increased by approximately +0.5°C in the North Pacific between 30°N and 45°N, the Indo-Pacific surrounding the Maritime Continent, the central South Pacific near 30°S, the western equatorial and tropical North Atlantic, the western North Atlantic near 45°N, and the coasts of the Arctic in the Euro-Asia sector. In

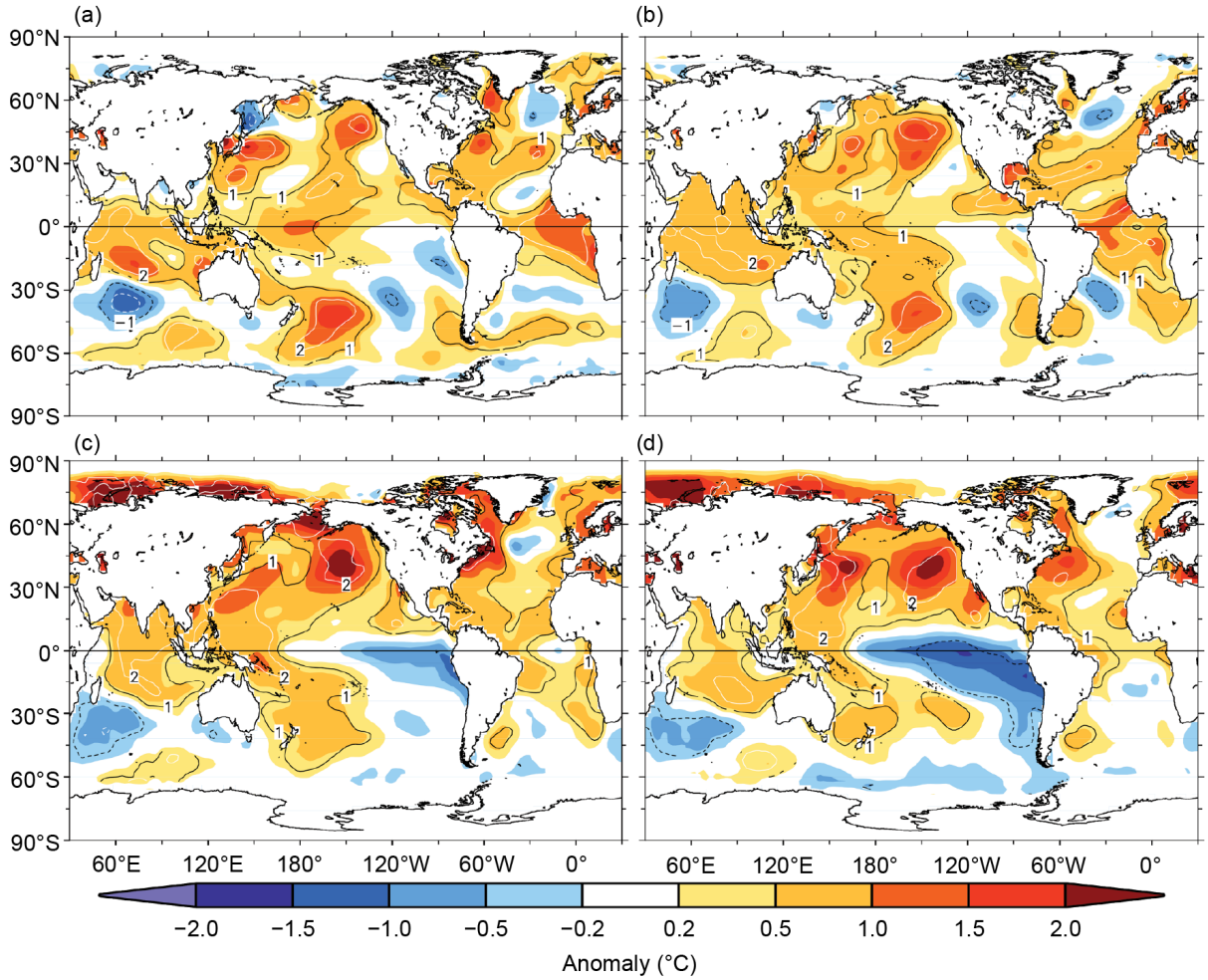

Fig. 3.2. Seasonally averaged SSTAs of ERSSTv5 (°C; shading) for (a) DJF 2019/20, (b) MAM 2020, (c) JJA 2020, and (d) SON 2020. Normalized seasonal mean SSTA based on seasonal mean std. dev. over 1981–2010 are contoured at values of –2 (dashed white), –1 (dashed black), 1 (solid black), and 2 (solid white).

contrast, the SST decreased by approximately −0.5°C in the equatorial tropical Pacific, the western and eastern South Pacific, the North Pacific and the Arctic regions surrounding Alaska, the western Indian Ocean, the North Atlantic regions surrounding Greenland, and the South Atlantic near 30°S. These SST changes are statistically significant at the 95% confidence level based on an ensemble analysis of 500 members.

The cooling in the tropical Pacific is associated with the transition from a weak El Niño in 2018–19 to a moderate La Niña in 2020–21 (see section 4b). The La Niña cooling started to be visible in June–August (JJA; Fig. 3.2c) and continued strengthening throughout September–November (SON; Fig. 3.2d). The near-uniform SSTAs in the Indian Ocean resulted in a near-neutral Indian Ocean dipole (IOD; Saji et al. 1999; see section 4f), in contrast to the strongly positive IOD index seen in late 2019. The Atlantic Niño index (Zebiak 1993) dropped dramatically from +1.5°C in 2018–19 to +0.2°C in the latter half of 2020, indicating a transition from a strong Atlantic Niño in 2018–19 to more neutral conditions.

For the seasonal mean SSTAs in 2020, in most of the North Pacific, SSTAs were +0.2° to +1.0°C (+1 to +2 std. dev.) in December–February (DJF) and March–May (MAM) (Figs. 3.2a,b). The anomalies increased to as high as +2.0°C (+2 std. dev.) in JJA and SON (Figs. 3.2c, d). In contrast, in the tropical and eastern South Pacific, SSTAs were small in DJF and MAM, and decreased to −0.5° to −1.0°C (–1 std. dev.) in JJA and SON. In the western South Pacific, SSTAs decreased from +1.5°C (+2 std. dev.) in DJF to +1.0°C in MAM and +0.5°C in JJA and SON. The pronounced SSTAs in the North Pacific in JJA and SON (Sidebar 3.1; Scannell et al. 2020) and in the western South Pacific east of New Zealand

Table 3.1. Linear trends of annually and regionally averaged SSTAs (°C decade^{-1}) from ERSSTv5, HadSST, and DOISST. Uncertainties at 95% confidence level are estimated by accounting for the effective sampling number quantified by lag-1 autocorrelation on the degrees of freedom of annually averaged SST series.

Product	Region	2000–2020 (°C decade^{-1})	1950–2020 (°C decade^{-1})
HadSST.3.1.1.0	Global	0.14 ± 0.06	0.09 ± 0.02
HadSST.4.0.0.0	Global	0.18 ± 0.06	0.112 ± 0.02
DOISST	Global	0.20 ± 0.05	N/A
ERSSTv5	Global	0.17 ± 0.07	0.10 ± 0.01
ERSSTv5	Tropical Pacific (30°S–30°N)	0.18 ± 0.17	0.10 ± 0.03
ERSSTv5	North Pacific (30°–60°N)	0.36 ± 0.14	0.08 ± 0.04
ERSSTv5	Tropical Indian Ocean (30°S–30°N)	0.21 ± 0.09	0.14 ± 0.02
ERSSTv5	North Atlantic (30°–60°N)	0.14 ± 0.09	0.11 ± 0.05
ERSSTv5	Tropical Atlantic (30°S–30°N)	0.15 ± 0.09	0.11 ± 0.02
ERSSTv5	Southern Ocean (30°–60°S)	0.12 ± 0.06	0.10 ± 0.02

were associated with marine heatwaves (Hu et al. 2011; Oliver et al. 2017; Perkins-Kirkpatrick et al. 2019; Babcock et al. 2019; see also section 2b3).

In the Euro-Asian coasts of the Arctic, SSTAs were neutral in DJF and MAM due to sea ice holding SSTs at the freezing point, but reached more than +2.0°C (+2 std. dev.) in JJA and SON (Figs. 3.2c,d). In the Indian Ocean and Maritime Continent, SSTAs of approximately +0.5°C (+2 std. dev.) were sustained throughout 2020 (Figs. 3.2a–d). In the tropical Atlantic, SSTAs were approximately +1.0°C (+2 std. dev.) in DJF and MAM and decreased to between +0.2°C and 0.5°C (+1 std. dev.) in JJA and SON. In contrast, in the western North Atlantic, SSTAs increased from between +0.5°C and 1.0°C (+1 std. dev.) in DJF and MAM to between +1.0°C and 1.5°C (+2 std. dev.). In the South Atlantic, SSTAs were near neutral in DJF, became below normal (−0.5°C) in the west and above normal (+0.5°C) in the east in MAM, and became near neutral again in JJA and SON.

The global oceans have exhibited an overall warming trend since the 1950s (Figs. 3.3a,b; Table 3.1), albeit with slightly lower SSTAs in 2020 (+0.39° ± 0.01°C) than in 2019 (+0.41° ± 0.02°C), due in part to La Niña. The year 2020 was the third warmest after the record high of 2016 (+0.44° ± 0.01°C) and 2019, but their separation may not be statistically significant. Linear trends of globally annually averaged SSTAs were 0.10° ± 0.01°C decade^{-1} over 1950–2020 (Table 3.1). Spatially, the warming was largest in the tropical Indian Ocean (Fig. 3.3e; 0.14° ± 0.02°C decade^{-1}) and smallest in the North Pacific (Fig. 3.3d; 0.08° ± 0.04°C decade^{-1}). Here, the uncertainty of the trends represents the 95% confidence level of the linear fitting uncertainty and 500-member data uncertainty.

In addition, interannual to interdecadal variabilities of SSTAs can be seen in all ocean basins. The variation amplitudes are large in the North Atlantic (Fig. 3.3f), which may be associated with the Atlantic Multidecadal Variability (Schlesinger and Ramankutty 1994) that may have in turn resulted from many internal and external factors such as aerosols and the AMOC (Zhang et al. 2019; Wang and Yang 2017), with warm periods in the early 1950s and from the late 1990s to the 2010s, and a cold period from the 1960s to the early 1990s. Similarly, SSTAs in the North Pacific (Fig. 3.3d) decreased from the 1960s to the late 1980s, followed by an increase from the late 1980s to the 2010s.

We compare SSTAs in ERSSTv5 with those in DOISST, HadSST.3.1.1.0, and HadSST.4.0.0.0, averaging all annually on a 2° × 2° grid (Fig. 3.3). SSTA departures of DOISST, HadSST.3.1.1.0, and HadSST.4.0.0.0 from ERSSTv5 are largely within 2 standard deviations (gray shading, Fig. 3.3). Overall, HadSST.4.0.0.0 is more consistent with ERSSTv5 than HadSST.3.1.1.0 before 1980, owing to its updated corrections to the SST observations from ships (e.g., ship engine room intakes, ship bucket) that had been used in both HadSST.4.0.0.0 and ERSSTv5. In the 2000s–10s, SSTAs were slightly higher in DOISST than in ERSSTv5 in the Southern Ocean, tropical Atlantic Ocean, and tropical Indian Ocean, and therefore

SST trends were slightly higher in DOISST over 2000–20 (Table 3.1). These SSTA differences have been mostly attributed to the differences in bias corrections to ship observations in those products (Huang et al. 2015; Kent et al. 2017), and have resulted in a slightly weaker SSTA trend in HadSST.3.1.1.0 but a stronger SSTA trend in HadSST.4.0.0.0 over both 1950–2020 and 2000–20 (Table 3.1).

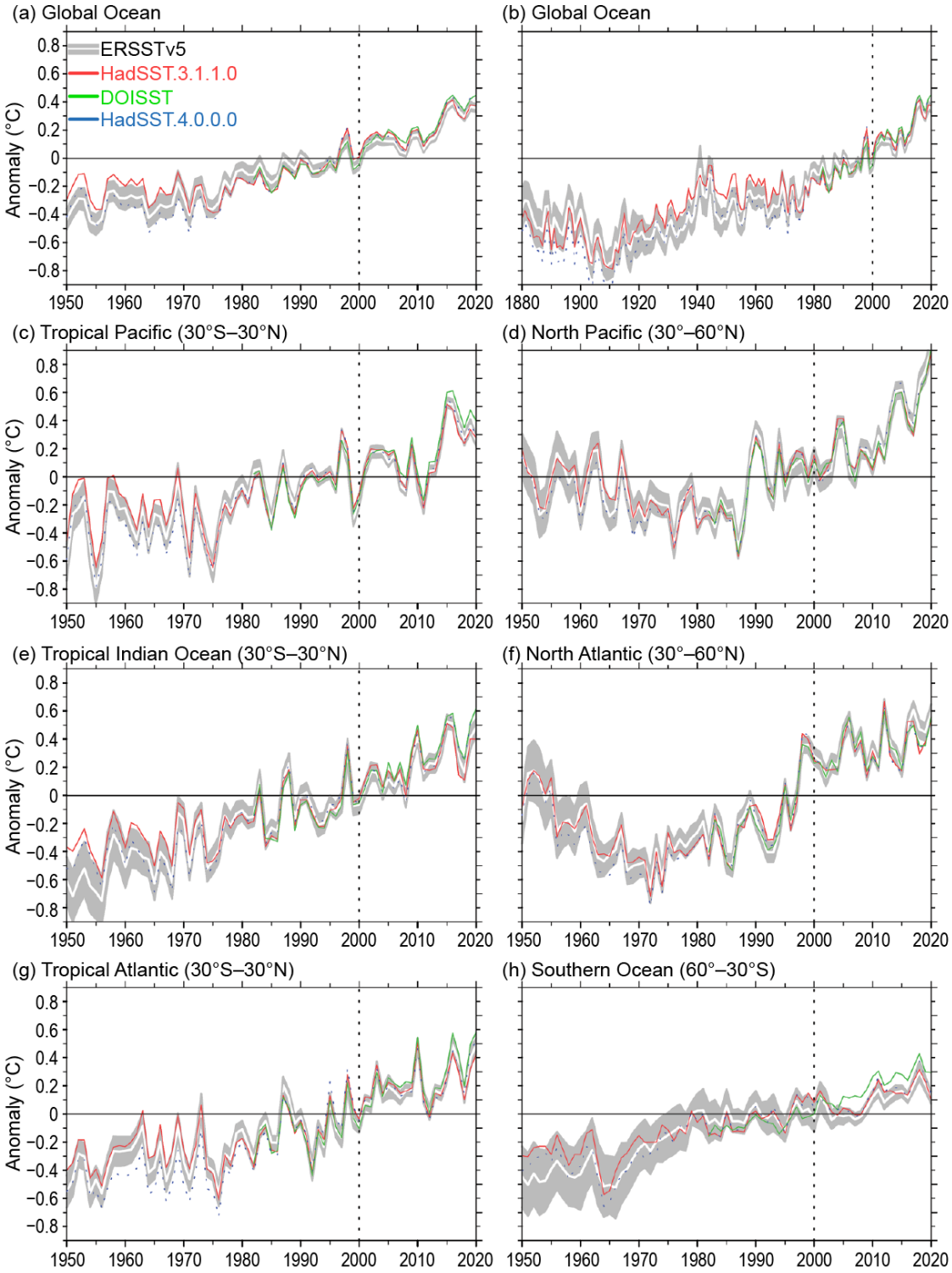

Fig. 3.3. Annually-averaged SSTAs of ERSSTv5 (solid white) and 2 std. dev. (gray shading) of ERSSTv5, SSTAs of DOISST (solid green), and SSTAs of HadSST.3.1.1.0 (solid red) and HadSST.4.0.0.0 (dotted blue) during 1950–2020 except for (b). (a) Global oceans, (b) global oceans in 1880–2020, (c) tropical Pacific, (d) North Pacific, (e) tropical Indian, (f) North Atlantic, (g) tropical Atlantic, and (h) Southern Oceans. The 2 std. dev. envelope was derived from a 500-member ensemble analysis based on ERSSTv5 (Huang et al. 2020) and centered to SSTAs of ERSSTv5. The year 2000 is indicated by a vertical black dotted line.

Sidebar 3.1: **The 2019–20 northeast Pacific marine heatwave**—H. A. SCANNELL AND D. J. AMAYA

Following the warm years of the 2013–15 marine heatwave (MHW) known as "the Blob" (Bond et al. 2015), the northeast Pacific Ocean experienced another devastating MHW, which formed during the summer of 2019 and persisted through 2020 (Amaya et al. 2020; Scannell et al. 2020). An MHW is defined when sea surface temperatures (SSTs) exceed an extremely warm threshold (e.g., the 90th percentile) for an extended period of time (e.g., at least five days; Hobday et al. 2016). In June 2019, an MHW developed in the northeast Pacific Ocean and by August it grew to encompass an ocean area spanning the Gulf of Alaska to the Hawaiian Islands (Fig. SB3.1a). The event was so unusual that the June–August SST anomalies (SSTA), which were >2.5°C above normal, broke a 40-year (1980–2019) summertime record (Amaya et al. 2020). Like the Blob, this event had local and regional impacts on marine ecosystems and fish redistributions (NOAA 2019). During 2019, the MHW along the U.S. West Coast initiated harmful algal blooms and coral reefs near Hawaii started to bleach under high thermal stress (Cornwall 2019). Off Oregon, warmer waters brought albacore tuna closer to shore, making them more accessible to recreational anglers, leading to record-breaking landings in September (Lambert 2019). Although many speculated that this summertime MHW would not last due to its shallow depth, its persistence into 2020 was unrelenting (Fig. SB3.1c)

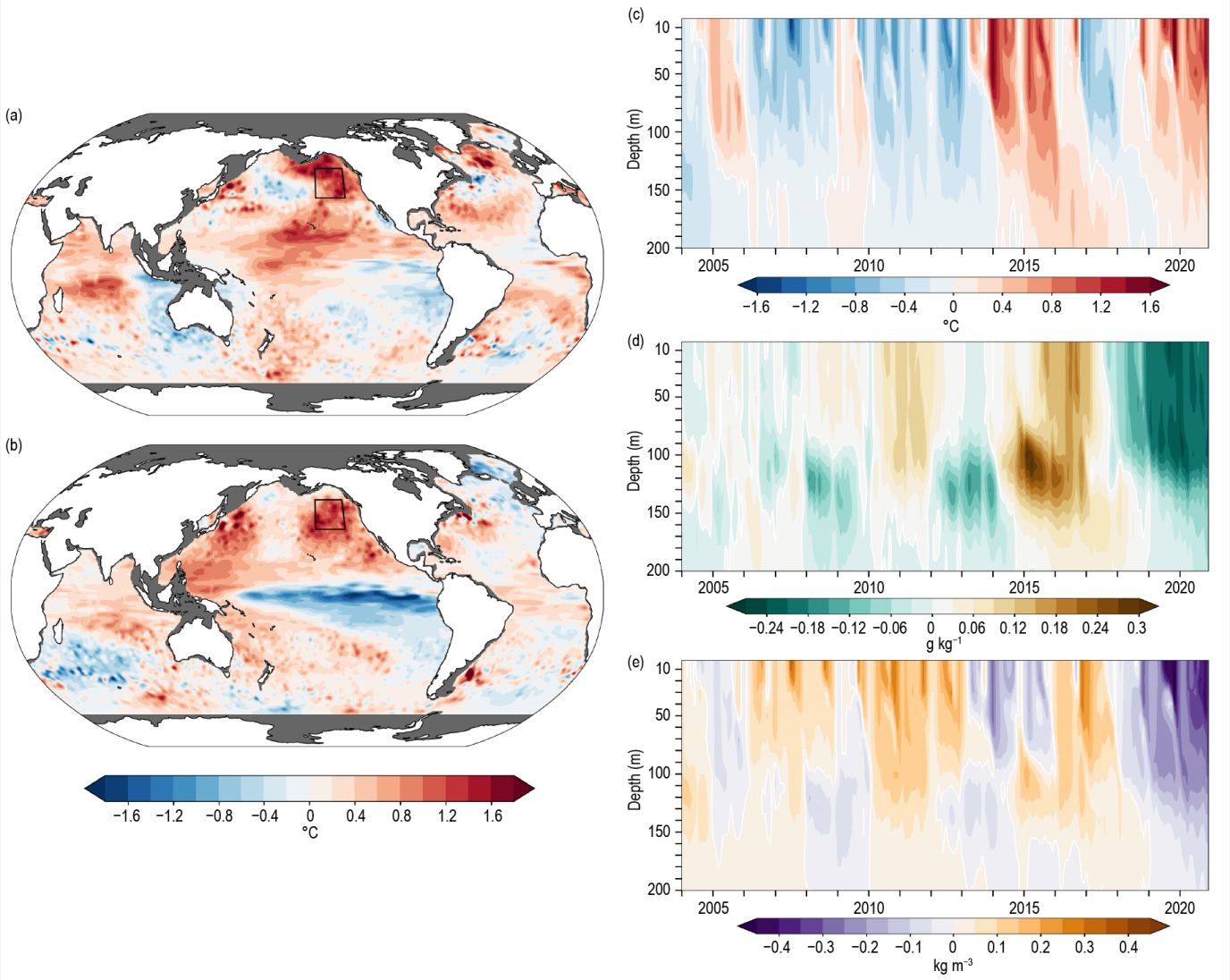

Fig. SB3.1. Seasonal 2.5-m temperature anomaly average (°C) over (a) JJA in 2019 and (b) SON in 2020. Time–depth plots of subsurface (c) temperature (°C), (d) salinity (g kg^{-1}), and (e) density (kg^{-3}) anomalies averaged within the northeast Pacific (35.5°–51.5°N, 135.5°–154.5°W; black box in (a) and (b) from Jan 2004 through Dec 2020. Subsurface observations were taken from the updated Roemmich-Gilson Argo Climatology (Roemmich and Gilson 2009) and monthly anomalies were computed with respect to the 2004–20 monthly means.

and its spatial scale rivaled its predecessor—the Blob (Bond et al. 2015).

The factors contributing to the onset of the 2019–20 northeast Pacific MHW are described by Amaya et al. (2020) and are summarized here. SSTAs that formed during summer 2019 were atmospherically forced. Remote influence from warm SSTAs near the central equatorial Pacific contributed to a weakening of the North Pacific (atmospheric pressure) High and associated surface winds from April through August. A reduction in wind-driven, upper-ocean mixing resulted in a record shallow mixed layer depth. Summertime surface heat fluxes more efficiently warmed the anomalously thin mixed layer, contributing to the rapid rise in SST. Downward heat fluxes were dominated by a reduction in latent heat loss from weakened surface winds and an increase in downwelling shortwave radiation due to diminished low-level clouds. In particular, the reduction in low cloud cover initiated a positive low-cloud-SST feedback, which amplified the intensity of the 2019 summer MHW and contributed to its overall persistence.

The spatial pattern of surface warming evolved in the northeast Pacific over the course of 2019 and 2020. This evolution was facilitated by remote influences from the tropics and extratropics. As described previously, warm anomalies in the central equatorial and subtropical Pacific in 2019 (Fig. SB3.1a) helped weaken the mean state of the atmosphere over northern latitudes, leading to the MHW onset. A positive Pacific Meridional Mode also likely helped modulate the surface heat fluxes over the North Pacific by shifting the Intertropical Convergence Zone farther north and further weakening the North Pacific High (Amaya et al. 2020). The transition to La Niña conditions in 2020 reversed the sign of anomalies near the equator. However, the northeast Pacific remained in a MHW-like state (Fig. SB3.1b). La Niña can disrupt weather patterns in the Northern Hemisphere midlatitudes through a teleconnection associated with the negative phase of the Pacific/North American (PNA) pattern (Wallace and Gutzler 1981). The negative PNA can establish more atmospheric ridging over the northeast Pacific Ocean, which diverts normal upper-level flow and is conducive to warming SSTs during boreal winter.

Once the surface mixed layer is heated from the atmosphere, those temperature anomalies can be redistributed within the ocean and begin to propagate horizontally or downward (Scannell et al. 2020). The upper 200 m of the water column was anomalously warm throughout 2020, with maximum intensities contained within the upper 70 m (Fig. SB3.1c). An unusual fresh anomaly that extended to 120 m (Fig. SB3.1d) accompanied the near-surface warming and likely originated from a net freshwater input from precipitation in the Gulf of Alaska in 2018 (Reagan et al. 2019; Yu et al. 2019). The salinity anomaly from 2018 through 2020 was the longest lasting, most intense, and deepest reaching fresh event observed since at least 2004. In contrast, the Blob in 2013–15 had the warmest and most salty near-surface anomalies since at least 2004. The subsurface freshwater anomaly in 2019–20 increased the buoyancy of the surface layer (Fig. SB3.1e). The decrease in surface density and resulting increase in stratification prevented the warm surface anomalies from penetrating as deeply as the Blob in 2013–15. However, the surface MHW anomalies in 2019–20 mixed into the subsurface across both isobars and isopycnals (Scannell et al. 2020). The subsurface burial and storage of surface MHW anomalies contributes to the long-lived persistence and memory of these events in the northeast Pacific Ocean, and their possible seasonal reemergence.

The northeast Pacific Ocean has warmed significantly over the past half-century due to anthropogenic climate change (Bulgin et al. 2020). Increased ocean temperatures not only make MHWs more likely to occur in the North Pacific (Scannell et al. 2016), they also increase the intensity and duration of these events over time (Oliver 2019; Laufkötter et al. 2020). Ocean warming has significantly contributed to a shoaling trend in North Pacific summertime mixed layers (~15% decrease) from 1980 to 2015 (Amaya et al. 2021). Shallower mixed layers reduce the effectiveness of detraining surface MHW anomalies into the subsurface and trap them near the surface (Amaya et al. 2020; Scannell et al. 2020). As a result, it is expected that MHWs will intensify in the coming decades as surface stratification increases and summertime mixed layers continue to shoal (Amaya et al. 2021; Li et al. 2020; Alexander et al. 2018).

The 2019–20 MHW was the latest event in a recent trend of increasing temperature extremes that has dominated the northeast Pacific. Second to the Blob in 2013–15, this event was the most expansive MHW since 1982, covering an ocean area roughly six times the size of Alaska in September 2020 (NWFSC 2020). However, the 2019–20 event really stands out for developing during the summer, when mixed layers were anomalously shallow and the subsurface was extremely fresh (Amaya et al. 2020; Scannell et al. 2020). The combination of these factors likely helped to amplify the intensification of this event. It is an open question whether the physical mechanisms responsible for this MHW are broadly applicable to summer-initiated events. The northeast Pacific Ocean has remained anomalously warm and fresh heading into 2021, and the subsurface has warmed substantially, likely as a result (Fig. SB3.1). This event's persistence is being closely monitored as La Niña conditions continue to dominate the tropics.

c. Ocean heat content—G. C. Johnson, J. M. Lyman, T. Boyer, L. Cheng, J. Gilson, M. Ishii, R. E. Killick, and S. G. Purkey

The oceans have been warming for decades owing to increases in greenhouse gasses in the atmosphere (Rhein et al. 2013), storing massive amounts of heat energy and expanding as they warm to contribute about 40% of the increase in global average sea level (WCRP Global Sea Level Budget Group 2018). This warming, while surface intensified, is not limited to the upper ocean, having been widely observed from 4000 to 6000 m in the coldest, densest bottom waters (Purkey and Johnson 2010). The El Niño–Southern Oscillation effects strong regional variations in ocean temperature and also modulates the rate of global ocean heat uptake (Johnson and Birnbaum 2017). The overall warming trend has increased the frequency and intensity of marine heatwaves (Laufkötter et al. 2020; see section 3b and Sidebar 3.1), which in turn have substantial effects on ecosystems (Smale et al. 2019). Additionally, warmer upper ocean waters can drive stronger hurricanes (Goni et al. 2009). Ocean warming has also been shown to increase melting rates of ice sheet outlet glaciers around Greenland (Castro de la Guardia et al. 2015) and Antarctica (Schmidtko et al. 2014).

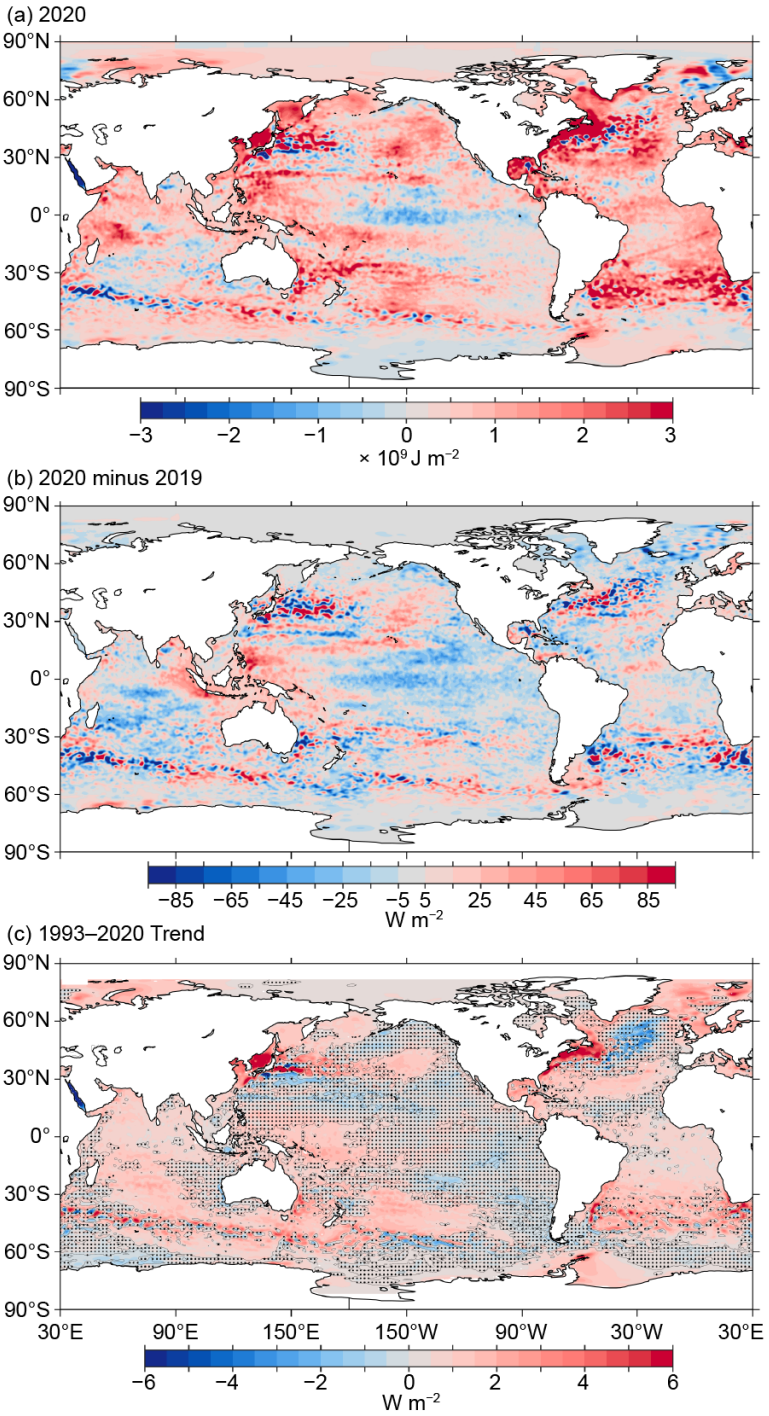

Fig. 3.4. (a) Combined satellite altimeter and in situ ocean temperature data estimate of upper (0–700 m) OHCA (× 10^9 J m^{-2}) for 2020 analyzed following Willis et al. (2004) but using an Argo monthly climatology and displayed relative to the 1993–2020 baseline. (b) 2020 minus 2019 combined estimates of OHCA expressed as a local surface heat flux equivalent (W m^{-2}). For (a) and (b) comparisons, note that 95 W m^{-2} applied over one year results in a 3 × 10^9 J m^{-2} change of OHCA. (c) Linear trend from 1993–2020 of the combined estimates of upper (0–700 m) annual OHCA (W m^{-2}). Areas with statistically insignificant trends are stippled.

Maps of annual (Fig. 3.4) upper (0–700 m) ocean heat content anomaly (OHCA) relative to a 1993–2020 baseline mean are generated from a combination of in situ ocean temperature data and satellite altimetry data following Willis et al. (2004), but using Argo (Riser et al. 2016) data downloaded from an Argo Global Data Assembly Centre in January 2021. Near-global average monthly temperature anomalies (Fig. 3.5) versus pressure from Argo data (Roemmich and Gilson 2009, updated) since 2004 and in situ global estimates of OHCA (Fig. 3.6) for three pressure layers (0–700 m, 700–2000 m, and 2000–6000 m) from five different research groups are also discussed.

The 2020 minus 2019 difference of 0–700-m OHCA (Fig. 3.4b) in the Pacific shows an increase in the western tropical Pacific and a decrease in the central to eastern equatorial Pacific, consistent

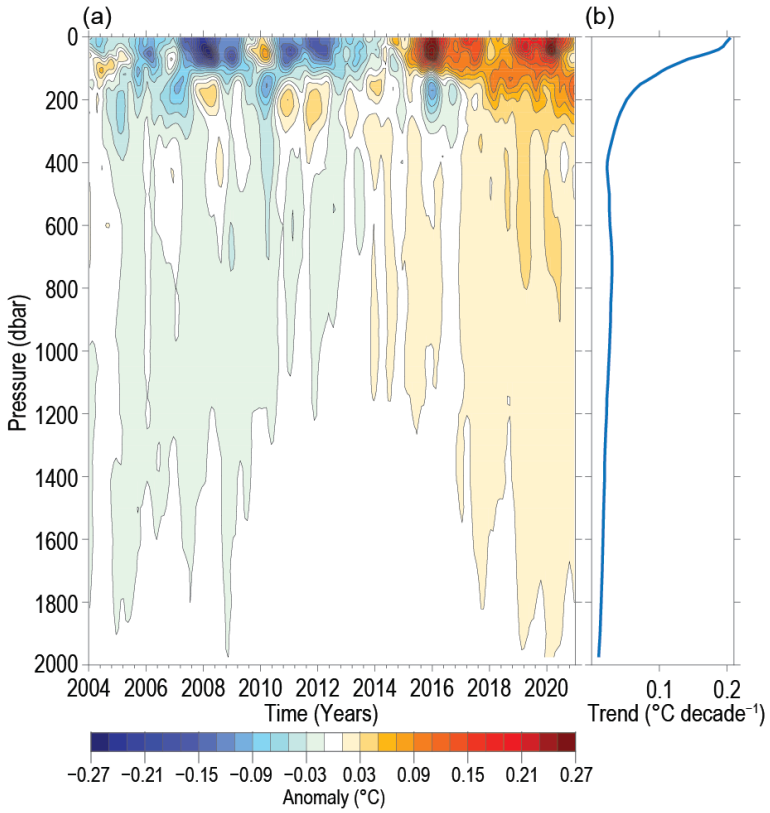

Fig. 3.5. (a) Near-global (65°S–80°N, excluding continental shelves, the Indonesian seas, and the Sea of Okhostk) average monthly ocean temperature anomalies (°C; updated from Roemmich and Gilson [2009]) relative to record-length average monthly values, smoothed with a 5-month Hanning filter and contoured at odd 0.02°C intervals (see colorbar) versus pressure and time. (b) Linear trend of temperature anomalies over time for the length of the record in (a) plotted versus pressure in °C decade^{-1} (blue line).

with the onset of a La Niña in 2020. La Niña induces this pattern with a shoaling of the equatorial thermocline in the central and eastern equatorial Pacific and a deepening of the western tropical Pacific warm pool as a response to strengthened easterly trade winds (see Fig. 3.13a), which also generate anomalous westerly surface currents on the equator (see Figs. 3.18, 3.19b–d). As a result, in the equatorial Pacific, the 2020 anomalies (Fig. 3.4a) are negative in the east and positive in the west. Outside of the tropics, the 2020 minus 2019 difference is toward higher values in the centers of the North and South Pacific basins, with some lower values in the eastern portions of the basin, consistent with an intensified cool (negative) phase of the Pacific Decadal Oscillation index in 2020 (see Fig. 3.1). Upper OHCA in the Pacific in 2020 is generally above the long-term average (Fig. 3.4a), with the most prominent negative values limited to the central tropical Pacific and the Southern Ocean south of 60°S.

In the Indian Ocean, the 2020 minus 2019 difference of 0–700-m OHCA

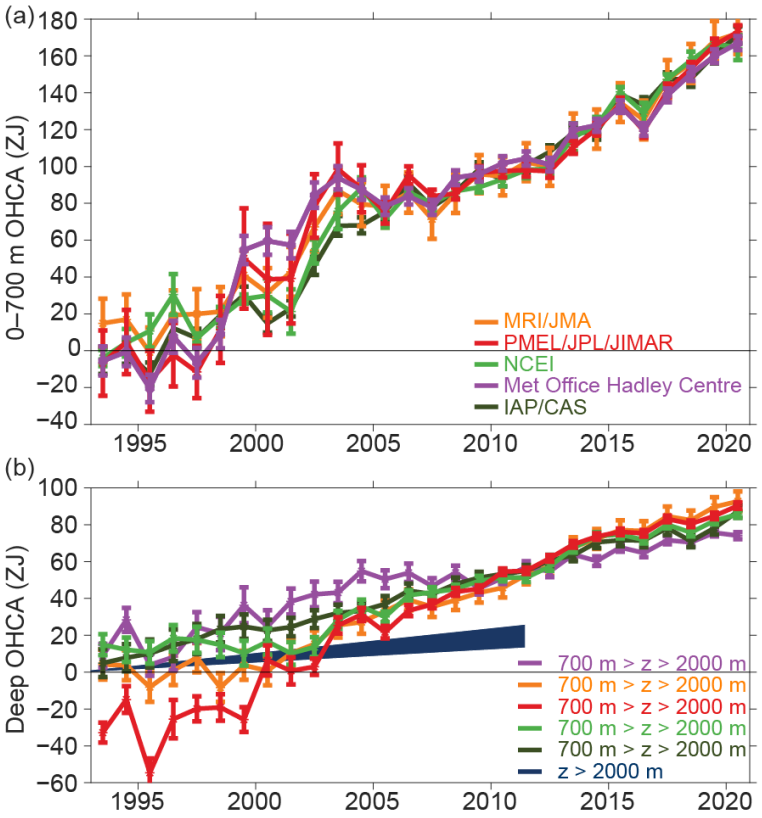

Fig. 3.6. (a) Annual average global integrals of in situ estimates of upper (0–700 m) OHCA (ZJ; 1 ZJ = 10^{21} J) for 1993–2020 with standard errors of the mean. The MRI/JMA estimate is an update of Ishii et al. (2017). The PMEL/JPL/JIMAR estimate is an update and refinement of Lyman and Johnson (2014). The NCEI estimate follows Levitus et al. (2012). The Met Office Hadley Centre estimate is computed from gridded monthly temperature anomalies (relative to 1950–2019) following Palmer et al. (2007). The IAP/CAS estimate is reported in Cheng et al. (2020). See Johnson et al. (2014) for details on uncertainties, methods, and datasets. For comparison, all estimates have been individually offset (vertically on the plot), first to their individual 2005–20 means (the best sampled time period), and then to their collective 1993 mean. (b) Annual average global integrals of in situ estimates of intermediate (700–2000 m) OHCA for 1993–2020 with standard errors of the mean, and a long-term trend with one standard error uncertainty shown from 1992.4–2011.6 for deep and abyssal (z > 2000 m) OHCA following Purkey and Johnson (2010) but updated using all repeat hydrographic section data available from https://cchdo.ucsd.edu/ as of Jan 2021.

(Fig. 3.4b) exhibits increases in the eastern third of the basin, from the Bay of Bengal to the Antarctic Circumpolar Current (ACC) and decreases in the center of the basin from the equator to the ACC. Upper OHCA values for 2020 were above the 1993–2020 mean over almost all of the Indian Ocean (Fig. 3.4a), with the higher values in the western half of the basin. The low 2020 upper OHCA values in the vicinity of the ACC in the west and the high values in the east suggest a northward excursion of that current in the west and a southward excursion in the east in 2020. The 2020 minus 2019 differences of 0–700-m OHCA (Fig. 3.4b) in the Atlantic Ocean are toward cooling around the Caribbean Islands and Florida, offshore of some of the east coast of North America, and in the Greenland–Iceland–Norwegian Seas. In much of the rest of the ocean, the tendency is weakly, but generally toward, warming. In 2020, almost the entire Atlantic Ocean exhibited upper OHCA above the 1993–2020 average (Fig. 3.4a) with especially warm conditions in the Gulf of Mexico, off the east coast of North America, and across the southern subtropical South Atlantic.

The large-scale statistically significant (Fig. 3.4c) regional patterns in the 1993–2020 local linear trends of upper OHCA are quite similar to those from 1993–2019 (Johnson et al. 2020). The longer the period over which these trends are evaluated, the more of the ocean surface area is covered by warming trends, either statistically significant or not, and the less it is covered by cooling trends (Johnson and Lyman 2020). The most prominent area with statistically significant negative trends is found mostly south of Greenland in the North Atlantic, a pattern that has been linked, together with the very strong warming trend off the east coast of North America, to a decrease in the Atlantic meridional overturning circulation (Dima and Lohmannn 2010; Caesar et al. 2018), although there are contributions from variations in local air–sea exchange (strong winter cooling in the years around 2015) and shortwave cloud feedbacks as well (Josey et al. 2018). Another cooling trend is found near the ACC in the central South Pacific. As noted in previous *State of the Climate* reports, the warming trends in the western boundary currents and extensions (Gulf Stream, Kuroshio, Agulhas, East Australia Current, and Brazil Current) are all quite prominent and may be associated with poleward shifts of these currents driven by changes in surface winds (Wu et al. 2012). Much of the Atlantic Ocean, the Indian Ocean, and the western and central Pacific Ocean exhibit statistically significant warming trends as well.

Near-global average seasonal temperature anomalies (Fig. 3.5a) from the start of 2004 through the end of 2020 exhibit a clear surface-intensified, record-length warming trend (Fig. 3.5b) that exceeds 0.2°C decade^{-1} at the surface. The reduction of warm anomalies during 2020 in the upper 100 dbar, with increases in warming from 100 to 400 dbar, is consistent with the transition to a La Niña in 2020. This pattern in the global average reflects a prominent large-scale regional change, as the equatorial Pacific thermocline shoals in the east and deepens in the west (e.g., Roemmich and Gilson 2011; Johnson and Birnbaum 2017). The pattern can be seen in other La Niña periods (e.g., 2007–08 and 2010–12). The opposite pattern is evident during El Niño years (e.g., 2009–10 and 2015–16) when the east–west tilt of the equatorial Pacific thermocline reduces as easterly trade winds subside, and even reverse at times.

As noted in previous reports, the analysis is extended back in time from the Argo period to 1993, and expanded to examine greater depths, using sparser, more heterogeneous historical data collected mostly from ships (e.g., Abraham et al. 2013). The different estimates of annual globally integrated 0–700-m OHCA (Fig. 3.6a) all reveal a large increase since 1993, with four of the five analyses reporting 2020 as a record high. The globally integrated 700–2000-m OHCA annual values (Fig. 3.6b) vary somewhat among analyses, but all five analyses report 2020 as a record high, and the long-term warming trend in this layer is also clear. Globally integrated OHCA values in both layers vary more both from year-to-year for individual years and from estimate-to-estimate in any given year prior to the achievement of a near-global Argo array around 2005. The water column from 0–700 and 700–2000 m gained 5.4 (±4.8) and 3.9 (±3.9) ZJ, respectively

Table 3.2. Trends of ocean heat content increase (in W m^{-2} applied over the 5.1 × 10^{14} m^2 surface area of Earth) from seven different research groups over three depth ranges (see Fig. 3.6 for details). For the 0–700- and 700–2000-m depth ranges, estimates cover 1993–2020, with 5%–95% uncertainties based on the residuals taking their temporal correlation into account when estimating degrees of freedom (Von Storch and Zwiers 1999). The 2000–6000-m depth range estimate, an update of Purkey and Johnson (2010), uses data from 1981 to 2020, while the global average is from May 1992 to Aug 2011, again with 5%–95% uncertainty.

	Global ocean heat content trends (W m^{-2}) for three depth ranges		
Research Group	0–700 m	700–2000 m	2000–6000 m
MRI/JMA	0.37 ± 0.05	0.24 ± 0.05	
PMEL/JPL/JIMAR	0.39 ± 0.12	0.31 ± 0.05	
NCEI	0.39 ± 0.05	0.19 ± 0.05	
Met Office Hadley Centre	0.38 ± 0.12	0.15 ± 0.04	
IAP/CAS	0.41 ± 0.04	0.18 ± 0.01	
Purkey and Johnson			0.06 ± 0.03

(means and standard deviations given) from 2019 to 2020. Causes of differences among estimates are discussed in Johnson et al. (2015).

The estimated linear rates of heat gain for each of the five global integral estimates of 0–700-m OHCA from 1993 through 2020 (Fig. 3.6a) range from 0.37 (±0.05) to 0.41 (±0.04) W m^{-2} applied over the surface area of Earth, as is customary in climate science (Table 3.2). These results are not much different from those in previous reports, although with an increasing record length trend uncertainties tend to decrease and differences among analyses tend to grow smaller. Linear trends from 700 to 2000 m over the same time period range from 0.15 (±0.04) to 0.31 (±0.05) W m^{-2}. Trends in the 0–700-m layer all agree within their 5%–95% confidence intervals. However, as noted in previous reports, one of the trends in the 700–2000-m layer, which is quite sparsely sampled prior to the start of the Argo era (circa 2005), does not. Different methods for dealing with under-sampled regions likely cause this disagreement. Using repeat hydrographic section data collected from 1981 to 2020 to update the estimate of Purkey and Johnson (2010) for 2000–6000 m, the linear trend is 0.06 (±0.03) W m^{-2} from May 1992 to August 2011 (these dates are global average times of first and last sampling of the sections). Summing the three layers (despite their slightly different time periods as given above), the full-depth ocean heat gain rate ranges from 0.58 to 0.78 W m^{-2} applied to Earth's entire surface.

d. Salinity—G. C. Johnson, J. Reagan, J. M. Lyman, T. Boyer, C. Schmid, and R. Locarnini

1) Introduction

Salinity is the measure of the mass of dissolved salts in a unit mass of seawater. Temperature and salinity vary spatially and temporally in the ocean. Atmospheric freshwater fluxes (namely evaporation and precipitation), advection, mixing, entrainment, sea ice melt/freeze, and river runoff all modify salinity (e.g., Qu et al. 2011; Ren et al. 2011). Sea surface salinity (SSS) and evaporation minus precipitation ($E-P$) have long been known to be highly correlated (Wüst 1936). SSS patterns are maintained through a balance among advection, mixing, and $E-P$ fluxes (Durack 2015). Roughly 86% of global evaporation and 78% of global precipitation occurs over the ocean (Baumgartner and Reichel 1975; Schmitt 1995), making the ocean Earth's largest rain gauge (Schmitt 2008). Evaporation-dominated regions, such as the subtropical North Atlantic, are generally saltier, whereas precipitation-dominated regions like the Intertropical Convergence Zone (ITCZ) are generally fresher. Furthermore, changes in the hydrological cycle can be estimated by salinity changes (e.g., Durack and Wijffels 2010; Durack et al. 2012; Skliris et al. 2014).

Seawater density at a given pressure is a function of temperature and salinity. In cold water, salinity variations tend to dominate density (Pond and Pickard 1983). Therefore, changes in salinity at high latitudes can have large impacts on ocean stratification and even alter the global thermohaline circulation (e.g., Gordon 1986; Broecker 1991). For example, the Atlantic meridional overturning circulation (section 3h) is vulnerable to changes in salinity (e.g., Liu et al. 2017). Ocean stratification (i.e., the vertical density gradient) has been found to be increasing over the past 50 years (Li et al. 2020), which has likely reduced ocean ventilation. Thus, diagnosing changes in surface and subsurface salinity is critical for monitoring potential changes in the hydrological cycle and ocean dynamics.

To investigate interannual changes of subsurface salinity, all available salinity profile data are quality controlled following Boyer et al. (2018) and then used to derive 1° monthly mean gridded salinity anomalies relative to a long-term monthly mean for years 1955–2012 (World Ocean Atlas 2013 version 2 [WOA13v2]; Zweng et al. 2013) at standard depths from the surface to 2000 m (Boyer et al. 2013). In recent years, the largest source of salinity profiles is the profiling floats of the Argo program (Riser et al. 2016). These data are a mix of real-time (preliminary) and delayed-mode (scientific quality controlled) observations. Hence, the estimates presented here may be subject to instrument biases such as Argo conductivity, temperature, depth devices with "fast salty drift," and could change after all data are subjected to scientific quality control. The SSS analysis relies on Argo data downloaded in January 2021, with annual anomaly maps relative to a seasonal climatology generated following Johnson and Lyman (2012) as well as monthly maps of bulk (as opposed to skin) SSS data from the Blended Analysis of Surface Salinity (BASS; Xie et al. 2014). BASS blends in situ SSS data with data from the *Aquarius* (Le Vine et al. 2014; mission ended in June 2015), Soil Moisture and Ocean Salinity (Font et al. 2013), and the Soil Moisture Active Passive (Fore et al. 2016) satellite missions. Despite the larger uncertainties of satellite data relative to Argo data, their higher spatial and temporal sampling allows higher spatial and temporal resolution maps than are possible using in situ data alone at present. All salinity values used in this section are dimensionless and reported on the Practical Salinity Scale-78 (PSS-78; Fofonoff and Lewis 1979).

2) Sea surface salinity—G. C. Johnson and J. M. Lyman

As noted in previous reports, since salinity has no direct feedback to the atmosphere, large-scale SSS anomalies can be quite persistent. This persistence contrasts with sea surface temperature (SST) anomalies, which are often damped by air–sea heat exchange (e.g., an anomalously warm ocean loses heat to the atmosphere, so SST cools). For example, one of the largest fresh SSS anomalies in 2020, located in the northeastern Pacific (Fig. 3.7a), began around 2016 in the central North Pacific (near 40°N between Hawaii and the Aleutian Islands), shifting eastward over time and strengthening overall (see previous *State of the Climate* reports). This upper ocean fresh anomaly increased density stratification and stabilized the upper ocean, which, together with surface-intensified warming of marine heat waves in the area that occurred in 2013–15 (e.g., Gentemann et al. 2017) and again in 2019–20 (Scannell et al. 2020), perhaps prolonging and amplifying especially the second event (Scannell et al. 2020; Sidebar 3.1).

Elsewhere in the Pacific Ocean, the fresh 2020 SSS anomaly (Fig. 3.7a) observed over much of the ITCZ and South Pacific Convergence Zone and extending north of Hawaii in the Central Pacific began around 2015 (see previous *State of the Climate* reports). In contrast, the more recent strong increase in salinity along the equator from 150°E to the dateline from 2019 to 2020 (Fig. 3.7b) is owing to the westward migration of the fresh pool with the advent of La Niña in 2020 (section 4b), linked to the anomalous westward currents across the equator in 2020 (see Fig. 3.18a), as well as westward shifts in precipitation in the region (see Fig. 3.12d).

There was mostly freshening of SSS from 2019 to 2020 in the tropical Atlantic ITCZ (punctuated by areas of strong salinification north of Brazil and Colombia) and in the Gulf of Guinea (Fig. 3.7b). Elsewhere in the Atlantic in 2020, as in many previous years, the relatively fresh regions

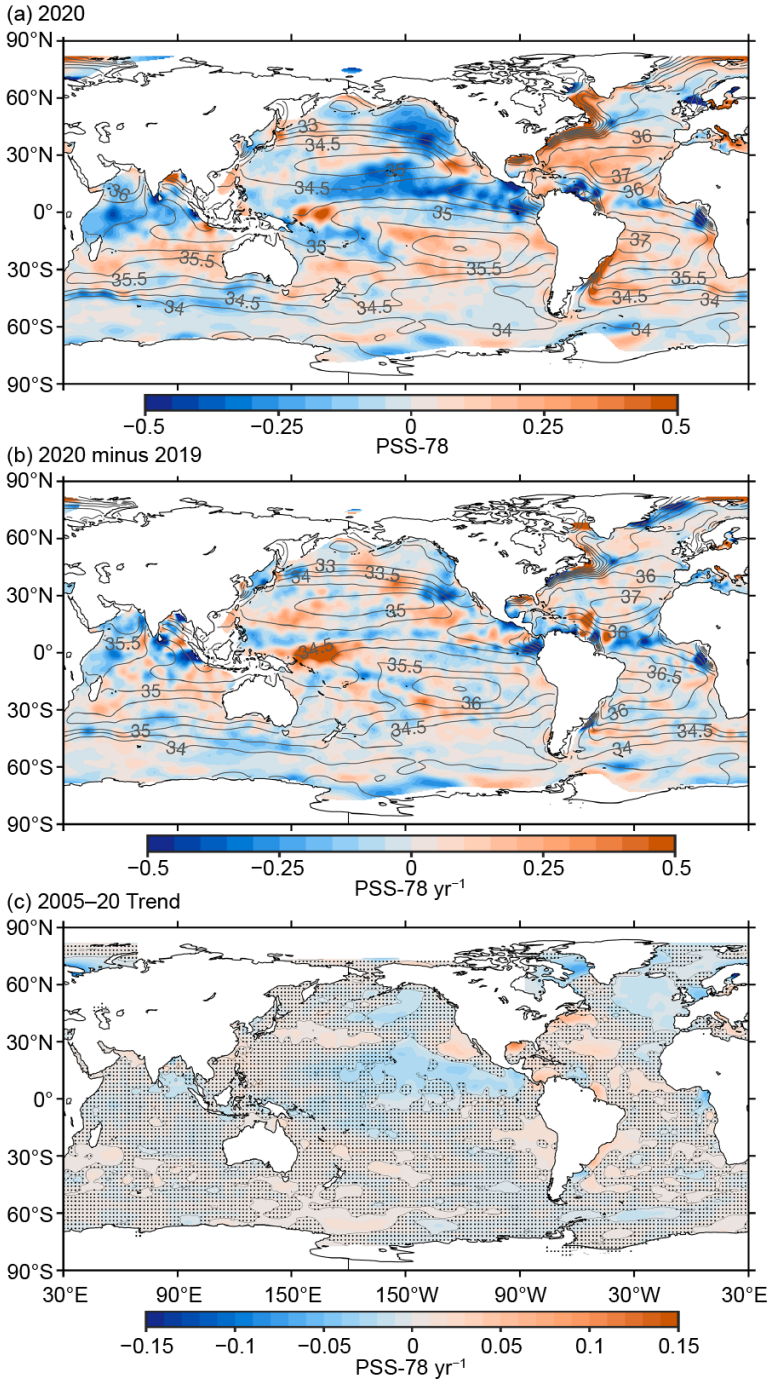

Fig. 3.7. (a) Map of the 2020 annual surface salinity anomaly (colors, PSS-78) with respect to monthly climatological 1955–2012 salinity fields from WOA13v2 (yearly average—gray contours at 0.5 intervals, PSS-78). (b) Difference of 2020 and 2019 surface salinity maps (colors, PSS-78 yr^{-1}). White ocean areas are too data-poor (retaining <80% of a large-scale signal) to map. (c) Map of local linear trends estimated from annual surface salinity anomalies for 2005–20 (colors, PSS-78 yr^{-1}). Areas with statistically insignificant trends at 5%–95% confidence are stippled. All maps are made using Argo data.

(subpolar North Atlantic and under the ITCZ) were fresher than climatology, and the relatively saltier regions (the subtropics) were saltier than climatology (Fig. 3.7a) These salty signals appear to be especially strong just off the east coasts of North and South America.

Freshening in much of the tropical Indian Ocean from 2019 to 2020 (Fig. 3.7b) left most of that region fresher than climatology in 2020 (Fig. 3.7a). In a warming climate, the atmosphere can hold more water, leading to expectations of more evaporation in regions where evaporation is dominant over precipitation and more precipitation where precipitation exceeds evaporation (Held and Soden 2006; Durack and Wijffels 2010). In the ocean this translates to "Salty gets saltier and fresh gets fresher." This pattern has been evident in *State of the Climate* reports going back as far as 2006, the first year of the SSS section. In 2020, salty SSS anomalies are associated with the subtropical salinity maxima in the South Indian, the South Pacific, and the North and South Atlantic Oceans (Fig. 3.7a), with fresh SSS anomalies in the subpolar North Pacific, the eastern subpolar North Atlantic, and the ITCZs of the Pacific and Atlantic. The 2005–20 SSS trends (Fig. 3.7c) reflect this pattern to some extent as well, although the portions with trends statistically different from zero at the 5%–95% confidence limits (Fig. 3.7c, unstippled areas) are somewhat limited. Still, there are statistically significant freshening trends evident in the subpolar North Pacific and North Atlantic, the Bay of Bengal, and the Pacific ITCZ. There are also statistically significant salty trends in parts of the subtropics in all basins. The salty trends in the stratocumulus deck regions west of California and Chile are interesting, as they are, to the best of our knowledge, unexplained.

In 2020, the seasonal BASS (Xie et al. 2014) SSS anomalies (Fig. 3.8) show the year-round persistence of fresh SSS anomalies in the North Pacific subpolar and tropical regions and salty SSS anomalies in the subtropics of all the other basins. The western equatorial Pacific starts

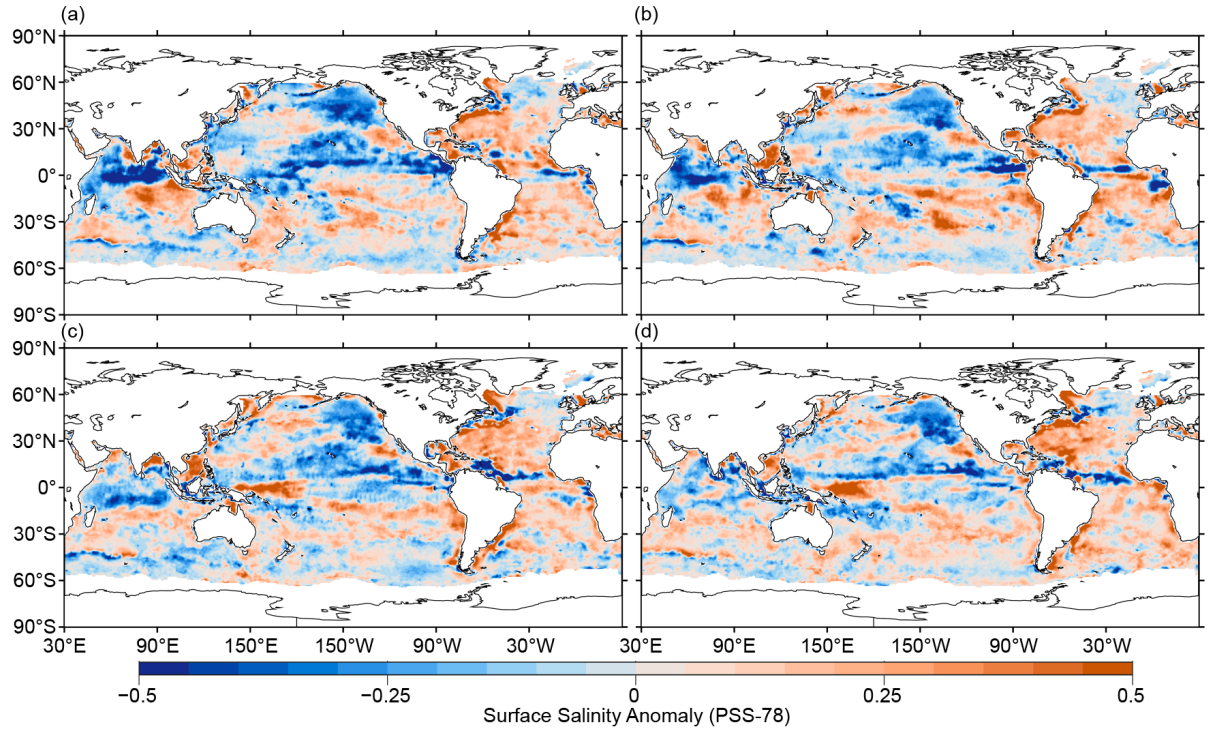

Fig. 3.8. Seasonal maps of SSS anomalies (PSS-78; colors) from monthly blended maps of satellite and in situ salinity data (BASS; Xie et al. 2014) relative to monthly climatological 1955–2012 salinity fields from WOA13v2 for (a) DJF 2019/20, (b) MAM 2020, (c) JJA 2020, and (d) SON 2020. Areas with maximum monthly errors exceeding 10 PSS-78 are left white.

out anomalously fresh, but becomes increasingly anomalously salty throughout the year with the advent of La Niña. Similarly, much of the tropical Indian Ocean becomes progressively less anomalously fresh during 2020. In the tropical Atlantic, fresh anomalies build in the Gulf of Guinea in boreal spring 2020 and north and east of the Orinoco and Amazon Rivers in boreal summer and autumn 2020. With their higher spatial and temporal resolution, BASS data also reveal some features like the fresh anomaly near the North Atlantic Current that are not as readily apparent in the Argo maps.

3) Subsurface salinity—J. Reagan, T. Boyer, C. Schmid, and R. Locarnini

Salinity anomalies originating near the surface of the ocean often propagate into the ocean's interior through mixing or through the sinking of water masses along isopycnals. Thus, subsurface salinity anomalies can often be used as a tracer for what has happened at the surface. Here we analyze salinity in the three main ocean basins (Atlantic, Pacific, and Indian) from 64.5°S to 65.5°N with definitions following World Ocean Atlas 2018 conventions (https://www.ncei.noaa.gov/data/oceans/woa/WOA18/MASKS/basinmask_01.msk).

The 0–1000-m Atlantic basin-average monthly salinity anomalies for 2011–20 exhibit large positive anomalies (>0.05) near the surface that weaken with depth to ~0.01 at 600 m (Fig. 3.9a), a pattern that has persisted for over a decade and continued in 2020. From 2019 to 2020 there was salinification (≥0.015) from 50 to 125 m (Fig. 3.9b), with little change above and below. Thus, the surface salinification between 2018 and 2019 (Reagan et al. 2020) appears to have deepened to ~100 m between 2019 and 2020. Statistically significant (>1 std. dev.) changes in zonally averaged salinity anomalies in the Atlantic (Fig. 3.9c) between 2019 and 2020 reveal large freshening (<−0.15) around 8°N in the upper 30 m and weaker freshening (~−0.03) in the upper 100 m near 35°S. Significant salinification (>0.03) is centered at 40°S and extends from the surface to 500 m. Additional salinification (>0.06) extends from the surface to 100-m depth centered at 45°N with subsurface pockets of salinification (>0.03) from 50 to 150 m between 5°N and 30°N.

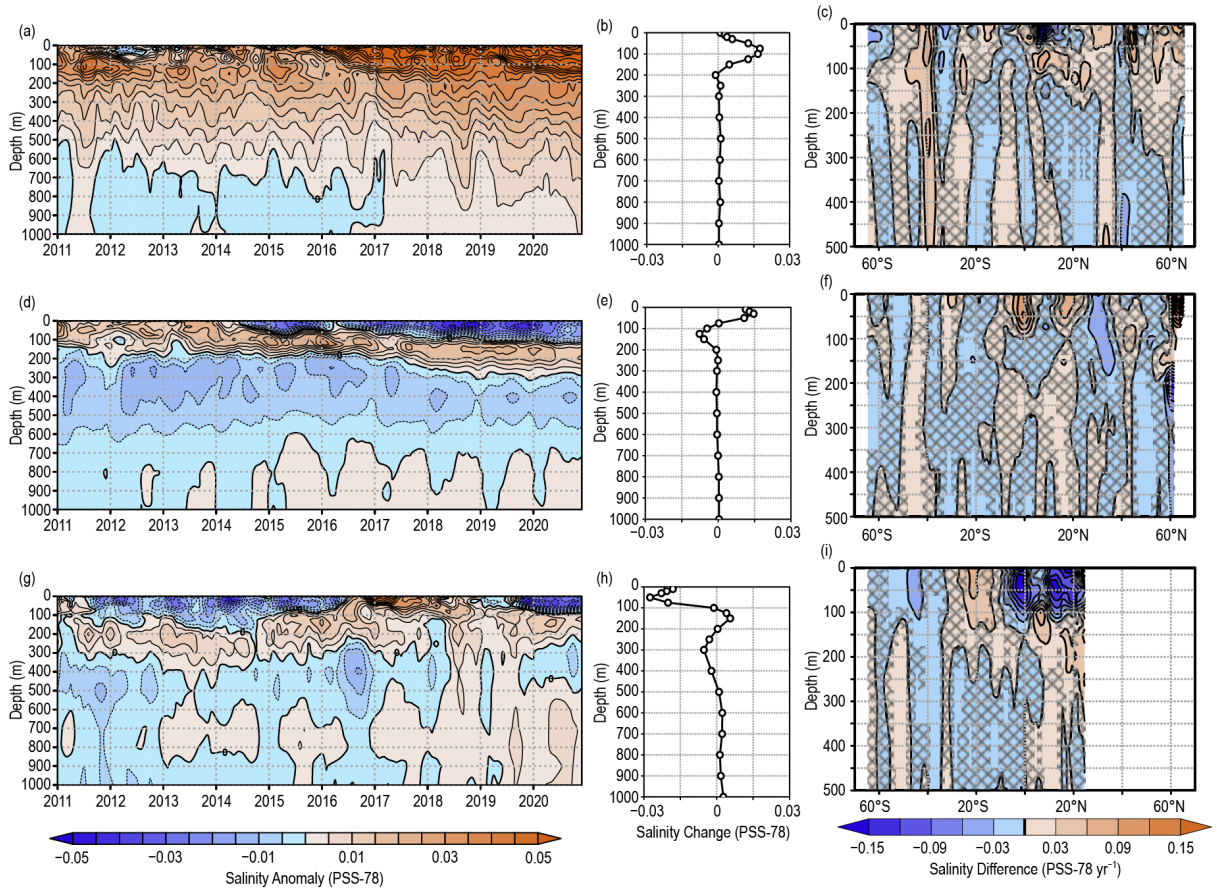

Fig. 3.9. Average monthly salinity anomalies from 0–1000-m depth for 2011–20 for the (a) Atlantic, (d) Pacific, and (g) Indian Ocean basins. Change in salinity from 2019 to 2020 for the (b) Atlantic, (e) Pacific, and (h) Indian Ocean basins. Change in the 0–500-m zonal-average salinity from 2019 to 2020 in the (c) Atlantic, (f) Pacific, and (i) Indian Ocean basins with areas of statistically insignificant change, defined as <±1 std. dev. and calculated from all year-to-year changes between 2005 and 2020, stippled in dark gray. Data were smoothed using a 3-month running mean. Anomalies are relative to the long-term (1955–2012) WOA13v2 monthly salinity climatology (Zweng et al. 2013).

The 2020 basin-average monthly salinity anomalies for the Pacific continued the persistent pattern that has been evident since mid-2014 (Fig. 3.9d). In 2020, fresh anomalies (<−0.01) dominated the upper 100 m, with salty anomalies (>0.01) between 125 and 250 m, and fresh anomalies (<−0.01) between 350 and 550 m. Changes from 2019 to 2020 (Fig. 3.9e) reveal salinification in the upper 75 m (peak of ~0.015 at 30 m) with freshening from 75 to 200 m (peak of ~−0.0075 at 125 m). The zonally averaged salinity changes from 2019 to 2020 (Fig. 3.9f) in the Pacific reveal significant salinification (>0.06) in the upper 100 m centered at three latitudes: 0°, 15°N, and 62°N. Significant freshening (<−0.03) occurred between the surface and 175 m between 27°N and 37°N and in a subsurface pocket between 175- and 275-m depths at 60°N.

Throughout 2020 in the Indian basin there were large (<−0.025) fresh anomalies in the upper 75 m with salty anomalies (>0.005) between 100- and 200-m depths (Fig. 3.9g). Similar to the salinity tendency exhibited from 2018 to 2019 (Reagan et al. 2020), there was strong freshening in the upper 100 m (peak of ~−0.028 at 50 m) from 2019 to 2020 (Fig. 3.9h). Additionally, there was salinification between 100- and 200-m depths (peak ~0.0065 at 150 m) and more freshening between 200- and 500-m depths (peak ~−0.0065 at 300 m). The 2019 to 2020 changes in zonally averaged salinity anomalies in the Indian basin reveal significant freshening (<−0.06) in the upper 100 m from ~6°S to 23°N, which was likely the result of enhanced precipitation over the eastern Indian basin associated with the 2020 La Niña event (see Fig. 3.12). Additional significant freshening (<−0.03) near 45°S from the surface to 100 m is also evident. Significant salinification (>0.03) occurred between 0 and 125-m depths between 25°S and 15°S and in two subsurface

pockets centered at 100 m and ~7°N and at 200 m and 22°N, respectively.

Figure 3.10 shows the 2005–20 basin average salinity trends for the three oceans. The Atlantic reveals significant salinification trends throughout the 0–1000-m water column, with maximum values of 0.04 decade^{-1} at the surface. The Pacific experienced significant freshening trends from 0 to 50 m (peak of ~–0.02 decade^{-1} at 20 m), with salinification trends between 75 and 250 m (peak of ~0.018 decade^{-1} at 150 m). The Indian Ocean experienced significant subsurface salinification trends with a peak at 125 m (0.01 decade^{-1}). The near-surface freshening in the Pacific (precipitation-dominated basin) and salinification in the Atlantic (evaporation-dominated basin) supports the idea that the hydrological cycle is amplifying in a warming world (Held and Soden 2006) and can be traced by changes in salinity (Durack 2015). Furthermore, a recent study by Li et al. (2020) shows that the ocean has become increasingly stratified over the last half century, which has been primarily due to ocean temperatures rising faster at the surface than below, creating less dense surface water. Based on the 2005–20 trend analysis, the Atlantic salinity trends have worked to destabilize the water column as salinity (and therefore density) increases the most at the surface, whereas the Pacific and Indian salinity trends have worked in conjunction with the temperature trends to stabilize the water column as there is freshening at the surface (decreasing density) and salinification below (increasing density).

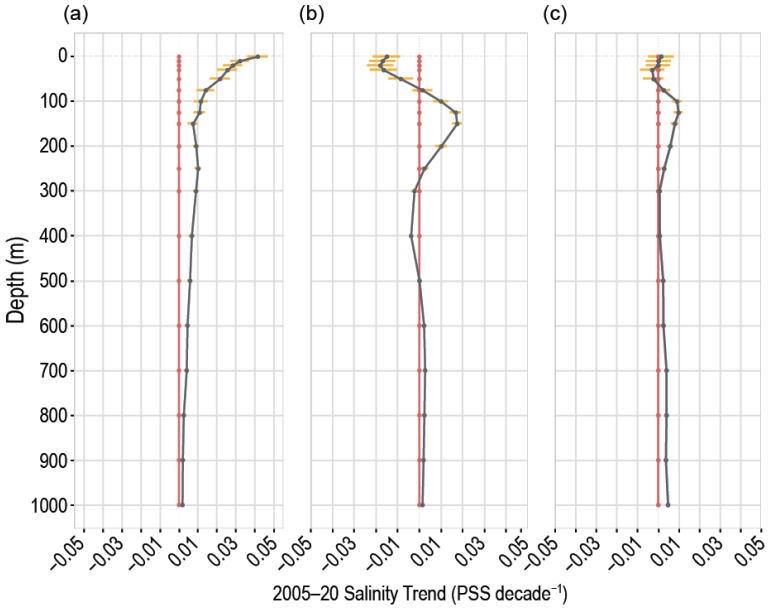

Fig. 3.10. Basin-average salinity trends from 2005 to 2020 (black line, PSS-78 decade^{-1}) with 95% confidence intervals (orange bars) at standard depths for (a) Atlantic, (b) Pacific, and (c) Indian Ocean basins. Red line is the zero-trend line.

e. Global ocean heat, freshwater, and momentum fluxes—L. Yu, P. W. Stackhouse, A. C. Wilber, C. Wen, and R. A. Weller

The ocean and atmosphere exchange heat, freshwater, and momentum at the surface. These air–sea fluxes are the primary mechanisms for keeping the global climate system in balance with the incoming insolation at Earth's surface. Most of the shortwave radiation (SW) absorbed by the ocean's surface is vented into the atmosphere by three processes: longwave radiation (LW), turbulent heat loss by evaporation (latent heat flux, or LH), and conduction (sensible heat flux, or SH). Heat is stored in the ocean and transported by the ocean circulation, forced primarily by wind stress. Evaporation connects heat and moisture transfers, and the latter, together with precipitation, determines the local surface freshwater flux. Identifying changes in air–sea fluxes is essential in deciphering observed changes in ocean water properties and transport of mass, freshwater, and heat.

We examined air–sea heat flux, freshwater flux, and wind stress in 2020 and their relationships with ocean surface variables. The net surface heat flux is: Qnet = SW+LW+LH+SH. The net surface freshwater flux into the ocean (neglecting riverine and glacial fluxes from land) is precipitation (P) minus evaporation (E). Wind stress is computed from satellite wind retrievals using the bulk parameterization Coupled Ocean-Atmosphere Response Experiment (COARE) version 3.5 (Fairall et al. 2003). We produce global maps of Qnet, $P-E$, and wind stress (Figs. 3.11–3.13) and the long-term perspective of the change of the forcing functions (Fig. 3.14) by integrating efforts of multiple groups. Ocean-surface LH, SH, E, and wind stress are from the Objectively Analyzed air-sea Fluxes (OAFlux) project's high-resolution products (Yu and Weller 2007). Surface SW and LW radiative fluxes are from the Clouds and the Earth's Radiant Energy Systems (CERES) Fast Longwave And Shortwave Radiative Fluxes (FLASHFlux) version

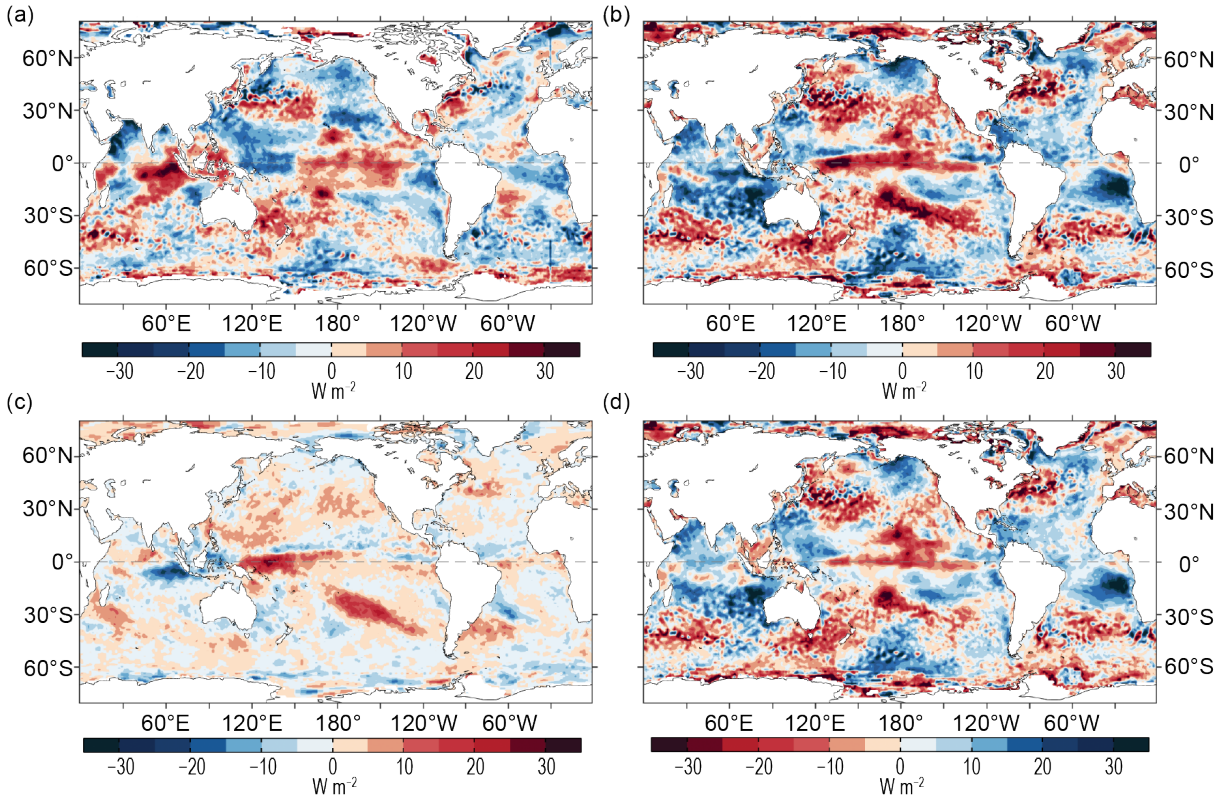

Fig. 3.11. (a) Surface heat flux (Qnet) anomalies for 2020 relative to the 2001–15 climatology. Positive values denote ocean heat gain. (b) 2020 minus 2019 difference for Qnet, (c) surface radiation (SW+LW), and (d) turbulent heat fluxes (LH+SH), respectively. Positive changes denote more ocean heat gain in 2020 than in 2019, consistent with the reversal of the color scheme in (d). All units are given in W m^{-2}. LH+SH are from OAFlux, and SW+LW is the NASA FLASHFlux version 4A.

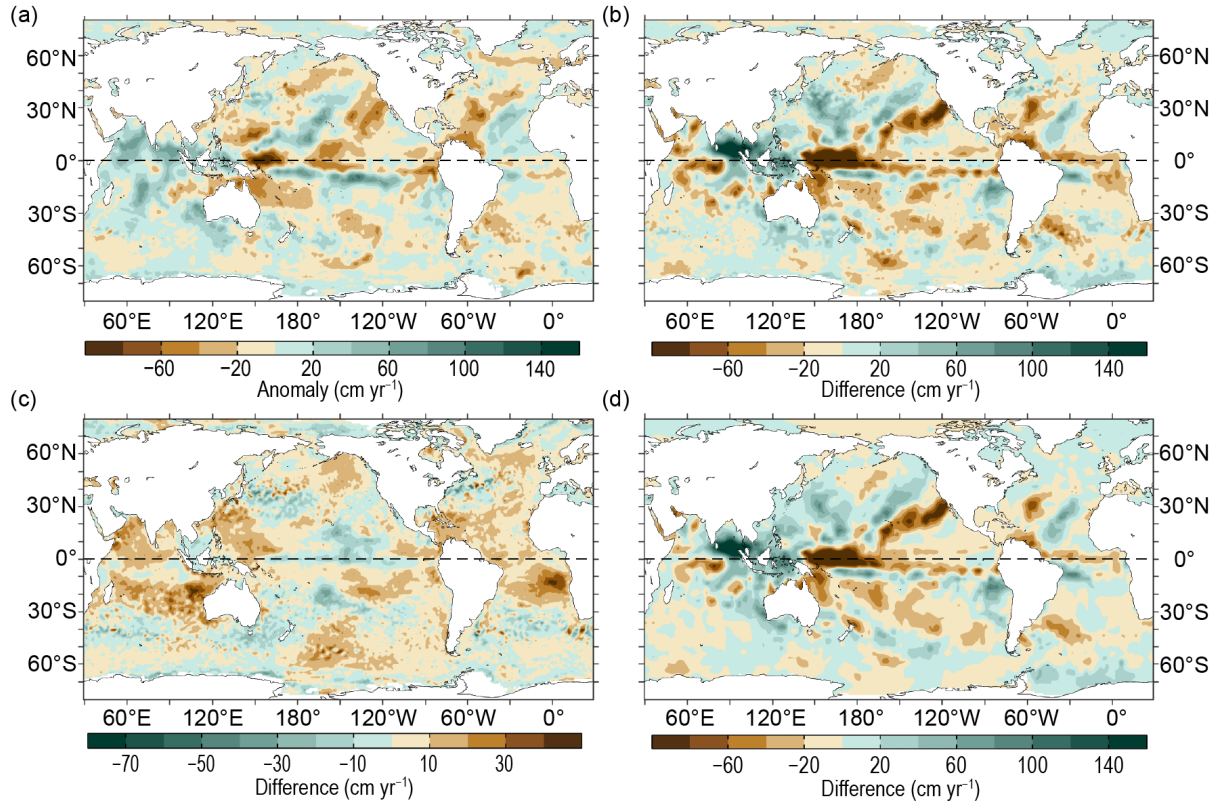

Fig. 3.12. (a) Surface freshwater *(P−E)* flux anomalies for 2020 relative to the 1988–2015 climatology. 2020 minus 2019 difference for (b) *P−E*, (c) evaporation (*E*), and (d) precipitation (*P*). Green colors denote anomalous ocean moisture gain, and browns denote loss, consistent with the reversal of the color scheme in (c). All units are given in cm yr^{-1}. *P* is the GPCP version 2.3rB1 product, and *E* is from OAFlux.

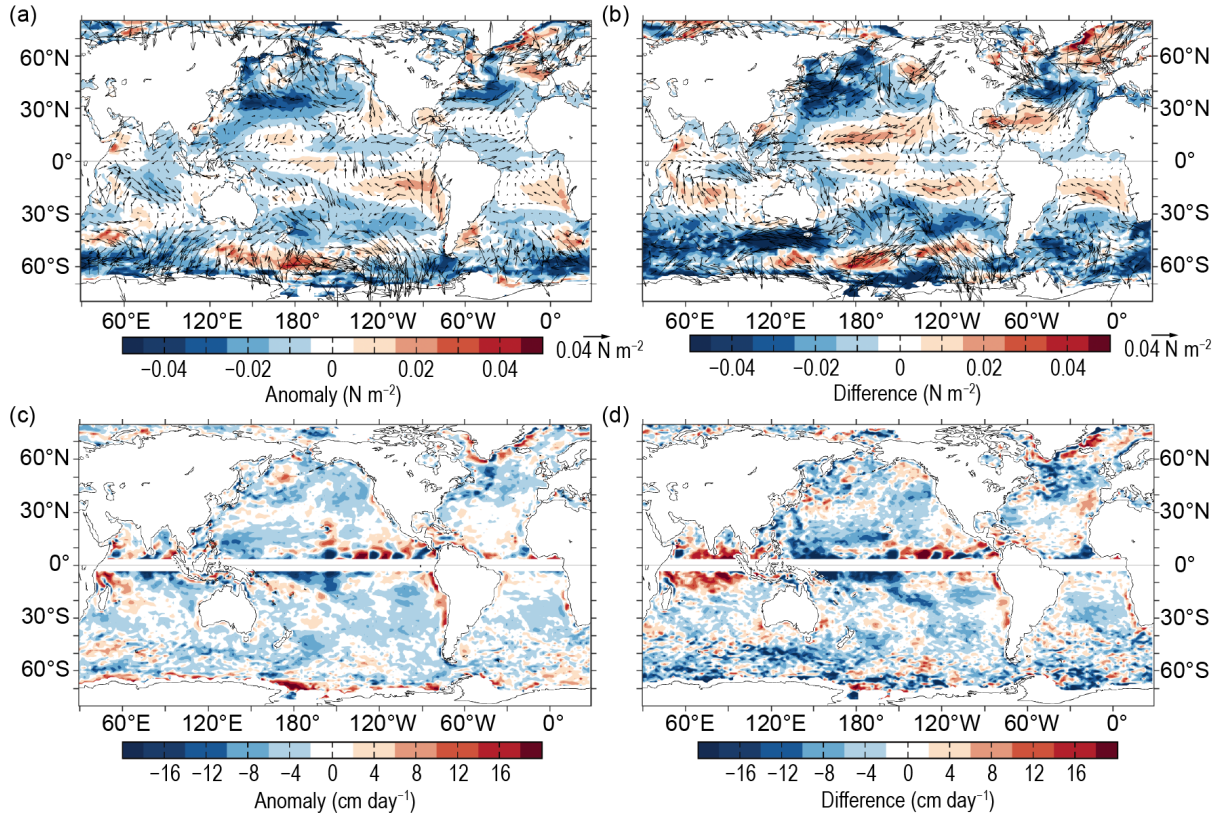

Fig. 3.13. (a) Wind stress magnitude (colors) and vector anomalies for 2020 relative to the 1988–2015 climatology, (b) 2020 minus 2019 difference in wind stress (N m^{-2}), (c) Ekman vertical velocity anomalies (W_{EK}; cm day^{-1}) for 2020 relative to the 1988–2015 climatology, and (d) 2020 minus 2019 difference in W_{EK} (cm day^{-1}). In (c) and (d), positive values denote upwelling tendency and negative downwelling tendency. Winds are computed from the OAFlux.

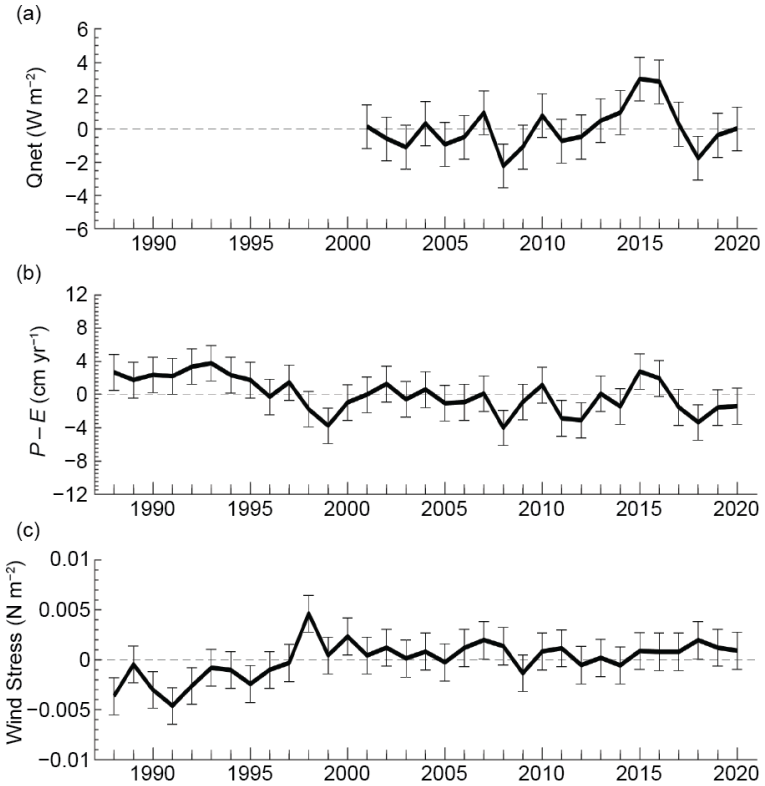

4A product (Stackhouse et al. 2006). Global P is from the Global Precipitation Climatology Project (GPCP) version 2.3 products (Adler et al. 2018). The CERES Energy Balanced and Filled (EBAF) surface SW and LW version 4.1 products (Loeb et al. 2018; Kato et al. 2018) are used in the time series analysis.

1) Surface heat fluxes

The ocean received anomalous net heat (Qnet anomalies) in 2020 (Fig. 3.11a) from the atmosphere (positive anomalies) in the eastern equatorial Indian Ocean (>30 W m^{-2}), the central and eastern equatorial Pacific (~10 W m^{-2}), the western North Pacific around 30°N (~10 W m^{-2}), the northwest subtropical Atlantic (~10 Wm^{-2}), and the midlatitude Southern Ocean 30°–50°S (~10 W m^{-2}). The regions where the ocean had pronounced anomalous heat loss to

Fig. 3.14. Annual-mean time series of global averages of (a) net surface heat flux (Qnet; W m^{-2}) from the combination of CERES EBAF4.1 SW+LW and OAFlux LH+SH. The 2020 Qnet estimate is based on FLASHFlux and OAFlux. (b) net freshwater flux ($P-E$; cm yr^{-1}) from the combination of GPCP P and OAFlux E, and (c) wind stress magnitude (N m^{-2}) from OAFlux. Shaded area denotes 1 std. dev. of annual mean variability.

the atmosphere include the Arabian Sea (<–25 W m^{-2}), the western tropical Pacific (~–20 W m^{-2}), the subtropical eastern North Pacific (~–20 W m^{-2}), and the tropical South Atlantic Ocean (~–15 W m^{-2}).

The 2020 minus 2019 Qnet differences (Fig. 3.11b) in the tropical Pacific reflect the transition from a weak El Niño in 2019 to a moderate La Niña in 2020 (see section 4b; compare Fig. 3.11b to sea surface temperature [SST] differences in Fig. 3.1b). Cool SST anomalies were damped by increased ocean heat uptake. In general, Qnet differences were dominated by the LH+SH difference (Fig. 3.11d), though both LH+SH and SW+LW (Fig. 3.11c) showed similar structures over most of the global ocean. Furthermore, SW+LW increases were dominant in the western equatorial Pacific and the central South Pacific, with increases in the region extending from the western equatorial Pacific to the southeastern Pacific, but maximum magnitude (~10 W m^{-2}) confined in a northwest-southeast tilted band between the dateline and 120°W. LH+SH showed a similar warming tendency in the central equatorial Pacific and the center of the South Pacific, induced primarily by a weakened LH heat loss (–10 Wm^{-2}).

Outside of the equatorial Pacific, both SW+LW and LH+SH 2020 minus 2019 differences produced an anomalous warming along 40°–50°S in the Southern Ocean, in the vicinity of the Kuroshio–Oyashio Extension in the North Pacific, and in a large area in the eastern North Pacific (170°E–150°W, 20°–40°N). In the latter, the band of SW+LW warming tendencies (~5 W m^{-2}) was likely caused by a reduction of clouds in 2020 relative to 2019. This location was on the southern edge of the 2019–20 northeast Pacific marine heatwave (MHW; Fig. 3.1; Sidebar 3.1), where LH+SH also showed warming tendencies (~10 W m^{-2}) due to the weakened LH loss.

In the tropical Indian Ocean, the 2020 minus 2019 Qnet differences revealed anomalous ocean cooling. As the 2020 minus 2019 SST differences (Fig. 3.1b) were mostly negative in the western half of the Indian Ocean, there seems to be a causality relationship between the Qnet forcing and SST. On the other hand, the SST differences in the eastern Indian Ocean did not have the same sign as Qnet.

In the Atlantic Ocean, there was a tripole-like difference pattern of Qnet featuring Qnet increases in the Gulf Stream and extension and Qnet decreases elsewhere between 30°S and 60°N (Fig. 3.11d). The subpolar North Atlantic (north of 60°N) and the South Atlantic (south of 30°S) gained heat (~10–15 W m^{-2}) from the atmosphere in 2020. The source of heating was attributable primarily to the reduced LH+SH and secondly to the net radiative heating (<5 W m^{-2}) in these regions.

2) Surface freshwater fluxes

The 2020 $P-E$ anomalies (Fig. 3.12a) reflect a basin-wide increase in the net freshwater input (~20 cm yr^{-1} on average) to the tropical Indian Ocean (positive anomalies with green colors; a freshening effect on the ocean), consonant with a local reduction of sea surface salinity (SSS; see Fig. 3.7a). The net freshwater input reduced (negative anomalies with brown colors; salinification effect on the ocean) in the eastern North Pacific and the western North Atlantic and increased in a few other regions, such as the zonal freshening band just south of the equator in the Pacific and the tilted southwest-northeast freshening bands in the central North Pacific and North Atlantic. The maximum $P-E$ reduction (~80 cm yr^{-1}) occurred in the western equatorial Pacific where SSS increased dramatically (see Fig. 3.7b).

The 2020 minus 2019 $P-E$ difference pattern in the tropical Pacific (Fig. 3.12b) resembles that of the net surface radiation (SW+LW) difference pattern (Fig. 3.11b), with the bands of the reduced $P-E$ value coinciding with the bands of increased SW+LW values. The $P-E$ tendencies are attributable to the P tendencies (Fig. 3.12d), showing that SW+LW increased in areas of reduced rainfall and conversely, SW+LW reduced in areas of increased rainfall. Outside of the tropics, the largest evaporative tendencies occurred in the eastern subtropical North Pacific (~80 cm yr^{-1}), resulting from the reduction of P. This freshwater deficit was concurrent with increased SW+LW tendencies (Fig. 3.11c).

3) Wind stress

Midlatitude westerly winds became weaker (negative wind stress anomalies; Fig. 3.13a) in 2020 in both Northern and Southern Hemispheres (NH and SH). In the North Pacific and North Atlantic Oceans, marked reduction of westerly winds occurred along 30°–40°N and the magnitude of negative anomalies was <0.04 N m^{-2}. In the SH, negative wind anomalies developed on the southern edge of the westerly winds along 50°–60°S in the eastern Pacific, and the Atlantic and Indian sectors (from 120°W to 120°E), with anomalies reaching −0.04 N m^{-2} in several locations. However, the change of the westerly winds was not uniform across the circumpolar region; for instance, the westerly winds actually became stronger in the western Pacific sector. Winds also became stronger in the subpolar North Atlantic Ocean, where winds are predominantly easterlies.

The trade winds in 2020 strengthened (<0.025 N m^{-2}) in the central tropical Pacific as expected with the transition to La Niña (see section 4b), as well as the southern tropical Pacific and Atlantic. In the North Indian Ocean, winds over the Arabian Sea accelerated while winds over the Bay of Bengal slowed down.

The 2020 minus 2019 wind stress difference map (Fig. 3.13b) further shows that the most noted changes in winds are the strengthening of the trade winds in the three tropical basins, the weakening of the westerly winds in the midlatitude NH and SH, and the strengthening of the easterly winds in the subpolar North Atlantic. Surface winds were stronger in the Gulf of Alaska associated with the evolving MHW (Sidebar 3.1).

Winds vary considerably in space. The spatial variations of winds cause divergence and convergence of the Ekman transport, leading to a vertical velocity, denoted by Ekman pumping (downward) or suction (upward) velocity W_{EK}, at the base of the Ekman layer. Computation of W_{EK} follows the equation: $W_{EK} = 1/\rho\nabla\cdot(\tau/f)$, where ρ is the water density and f the Coriolis force. The 2020 W_{EK} anomaly pattern (Fig. 3.13c) is dominated by large downwelling (negative) anomalies in the tropical South Indian Ocean and tropical South Pacific Ocean, with maximum magnitude of ~−16 cm yr^{-1}. The change indicates a weakening of the typical upwelling conditions in the former and a strengthening of the typical downwelling conditions in the latter. Outside of the tropical region, the 2020 W_{EK} anomalies were generally weak and less organized. The 2020 minus 2019 W_{EK} difference pattern (Fig. 3.13d) suggests the resuming of the typical upwelling conditions in the equatorial Indian Ocean after the end of the major 2019 positive Indian Ocean dipole event (see Fig. 3.1b), with its anomalously warm waters in the western Indian Ocean, and cool waters in the east.

4) Long-term perspective

A long-term perspective on the change of ocean surface forcing functions in 2020 is examined in the context of multi-decade annual mean time series of Qnet, $P-E$, and wind stress averaged over the global ice-free oceans (Figs. 3.14a–c). The Qnet time series commences in 2001, when CERES EBAF4.1 surface radiation products begin. The $P-E$ and wind stress time series are each 33 years long, starting from 1988 when higher quality global flux fields can be constructed from Special Sensor Microwave/Imager (SSM/I) satellite retrievals. Qnet anomalies are relative to the 2001–15 climatology, and positive anomalies denote increased net downward heat flux into the ocean that has a warming effect on the ocean. $P-E$ anomalies are relative to the 1988–2015 climatology, and positive anomalies denote increased freshwater flux into the ocean that causes sea surface freshening. Wind stress anomalies are relative to the 1988–2015 climatology, and positive anomalies denote increased wind stress magnitude over the ocean.

Qnet did not change significantly between 2001 and 2007 but had large interannual fluctuations thereafter. The total downward heat flux into the global ocean increased by about 3 W m^{-2} during 2011–16, when the tropical Pacific switched from a strong La Niña event in 2011 to a strong El Niño event in 2015–16. This period of increasing oceanic heat gain coincided with an increase of the global mean SST by about 0.35°C (Fig. 3.3a). Qnet went up slightly in 2019 after a

sharp reduction of about 4 W m^{-2} during the 2017–18 La Niña, and the 2020 Qnet remained at a similar level to its 2019 value. The $P - E$ time series shows similar interannual variability to that of the Qnet time series, with the 2020 level more or less the same as the 2019 level. The time series of wind stress was flat in the recent two decades after a regime shift around 1999, and the 2020 winds were slightly but not significantly down from the 2019 level. The error bars in the time series represent one standard deviation of year-to-year variability.

f. Sea level variability and change—P. R. Thompson, M. J. Widlansky, E. Leuliette, W. Sweet, D. P. Chambers, B. D. Hamlington, S. Jevrejeva, J. J. Marra, M. A. Merrifield, G. T. Mitchum, and R. S. Nerem

Global mean sea level (GMSL) during 2020 had the highest annual average in the satellite altimetry record (1993–2020), 91.3 mm above 1993 (Fig. 3.15a). This marks the ninth consecutive year (and 25th out of the last 27) that GMSL increased relative to the previous year. The new high reflects an ongoing multi-decadal trend of 3.3 ± 0.4 mm yr^{-1} in GMSL during the satellite altimetry era (Fig. 3.15a). A quadratic fit with corrections for the eruption of Mt. Pinatubo (Fasullo et al. 2016) and El Niño-Southern Oscillation effects (Hamlington et al. 2020) yields an average (1993–2020) climate-driven trend of 3.0 ± 0.4 mm yr^{-1} and acceleration of 0.081 ± 0.025 mm yr^{-2} (updated from Nerem et al. 2018).

Variations in GMSL (Fig. 3.15a) result from changes in both the mass and density of the global ocean (Leuliette and Willis 2011; Chambers et al. 2017). The steric (i.e., density-related) sea level rise rate observed by the Argo profiling float array during 2005–20, 1.4 ± 0.2 mm yr^{-1}, which is mostly due to ocean warming, accounted for about one-third of the GMSL trend of 3.7 ± 0.4 mm yr^{-1} since 2005. Increasing global ocean mass observed by the NASA Gravity Recovery and Climate Experiment (GRACE) and GRACE Follow-On (GRACE-FO) missions, contributed the remaining two-thirds, 2.6 ± 0.4 mm yr^{-1}, of the GMSL trend during 2005–20. The positive trend in ocean mass primarily resulted from melting of glaciers and ice sheets (see sections 5e, 6d, 6e) with a small contribution, 0.3 ± 0.1 mm yr^{-1}, from terrestrial water storage (Frederikse et al. 2020; a decrease in terrestrial storage will cause an increase in sea level).

Annually averaged GMSL from satellite altimetry increased by 3.5 mm from

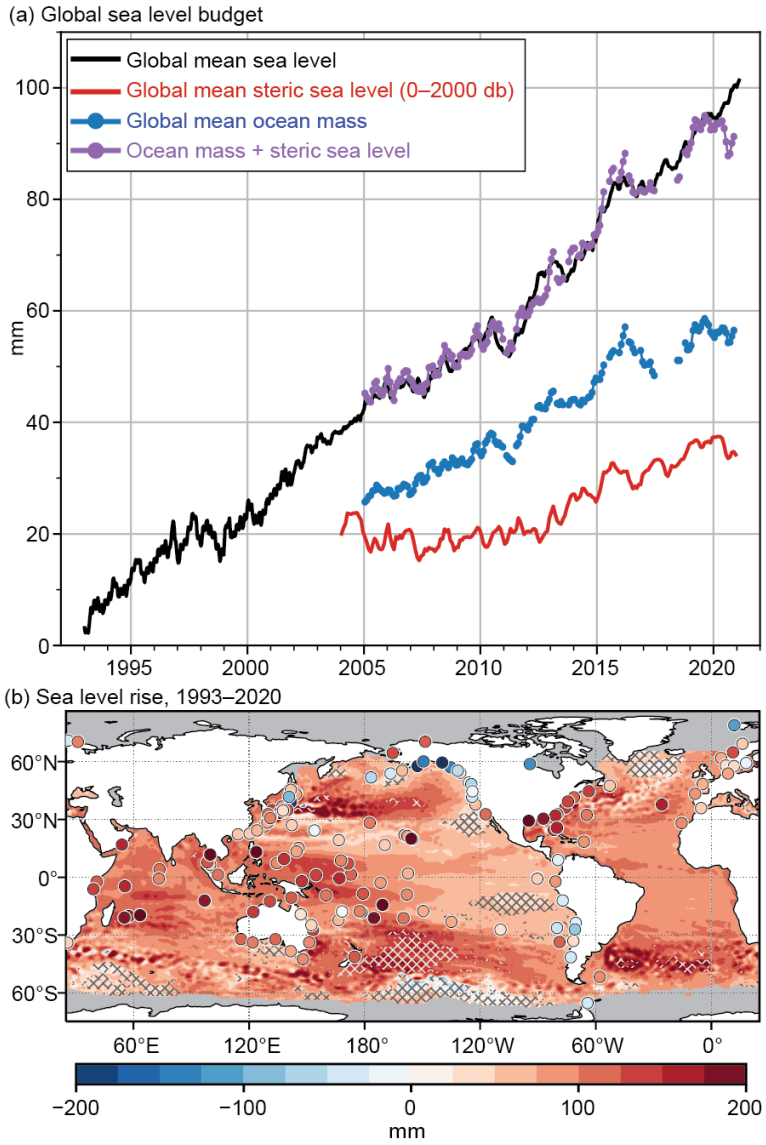

Fig. 3.15. (a) Monthly averaged GMSL (mm) observed by satellite altimeters (black, 1993–2020 from the NOAA Laboratory for Satellite Altimetry), global ocean mass (blue, 2005–20 from GRACE and GRACE-FO), global mean steric sea level (red, 2004–20 from the Argo profiling float array), mass plus steric (purple), and inferred global ocean mass (blue) calculated by subtracting global mean steric sea level from global mean sea level. All time series have been smoothed with a 3-month filter. (b) Total local sea level change during 1993–2020 as measured by satellite altimetry (contours) and tide gauges (circles). Hatching indicates local changes that are significantly different from the change in GMSL.

2019 to 2020 (Fig. 3.15a) while annual global mean steric sea level observed by Argo (0–2000 m) decreased by 0.75 mm from 2019 to 2020 (Fig. 3.15a). The decrease in global mean steric sea level contrasts with the estimated year-over-year increase in the globally integrated ocean heat content anomaly (OHCA; 0–2000 m) from an ensemble of OHCA products (see section 3c). One of the five estimates (e.g., the NCEI estimate, Fig. 3.6) shows little globally integrated OHCA change from 2019 to 2020 and is not inconsistent with the year-over-year reduction in total steric sea level given a modest salinification of the global ocean. Annual global ocean mass from GRACE-FO decreased by 1.0 mm from 2019 to 2020, which was primarily due to anomalous precipitation in eastern Africa during 2020 and associated terrestrial water storage there (see sections 2d4, 2d9, 7e4).

The sea level budget based on observations from altimetry, Argo, and GRACE-FO did not close during 2020 as annually averaged GMSL measured by satellite altimeters diverged from the sum of the independently estimated steric and mass contributions by more than 5 mm (Fig. 3.15a). Previous discrepancies in the global sea level budget coincided with the failure of an accelerometer onboard the original GRACE mission (Chen et al. 2020). A similar issue may be affecting recent observations from GRACE-FO, because one accelerometer has not functioned properly since launch. However, the reduction in global ocean mass during 2020 can be directly attributed to terrestrial water storage, which is known to produce fluctuations in global ocean mass (Boening et al. 2012). For 2020 specifically, the reduction in global ocean mass is linked to increased water storage in eastern Africa (see sections 2d, 7e4). Given this link, errors in altimetry and/or salty drift in Argo observations cannot be ruled out in accounting for recent discrepancies in the global sea level budget (Chen et al. 2020).

Spatial structure in sea level change over the 28-year altimeter record (Fig. 3.15b) is due to a combination of natural fluctuations in coupled modes of atmosphere–ocean variability (Han et al. 2017) and spatial structure in the response of the ocean to anthropogenic radiative forcing (Fasullo and Nerem 2018). It is difficult to disentangle these contributions to regional differences in sea level change (Hamlington et al. 2019), but salient features can be attributed to specific processes. For example, the east–west difference in sea level change across the Pacific (e.g., the more than 100 mm difference between Palau and Los Angeles) is associated with multidecadal variability in the strength of Pacific trade winds (e.g., Merrifield 2011). The region of enhanced sea level change in the high-latitude South Pacific can be attributed to regional warming of the ocean above 2000 m (Llovel and Terray 2016) and below 2000 m (Volkov et al. 2017). Sea level change relative to land (i.e., relative sea level, the quantity measured by tide gauges; red circles, Fig. 3.15b) is most relevant for societal impacts and can differ substantially from satellite-derived changes in tectonically active regions (e.g., Japan) and areas strongly affected by glacial isostatic adjustment (e.g., Alaska; Fig. 3.15b).

Due to long-term trends in GMSL (Fig. 3.15), annual sea level anomalies during 2020 were positive nearly everywhere (Fig. 3.16a). In the global tropics, the highest sea level anomalies were in the western Indian Ocean (10–15 cm above normal), whereas the lowest anomalies were in the central equatorial Pacific Ocean (0–5 cm). Sea level anomalies were positive across most of the subtropics (i.e., approximately within 20°–30° of the equator), except for small areas in the subtropical southern Indian Ocean, northwestern Pacific, and Gulf of Mexico Loop Current System where the 2020 sea levels were below normal. Each region of negative anomalies was near where some of the highest positive anomalies occurred in the tropical and subtropical latitudes (e.g., northeast of Madagascar, around Hawaii, and along the entire Gulf of Mexico Coast; anomalies 10–15 cm above normal). The 2020 annual mean anomalies were even higher in parts of the midlatitudes, such as in the extension regions of the Kuroshio and Gulf Stream Currents, although upwelling mesoscale eddy activity also contributed to small-scale areas of negative sea level anomalies.

Development of La Niña conditions during 2020 (see section 4b) explains most of the large-scale changes in the sea level compared to 2019 (Fig. 3.16b). Year-to-year sea level increases exceeding 15 cm occurred around parts of Indonesia and the Philippines (i.e., in the equatorial eastern

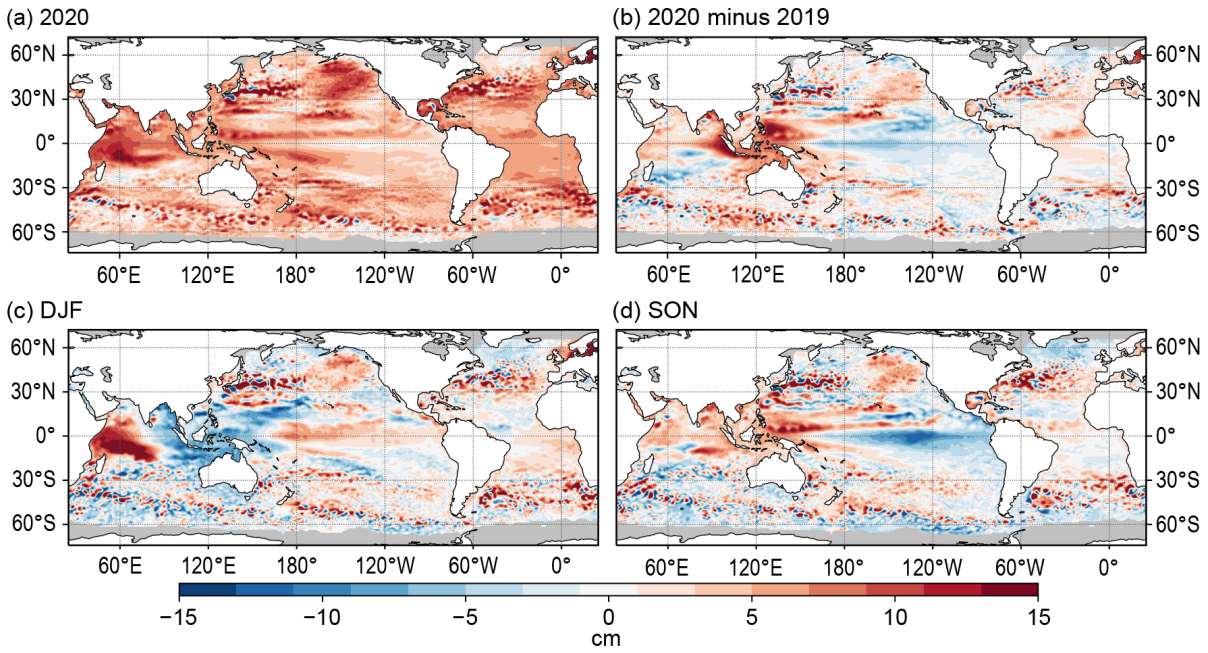

Fig. 3.16. (a) Annual average sea level anomaly during 2020 relative to average sea level at each location during 1993–2020. (b) Average 2020 minus 2019 sea level anomaly. (c) Average sea level anomaly during DJF 2020 relative to 1993–2020 average. (d) Same as (c), but for SON. All units are given in cm. GMSL was subtracted from panels (c),(d) to emphasize regional, non-secular change. Altimetry data were obtained from the gridded, multi-mission product maintained by Copernicus Marine and Environment Monitoring Service.

Indian Ocean and tropical northwestern Pacific Ocean, respectively), whereas in the central and eastern tropical Pacific, sea levels during 2020 were 5–10 cm lower relative to 2019. Elsewhere in the North Pacific Ocean, tendencies from 2019 to 2020 were for higher sea levels in a broad region centered around Hawaii (15 cm year-over-year increase) that extended both southwestward toward the Philippines and northeastward to near the U.S. West Coast. The shape of high sea level anomalies around Hawaii resembles the SST pattern associated with a positive Pacific Meridional Mode (Chiang and Vimont 2004), which is also indicative of weaker-than-normal trade winds in the region (Long et al. 2020), consistent with 2020 observations of wind stress (Fig. 3.13b). The 2020 minus 2019 sea level difference was also positive in the southwestern and south-central Pacific Ocean (greatest near 30°S), throughout most of the Atlantic Ocean including along almost the entire U.S. Gulf and East Coasts, and in the northern Indian Ocean (especially in the Bay of Bengal). Overall, these sea level changes from 2019 to 2020 (Fig. 3.16b) are representative of the underlying OHCA changes in these locations (Fig. 3.4b) but also incorporate the sea level response to year-to-year variability of oceanic warming (Widlansky et al. 2020).

Besides development of La Niña and the associated falling sea levels that occurred in the eastern half of the equatorial Pacific during 2020, the largest intra-seasonal changes (Figs. 3.16c,d) occurred in the tropical Indian Ocean. The year began with well above-normal sea levels in the western Indian Ocean and well below-normal sea levels to the east (a gradient of almost 30 cm during the December–February [DJF] season; Fig. 3.16c). By the September–November (SON) season, the zonal gradient of sea level anomalies in the Indian Ocean had mostly disappeared (Fig. 3.16d). This relaxation of the Indian Ocean sea level anomalies was concurrent with the transition of the Indian Ocean dipole (IOD) index from positive at the beginning of 2020 to near neutral for the remainder of the year (see section 4f). The 2020 minus 2019 sea level difference (Fig. 3.16b) in the tropical Indo-Pacific more closely resembles the end-of-year pattern (Fig. 3.16d; SON), compared to the early-year pattern (Fig. 3.16c; DJF), which is consistent with the abrupt termination of the positive IOD.

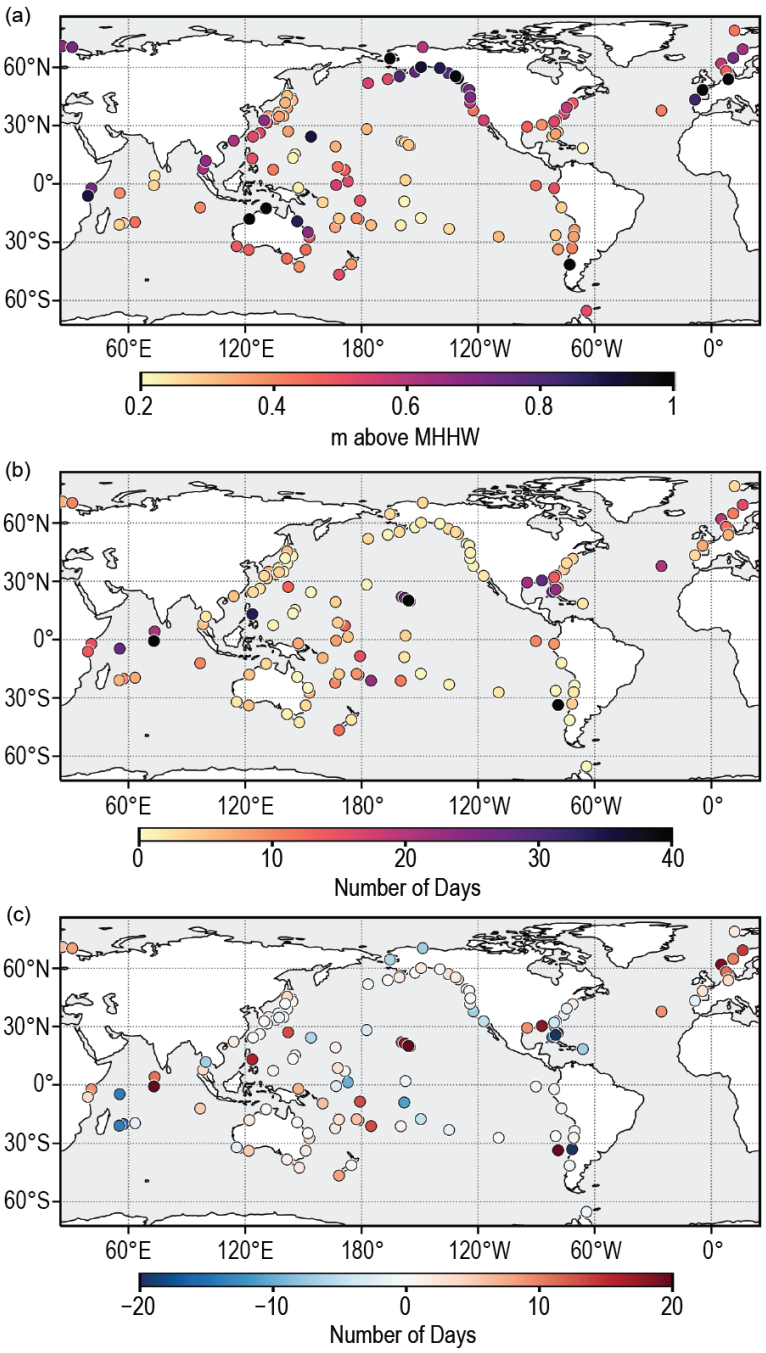

Fig. 3.17. (a) Nuisance-level flooding thresholds defined by the level of the top 1% of observed daily maxima during 2000–18 from tide gauge records. Units are in meters above mean higher high water (MHHW) calculated over 2000–18. (b) Number of daily maximum water levels exceeding the thresholds in (a) during 2020. (c) Same as in (b), but for 2020 minus 2019. Daily maximum water levels were calculated from hourly tide gauge observations obtained from the University of Hawaii Sea Level Center Fast Delivery database. Only records with at least 80% completeness during 2000–18 and 80% completeness during 2020 were analyzed.

Ongoing trends and year-to-year changes in sea level impact coastal communities by increasing the magnitude and frequency of positive sea level extremes that cause flooding and erosion. In many areas, coastal infrastructure is exposed to minor high-tide flooding when water levels exceed a threshold defined by the top 1% of observed daily maxima (Sweet et al. 2014). Such thresholds are expected to be exceeded three to four times per year but the heights of the thresholds vary geographically (Fig. 3.17a). The greatest numbers of 1%-threshold exceedances during 2020 occurred in regions that experienced the highest sea level anomalies (Fig. 3.17b): the equatorial and northern Indian Ocean and coasts along the western Pacific, the Hawaiian Islands, along the Gulf of Mexico, the southeast United States, and northern Europe. The number of threshold exceedances decreased by more than five days from 2019 to 2020 at 17 of the 122 locations analyzed and increased by more than five days at 31 locations (Fig. 3.16c). The largest year-over-year increases occurred in the equatorial Indian Ocean, Hawaii, and northern Europe, while elevated numbers of exceedances in the eastern Gulf of Mexico and southeast United States mostly represented a continuation of (or decrease from) elevated exceedances during 2019.

g. Surface currents—R. Lumpkin, R. Domingues, and G. Goni

This section describes ocean surface current changes, transports derived from ocean surface currents, and features such as rings inferred from surface currents. Surface currents are obtained from in situ (global arrays of drogued drifters and moorings) and satellite (altimetry and wind stress) observations. Transports are derived from a combination of sea surface height anomalies (from altimetry) and hydrographic climatologies. See Lumpkin et al. (2011) for details of these calculations. Zonal surface current anomalies are calculated with respect to a 1993–2007 climatology and are discussed for individual ocean basins as follows.

1) Pacific Ocean

In 2020, the Pacific exhibited basin-wide annual mean zonal westward (negative) current anomalies of 14–16 cm s^{-1} from 150°E to 100°W (Fig. 3.18a) and the equator to 1°N, associated with the 2020 La Niña (see sections 3b, 4b). These were driven by strengthened easterly trade winds (Fig. 3.13a) and produced equatorial upper ocean heat anomalies that were negative in the east and positive in the west (Fig. 3.4a). To the north, eastward anomalies of 5 cm s^{-1} at 150°E–120°W, 8°–10°N indicated a stronger and northward-shifted North Equatorial Countercurrent (NECC; e.g., Johnson et al. 2002), which had a maximum eastward speed of 28 cm s^{-1} (total, not anomaly) at 6.6°N. This northward shift has been seen since 2018, when the NECC was similar in strength to 2020; because it was slightly weaker in 2019, the 2020 minus 2019 anomaly difference (Fig. 3.18b) indicates weaker eastward anomalies along this band.

Eastward anomalies of ~25 cm s^{-1} were present in the western equatorial Pacific in December–February (DJF), but reversed to strong (25 cm s^{-1}) westward anomalies across the basin by March–May (MAM; Fig. 3.19), leading sea surface temperature anomalies (see Fig. 3.2) by a season.

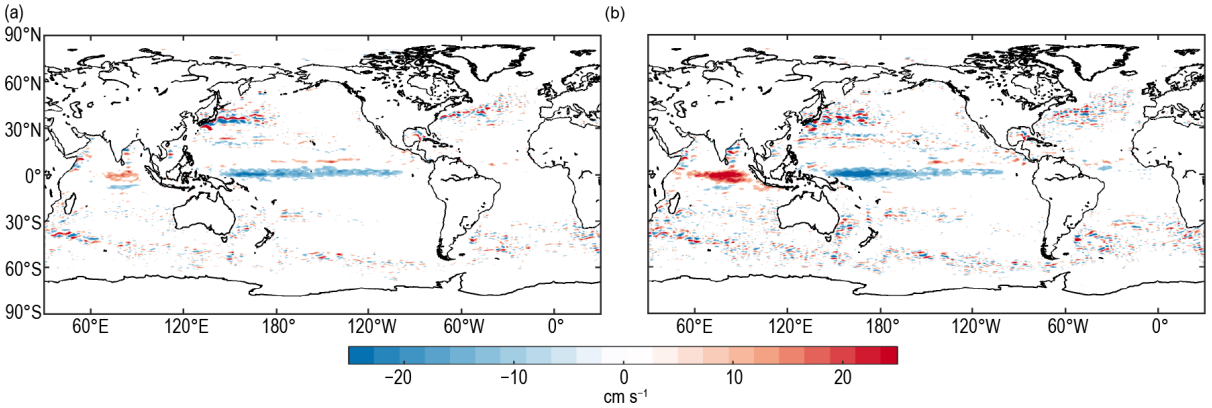

Fig. 3.18. Annually averaged geostrophic zonal current anomalies (cm s^{-1}) for (a) 2020 and (b) 2020 minus 2019 difference derived from a synthesis of drifters, altimetry, and winds. Values not shown where they are not significantly from zero.

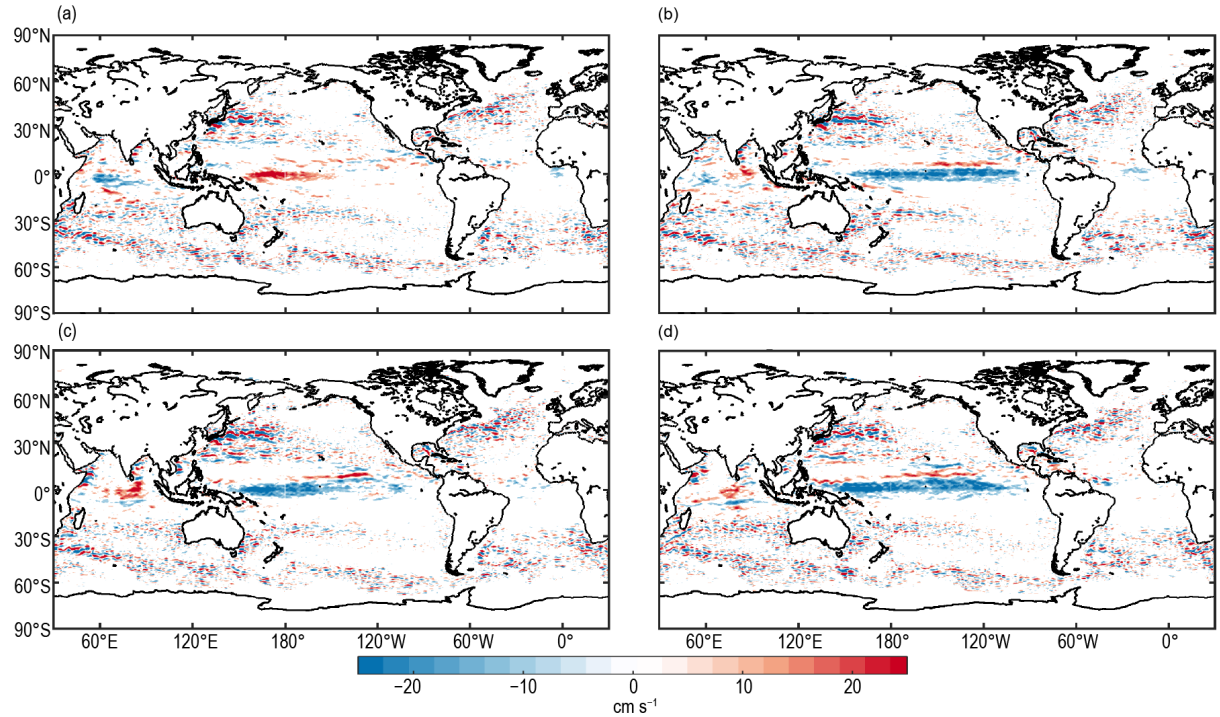

Fig. 3.19. Seasonally averaged zonal geostrophic anomalies (cm s^{-1}) with respect to seasonal climatology, for (a) DJF 2019/20, (b) MAM 2020, (c) JJA 2020, and (d) SON 2020. Values not shown where they are not significantly different from zero.

These zonal surface current anomalies were strongest (25 cm s^{-1}) on the equator but were present from 6°S–4°N. Also in MAM, the NECC accelerated and exhibited eastward anomalies of ~10 cm s^{-1} along 6°–7°N. By June–August (JJA), the equatorial westward anomalies were primarily confined to the western third of the basin, while NECC anomalies weakened except in a narrow longitude range 125°–150°W. During these months, the core of the NECC was shifted north from its climatological location of 6.6°N to 8°N. As the year waned (September–November [SON]), westward anomalies reappeared west of 100°W from 6°N to 5°S, with maxima of ~25 cm s^{-1} on the equator.

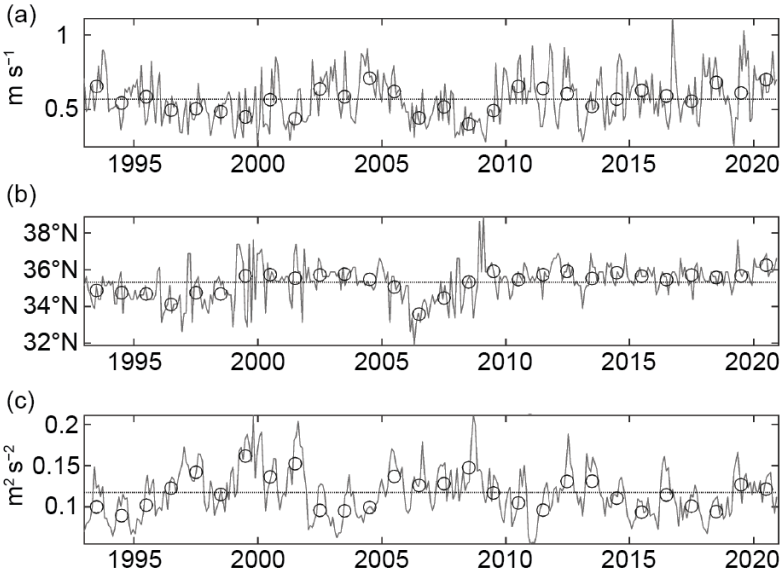

Fig. 3.20. (a) Maximum zonally averaged value of total geostrophic zonal velocity (U; m s^{-1}) versus time in the Kuroshio Extension region (141°–153°E, 32°–38°N; Qiu and Chen 2005). (b) Latitude (°N) of the maximum velocity shown in (a). (c) Eddy kintetic energy (EKE; m^2 s^{-2}) averaged in the Kuroshio Extension region. In all plots, monthly values are shown in gray, annual averages as black circles, and the time-mean is shown as a horizontal gray line.

In 2020, the global anomaly map (Fig. 3.18a) featured strong positive anomalies north of and strong negative anomalies south of the mean Kuroshio Extension location, indicating a shift to the north of 1.3° latitude (from 35.3°N to 36.6°N; Figs. 3.20a,b), the most northern annually-averaged location since 1993 (the start of satellite altimeter records). Long-term shifts in the location of the Kuroshio Extension are associated with a decadal stable/unstable oscillation (Qiu and Chen 2005). The Kuroshio Extension shifts to the north when it intensifies and becomes stable thus lowering eddy kinetic energy (EKE). Averaged in the downstream Kuroshio Extension region (141°–153°E, 32°–38°N; Qiu and Chen 2005), EKE was low in 1993–95, elevated in 1999–2001, low in 2002–04, high in 2005–08, and low in 2015–18 (Fig. 3.20c). EKE was close to its long-term average during 2019 and 2020. As noted in the *State of the Climate in 2019* report, the northern location of the Kuroshio Extension and near-climatological levels of EKE are so far inconsistent with a phase shift of the decadal mode described by Qiu and Chen (2005).

2) Indian Ocean

Annually-averaged zonal currents in the Indian Ocean exhibited 10–20 cm s^{-1} eastward anomalies at 6°S–2°N, 70°–95°E and, in the same longitude range, westward anomalies of 10–15 cm s^{-1} at 8°–14°S (Fig. 3.18a). The eastward anomalies are consistent with strong La Niña conditions and a southward migration of the South Equatorial Current (SEC; Lumpkin and Johnson 2013), while the westward anomalies indicate a strengthening of the SEC in that latitude band. Differences from 2019 (Fig. 3.18b) reflect the strong westward anomalies at 55°–95°E, 2°S–1°N seen in 2019 (and hence are positive anomalies in the 2020 minus 2019 difference map). The 2020 eastward anomalies indicate an acceleration of the seasonally varying eastward Wyrtki Jet, which climatologically is most prominent in May and November (e.g., Nagura and McPhaden 2010). These anomalies developed in JJA after the westward La Niña-related Pacific anomalies were established (Fig. 3.19c), when the Wyrtki Jet typically weakens to a weakly reversed state (Lumpkin and Johnson 2013). They persisted through SON (Fig. 3.19d) consistent with La Niña conditions (Lumpkin and Johnson 2013).

3) Atlantic Ocean

Annual mean zonal currents in the tropical Atlantic Ocean in 2020 exhibited a similar pattern to those in the Pacific, but zonal velocity anomalies were much weaker (Fig. 3.18a). Averaged across the basin, eastward anomalies of 3–4 cm s^{-1} at 6°–7°N indicate a slightly accelerated and northward-shifted NECC, while westward anomalies of 3–5 cm s^{-1} from the equator to 4°N indicate an acceleration of the westward northern core of the SEC. These westward anomalies rapidly developed in March–May (Fig. 3.19b) to maxima of ~10 cm s^{-1}, weakened through JJA (Fig. 3.19c), and were gone by SON (Fig. 3.19d).

The variability of key Atlantic Ocean currents is continuously monitored in near-real time by leveraging relationships between in situ and satellite altimetry observations (https://www.aoml.noaa.gov/phod/indexes/index.php). In the South Atlantic, the Agulhas Current shed five rings, within the 1993–2020 average of four to six rings in a given year. The annual transport of the Agulhas Current was slightly below the average by –1.4 Sv in a cross section at ~28°E and between 34°S and 40°S. In the southwestern Atlantic, the Brazil–Malvinas Confluence was for the fourth consecutive year displaced to the south with respect to its mean location during 1993–2020. Since 1993, the Brazil–Malvinas Confluence has shifted southward at decadal time scales (cf., Lumpkin and Garzoli 2011; Goni et al. 2011). During 2020, the confluence was on average 0.5 degrees of latitude south of its 1993–2019 mean location, and over 1.5 degrees of latitude south of its average location in the early 1990s. This is important because the Brazil Current is the mechanism by which waters of subtropical origin are transported into subpolar regions.

In the North Atlantic, the 2020 volume transports of the North Brazil Current, Yucatan Current, and Florida Current (FC) were all below their 1993–2020 averages. The North Brazil Current serves as an interhemispheric conduit for water masses and heat from the South Atlantic into the North Atlantic. It also often sheds rings (Goni and Johns 2003) that can enter the Caribbean Sea while carrying low-salinity Amazon River waters (Ffield 2007), which are known for creating barrier layer conditions that can often contribute to hurricane intensification (e.g., Balaguru et al. 2012; Domingues et al. 2015). The North Brazil Current exhibited a mean negative transport anomaly of –1.4 Sv in 2020, which is within the lowest 25th percentile in terms of its annual mean transport, with anomalies as low as –5 Sv observed mostly during the first half of 2020. Farther to the north, the Yucatan Current and FC exhibited mean negative anomalies of –0.3 Sv and –0.7 Sv, respectively, with positive anomalies reaching ~2 Sv in the first half of 2020 and negative anomalies as low as –4 Sv during the second half of the year. Interestingly, the negative anomalies observed in the North Brazil Current during the first quarter of 2020 are of similar magnitude to the negative anomalies observed both in the Yucatan Current and FC in the latter half of the year. Because these currents are a critical part of the Atlantic meridional overturning circulation's surface pathway (section 3h), negative transport anomalies first seen in the North Brazil Current may have subsequently propagated westward through the Caribbean Sea, were then transported into the Gulf of Mexico by the Yucatan Current, and then into the Florida Straits by the FC in the latter half of 2020. A lower-than-usual FC transport is closely tied to higher coastal sea level and "sunny day" flooding events along the southeast U.S. coast (Ezer and Atkinson 2014; Domingues et al. 2016; Volkov et al. 2020a) , which may partly explain the 2020 increased number of high-tide flooding days in the Gulf of Mexico and southeast U.S. (Fig. 3.16b). Further studies addressing the delayed North Brazil Current to FC connection may help develop early warnings for such flooding events.

h. Meridional overturning circulation and heat transport in the Atlantic Ocean—D. L. Volkov, S. Dong, M. Lankhorst, M. Kersalé, A. Sanchez-Franks, C. Schmid, J. Herrford, R. C. Perez, B. I. Moat, P. Brandt, C. S. Meinen, M. O. Baringer, E. Frajka-Williams, and D. A. Smeed

The zonally integrated component of surface and deep currents, known as the meridional overturning circulation (MOC), plays an important role in Earth's climate because it provides a mechanism for ocean meridional heat transport (MHT). The observing system for the Atlantic MOC/MHT consists of several basin-wide moored arrays as well as the combination of satellite altimetry and in situ (mainly Argo and eXpendable BathyThermograph [XBT]) measurements (Fig. 3.21a; e.g., Frajka-Williams et al. 2019). The currently active basin-wide moored arrays are the Rapid Climate Change/MOC and Heatflux Array/Western Boundary Time Series (RAPID/MOCHA/WBTS) array at 26.5°N (Moat et al. 2020a), the South Atlantic MOC Basin-wide Array (SAMBA) at 34.5°S (Meinen et al. 2013, 2018), the Overturning in the Subpolar North Atlantic Program (OSNAP) array between about 55° and 60°N (Lozier et al. 2017, 2019), and the Tropical Atlantic Circulation and Overturning array at 11°S (TRACOS; Herrford et al. 2021).

The *State of the Climate in 2019* report included MOC/MHT estimates derived from mooring measurements up to 2018 (Volkov et al. 2020b). The COVID-19 pandemic negatively impacted the servicing of moorings, because most research cruises scheduled in 2020 were either postponed or canceled. Therefore, no updates are available as of this writing for the basin-wide arrays in the North Atlantic (Figs. 3.21b,c). In this report, however, we present novel MOC upper- and lower- ("abyssal") cell transport estimates from the extended number of SAMBA moorings (Fig. 3.21e; Kersalé et al. 2020) and new results for the TRACOS array (Fig. 3.21d; Herrford et al. 2021). Then we discuss the state of the Florida Current (FC) at 27°N (Fig. 3.22a) and provide the new estimates of the North Atlantic Current (NAC) volume transport (Fig. 3.22b; Lankhorst and Send 2020), which

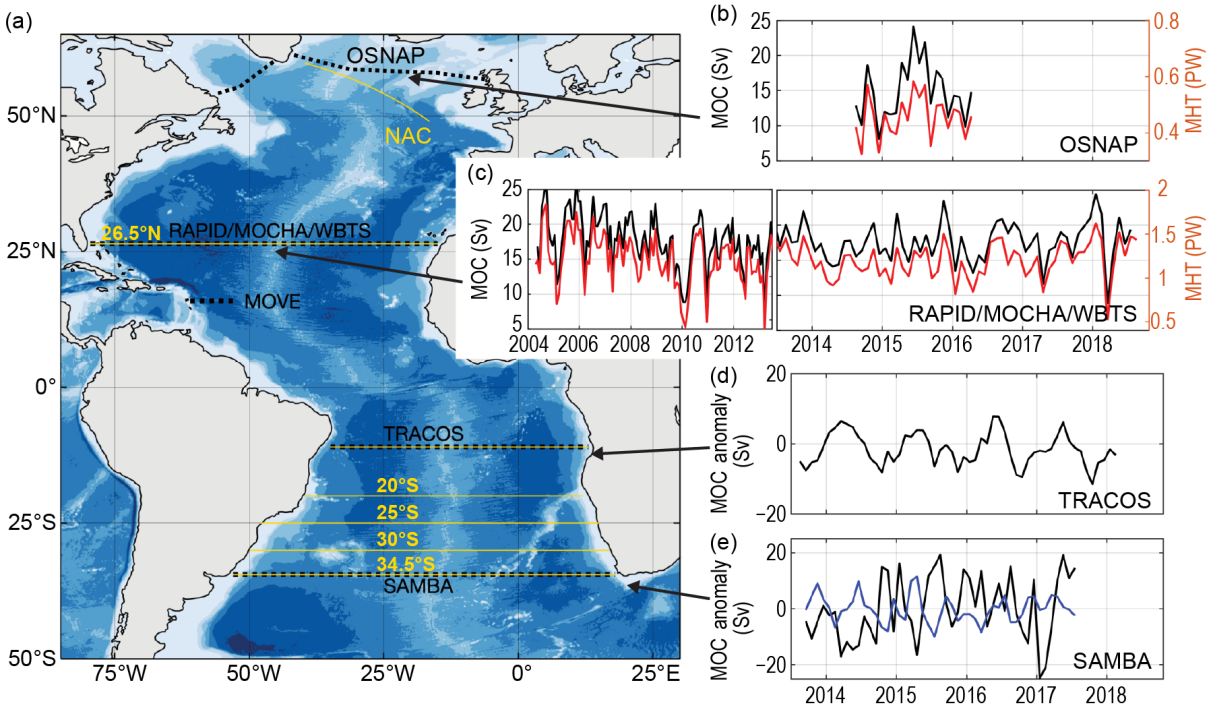

Fig. 3.21. (a) The Atlantic Ocean meridional overturning circulation (MOC) observing system: moored arrays (dashed black lines) and sections (yellow lines) across which the MOC is estimated by combining in situ measurements (Argo, XBT, bottom pressure) with satellite altimetry data. (b) Monthly time series of the MOC northward volume transport (black) and meridional heat transport (MHT; red) across the OSNAP array (Lozier et al. 2019). (c) Monthly time series of the MOC northward volume transport (black) and MHT (red) across the RAPID/MOCHA/WBTS array (Moat et al. 2020b). (d) Monthly time series of the MOC northward volume transport anomaly across the TRACOS array (Herrford et al. 2021). (e) Monthly time series of the MOC northward upper (black) and abyssal cell (blue) volume transport anomalies across the SAMBA (Kersalé et al. 2020). Units for (b)–(e) are given in Sv.

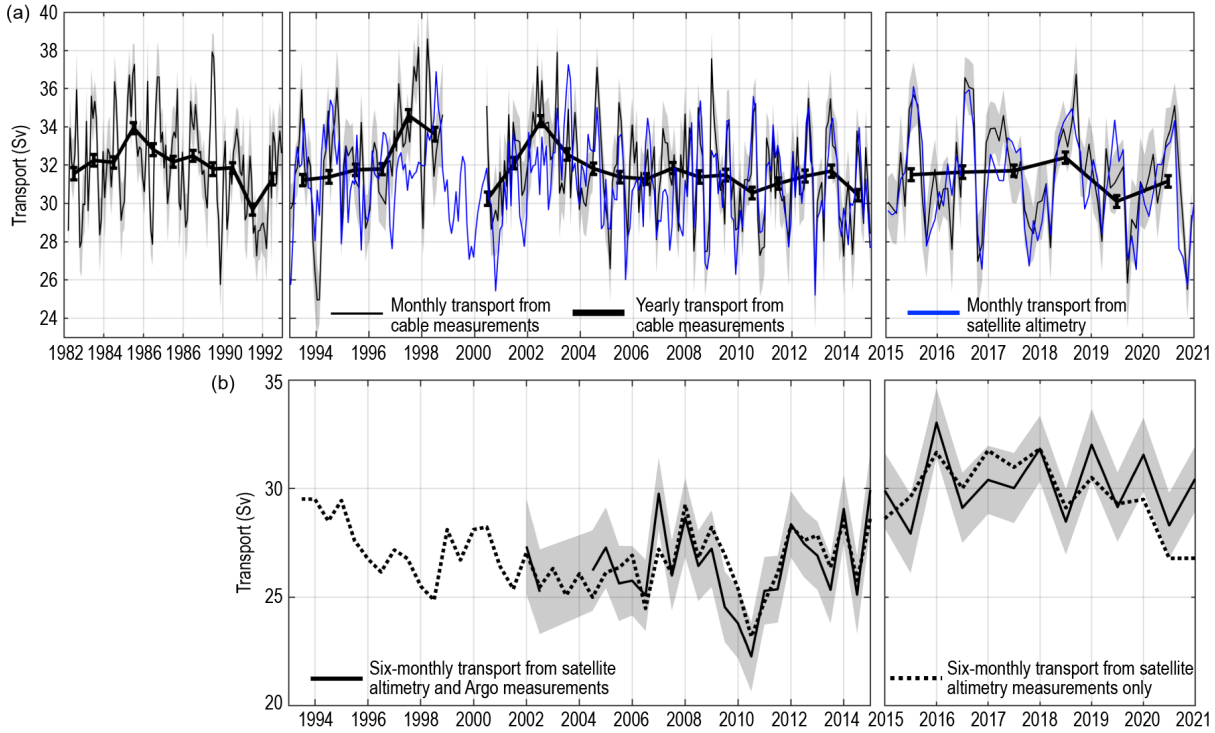

Fig. 3.22. (a) Monthly (thin black curve) and yearly (thick black curve) averages of the Florida Current (FC) volume transport (Sv) derived from the cable measurements at 27°N with associated uncertainties (gray shading and black error bars, respectively). Uncertainties include the measurement error and the standard error of the mean. Monthly averaged FC volume transport (Sv) derived from satellite altimetry (blue) following Volkov et al. (2020b). (b) Six-monthly North Atlantic Current (NAC) volume transport across the NAC section (see Fig. 3.21a for location) following Lankhorst and Send (2020): transport derived from satellite altimetry and Argo measurements (solid curve) with uncertainties (gray shading) and transport derived from satellite altimetry measurements only (dotted curve).

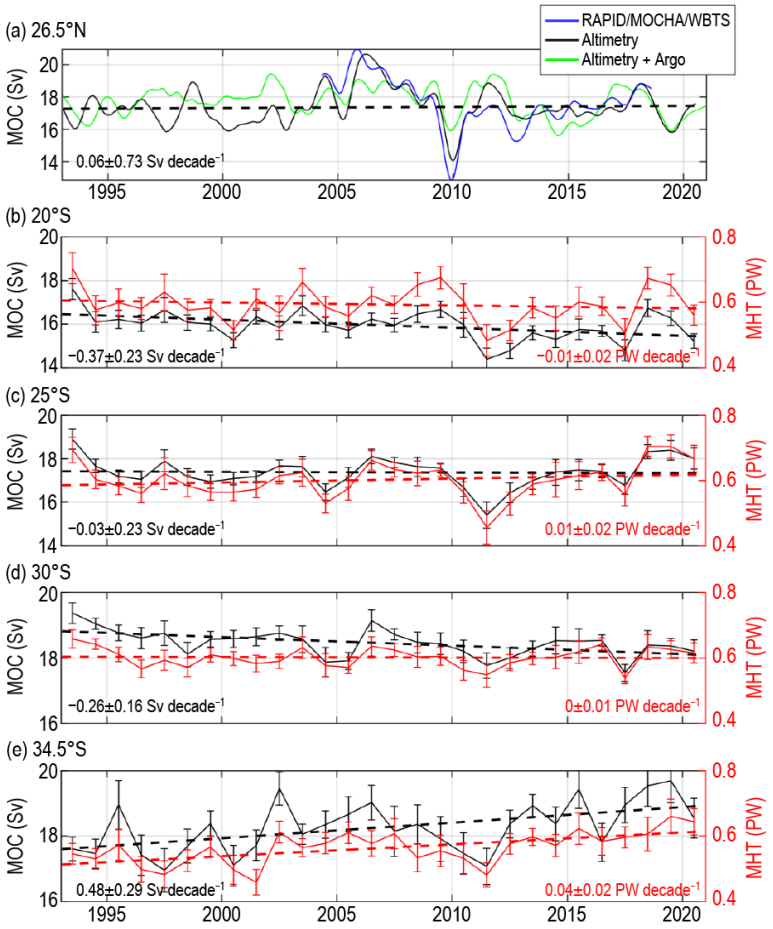

Fig. 3.23. Blended meridional overturning circulation (MOC) estimates (Sv) based on combinations of satellite altimetry and in situ hydrography data. (a) The MOC at 26.5°N derived from RAPID/MOCHA/WBTS observing array (blue), satellite altimetry (black), and satellite altimetry and Argo (green). (b–e) The yearly MOC Sv; (black) and meridional heat transport (MHT) (PW, red) averages at various latitudes in the South Atlantic. Error bars in (b)–(e) show standard errors of the yearly means. Dashed lines show linear trends over the observational period.

both constitute the bulk of the upper limb northward MOC transport in the subtropical and subpolar North Atlantic, respectively. Finally, we present updated MOC/MHT estimates derived from blended in situ and satellite observations at different locations through 2020 (Fig. 3.23).

The Atlantic MOC consists of an upper cell and an abyssal cell. Preliminary SAMBA efforts focused solely on the upper cell using two pressure-equipped inverted echo sounder (PIES) moorings at 1350-dbar isobath on either side of the basin (Meinen et al. 2013, 2018). Recently,

both the upper and abyssal cell volume transports at 35.5°S from September 2013 to July 2017 were obtained using nine PIES (Fig. 3.21e; Kersalé et al. 2020). Both the upper and abyssal cells exhibit a high degree of variability at time scales ranging from a few days to a few weeks. The upper-cell transport variability obtained from nine PIES is about twice as strong as the variability observed with only two PIES (std. devs. are 15.5 and 8.2 Sv, respectively), due to a better representation of barotropic flows and mesoscale eddies. The rather low (−0.4) correlation between the upper and abyssal cell daily transports suggests that transport variability in the abyssal cell is largely independent of the variations in the upper cell. Both cells exhibit positive, but statistically insignificant, transport trends.

TRACOS array data at 11°S were analyzed in Herrford et al. (2021). This array consists of a western boundary current transport array (Hummels et al. 2015), an eastern boundary current meter mooring (Kopte et al. 2017), and two sets of pressure gauges deployed at 300-m and 500-m depth across the Brazilian continental slope and at the eastern boundary off Angola. The MOC transport estimate is based on the combination of bottom pressure measurements with satellite altimetry and wind stress data, and covers 2013–18 (Fig. 3.21d). Given the limitations of instruments and the shortness of time series, only the seasonal variability of the MOC at 11°S was investigated. The seasonal peak-to-peak amplitude of the MOC transport is 14 Sv, which is contributed by the upper-ocean geostrophic and Ekman transport fluctuations with peak-to-peak amplitudes of 12 Sv and 7 Sv, respectively. The seasonal variability of the geostrophic contribution to the MOC at 11°S is mainly modulated by oceanic adjustment to local and remote wind forcing.

The oldest MOC trans-basin array at 26.5°N (RAPID/MOCHA/WBTS) consists of tall moorings between the Bahamas and Africa and measurements of the FC volume transport with a submarine cable. Although the COVID-19 pandemic made it impossible to retrieve the mooring data and update the MOC estimates in 2020, cable measurements of the FC (Fig. 3.22a) were not affected. In 2020, the annual mean FC transport (31.2 ± 0.3 Sv) was stronger than in 2019 (30.1 ± 0.3 Sv), and close to the record mean transport (31.8 ± 0.2 Sv). The FC transport has been rather stable over the entire observational record, exhibiting only a small, statistically insignificant, negative trend (−0.03 ± 0.03 Sv yr^{-1}). Given the extremely high value of the FC measurements for monitoring the Atlantic MOC at 26.5°N, backup observing systems have been investigated in case the cable someday becomes inoperable. Transports estimated from bottom pressure measurements (8 July 2008–17 September 2014) on both sides of the Straits of Florida at 27°N explain roughly 55% of the daily cable transport variability (Meinen et al. 2020). Similarly, FC transports derived from cross-stream sea level differences measured by satellite altimetry (blue curve in Fig. 3.22a) account for up to 60% of the cable transport subsampled at the days of satellite overpasses (Volkov et al. 2020a). Although pressure gauges provide unrivaled temporal resolution, satellite altimetry yields a longer homogeneous data record (back to 1993) filling in the existing gaps in cable data (e.g., 1998–2000).

While no updates are available for the OSNAP array in the subpolar North Atlantic since the past year's report (Fig. 3.21b), an estimate of the NAC volume transport across a section between the central Irminger Sea and the Porcupine Abyssal Plain (NAC section in Fig. 3.21a) was computed from in situ density profiles and satellite altimetry sea level anomalies (Lankhorst and Send 2020). Similar to the FC in the subtropical gyre, the NAC is an important contributor to the upper-ocean MOC transport in the subpolar gyre. The six-monthly NAC transport estimates (Fig. 3.22b) suggest that there is a likely multi-decadal oscillation exhibiting high values in the early 1990s, lower values throughout the 2000s, and higher transports again in recent years (2015–20). Values in recent years are below the recent maximum and may indicate the beginning of a downward tendency.

The only basin-integrated transports that were updated through 2020 are the blended estimates derived from the combination of satellite altimetry and in situ hydrography (XBT, Argo, etc.; Sanchez-Franks et al. 2021; McCarthy et al. 2020; Majumder et al. 2016; Dong et al. 2015). An MOC time series at 26.5°N, generated from the combination of altimetry and Argo data using the

method of Majumder et al. (2016), has been updated through 2020 (McCarthy et al. 2020; green curve in Fig. 3.23a). Another dynamically based method was recently developed for estimating the MOC at 26.5°N using satellite altimetry, in situ density profiles, and the ERA5 zonal wind stress (Sanchez-Franks et al. 2021). This latter MOC estimate (black curve in Fig. 3.23a) captures 69% of the interannual MOC variability observed by the RAPID/MOCHA/WBTS array (blue curve in Fig. 3.23a). The two satellite-based estimates reasonably agree only after the advent of Argo data in 2004, which indicates sensitivity to the amount of in situ data available for calibration and methodology used to derive them. Both estimates suggest that the MOC in 2020 was 1–2 Sv stronger than in 2019, but weaker than in 2018. It is too early to draw conclusions about the longer MOC tendencies, in particular in relation to a possible MOC strengthening since 2010 reported in Moat et al. (2020a).

Yearly blended MOC/MHT estimates at 20°S, 25°S, 30°S, and 34.5°S (Figs. 3.23b–e) obtained following Dong et al. (2015) estimate that in 2020, the MOC and MHT were somewhat lower than in 2019 at all latitudes. However, this change was statistically significant only at 34.5°S and 20°S for the MOC and at 20°S for the MHT. Significant positive trends in both the MOC and MHT over the entire observational period are observed at 34.5°S (0.48 ± 0.29 Sv decade^{-1} and 0.04 ± 0.02 PW decade^{-1}, respectively). Significant negative trends in the MOC are observed at 30°S (−0.26 ± 0.16 Sv decade^{-1}) and 20°S (−0.37 ± 0.23 Sv decade^{-1}), with no significant trends in the MHT at other latitudes. These trends suggest that there has been a strengthening of the South Atlantic subtropical gyre and associated heat convergence in 1993–2020, consistent with the warming trend observed in the region (e.g., Dong et al. 2020; Fasullo and Gent 2017; Fig. 3.4c).

Comparisons of the various blended satellite/in situ MOC estimates among each other and the results from moored arrays (at 26.5°N and 34.5°S) usually yield low correlations and different variances (not shown), suggesting that the estimates are sensitive to the methodology used to derive them. In addition, differences between the MOC estimates from the pilot (two PIES) and extended (nine PIES) SAMBA moorings suggest sensitivity to the design of the observing array. To better determine the state of the MOC and understand its variability, it is necessary to reconcile different estimates and investigate the sources of uncertainties.

i. Global ocean phytoplankton—B. A. Franz, I. Cetinić, J.P. Scott, D. A. Siegel, and T.K. Westberry

Photosynthetic production of carbon by marine phytoplankton fuels oceanic ecosystems and drives biogeochemical cycles (e.g., Falkowski et al. 1998; Field et al. 1998), contributing roughly 50% of global net primary production (NPP). Phytoplankton distribution, growth, and diversity are governed by the availability of light and nutrients (e.g., nitrogen, phosphorous, and iron) in the upper ocean euphotic zone, which in turn are influenced by physical factors such as ocean temperature and circulation processes (e.g., Behrenfeld et al. 2006). Satellite ocean color sensors such as Sea-viewing Wide Field-of-view-Sensor (SeaWiFS; McClain 2009) and Moderate Resolution Imaging Spectroradiometer (MODIS; Esaias et al. 1998) allow detection of spatial and temporal changes in the distribution of phytoplankton through measurements of near-surface concentrations of the phytoplankton pigment chlorophyll-*a* (Chl*a*; mg m^{-3}) or phytoplankton carbon (C_{phy}, mg m^{-3}). While C_{phy} is a direct measure of phytoplankton biomass, Chl*a* is an indicator of variability in both biomass and phytoplankton physiology. Discrepancies between their distributions (shifts in Chl*a*:C_{phy} ratios) thus provide valuable insight into physiological variability within the cells (due to the changes in light and nutrient conditions) or variability in species composition (Westberry et al. 2016; Siegel et al. 2013; Dierssen 2010; Geider et al. 1997). Taken together, these measurements provide a synoptic view of phytoplankton biomass, composition, and health in the ocean, as well as its response to climate-driven changes in the marine environment.

Here we evaluate global Chl*a* and C_{phy} distributions for the one-year period from October 2019 through September 2020 (the analysis year), within the context of the continuous 23-year record provided through the combined observations of SeaWiFS (1997–2010) and MODIS on *Aqua*

(MODIS-A, 2002–present). The MODIS-A daytime sea surface temperature (SST; °C) is also assessed for the same time period to provide context on the physical state of the oceans. The Chl*a* product was derived using the Ocean Color Index algorithm of Hu et al. (2012), while C_{phy} was derived from the particle backscattering coefficient, b_{bp}, at 443 nm (Generalized Inherent Optical Properties algorithm; Werdell et al. 2013) and a linear relationship between b_{bp} and C_{phy} as described in Graff et al. (2015). In combining the ocean color records, the overlapping period from 2003 through 2010 was used to assess and correct for residual bias between the two mission datasets.

Changes in phytoplankton distribution were evaluated by subtracting monthly climatological means for MODIS-A (October 2002–September 2019) from their monthly mean values for MODIS-A Chl*a* and C_{phy} in the analysis year. These monthly anomalies were then averaged to produce the global Chl*a* and C_{phy} annual mean anomaly maps (Figs. 3.24a,b). Similar calculations were performed on MODIS-A SST data to produce an equivalent SST annual mean anomaly for the same time period (Fig. 3.24c). The permanently stratified ocean (PSO) is defined as the region, spanning the tropical and subtropical oceans, where annual average SST is greater than 15°C and surface mixed layers are typically low in nutrients and shallower than the nutricline (black lines near 40°N and 40°S in Fig. 3.24; Behrenfeld et al. 2006).

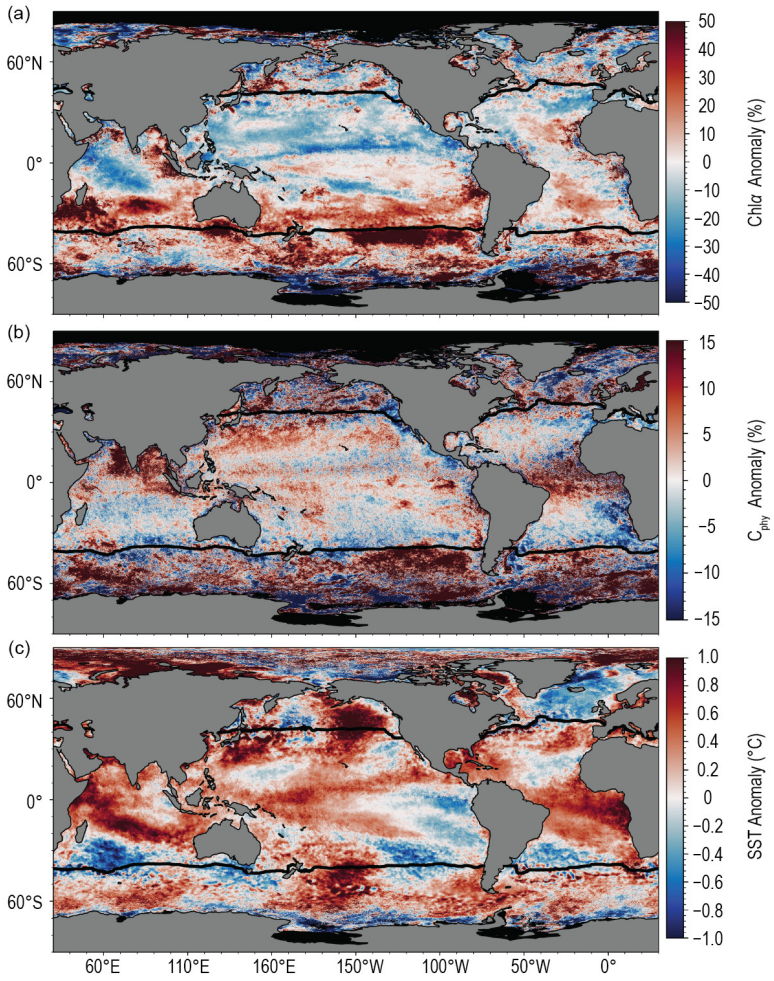

Fig. 3.24. Spatial distribution of average monthly (a) MODIS-A Chl*a* anomalies, (b) MODIS-A C_{phy} anomalies, and (c) MODIS-A SST anomalies, where monthly differences were derived relative to a MODIS-A 17-year climatological record (Oct 2002–Sep 2019). Chl*a* and C_{phy} are stated as % difference from climatology, while SST is shown as an absolute difference. Also shown in each panel is the location of the mean 15°C SST isotherm (black lines) delineating the permanently stratified ocean (PSO). Differences in the SST anomalies here versus in Fig. 3.1a are owing to differences in climatological periods, smoothing, and data sources.

A striking feature of the phytoplankton Chl*a* anomaly distributions for this year is a strong hemispherical difference, with elevated concentrations in the south and depressed concentrations in the north, and with C_{phy} distributions showing a weaker but inverse hemispherical difference (Figs. 3.24a,b). Within the PSO, Chl*a* concentrations (Fig. 3.24a) were consistently elevated 20%–40% throughout much of the subtropical Southern Hemisphere (SH), with the largest positive anomalies in the southern Indian Ocean followed by the subtropical South Pacific and South Atlantic. These regions were generally characterized by anomalously cold water conditions, characteristic of the La Niña phase of the El Niño-Southern Oscillation ([ENSO] with SST depressed −0.6° to −0.8°C; Fig. 3.24c). Negative SST anomalies in these stratified ocean regions typically correspond with a deepening of the surface mixed layer (Deser et al. 2010), which decreases the effective light exposure per unit of phytoplankton biomass within that mixed layer. The response of the phytoplankton to this decreased insolation is to increase cellular chlorophyll concentration and thus light-use efficiency (Behrenfeld et al. 2015). In combination with the physiological response to low-nutrient conditions in the PSO, this leads to increased cellular chlorophyll-to-carbon ratios (Westberry et al. 2016) and thus a decoupling of the Chl*a* and C_{phy} anomalies. The C_{phy}

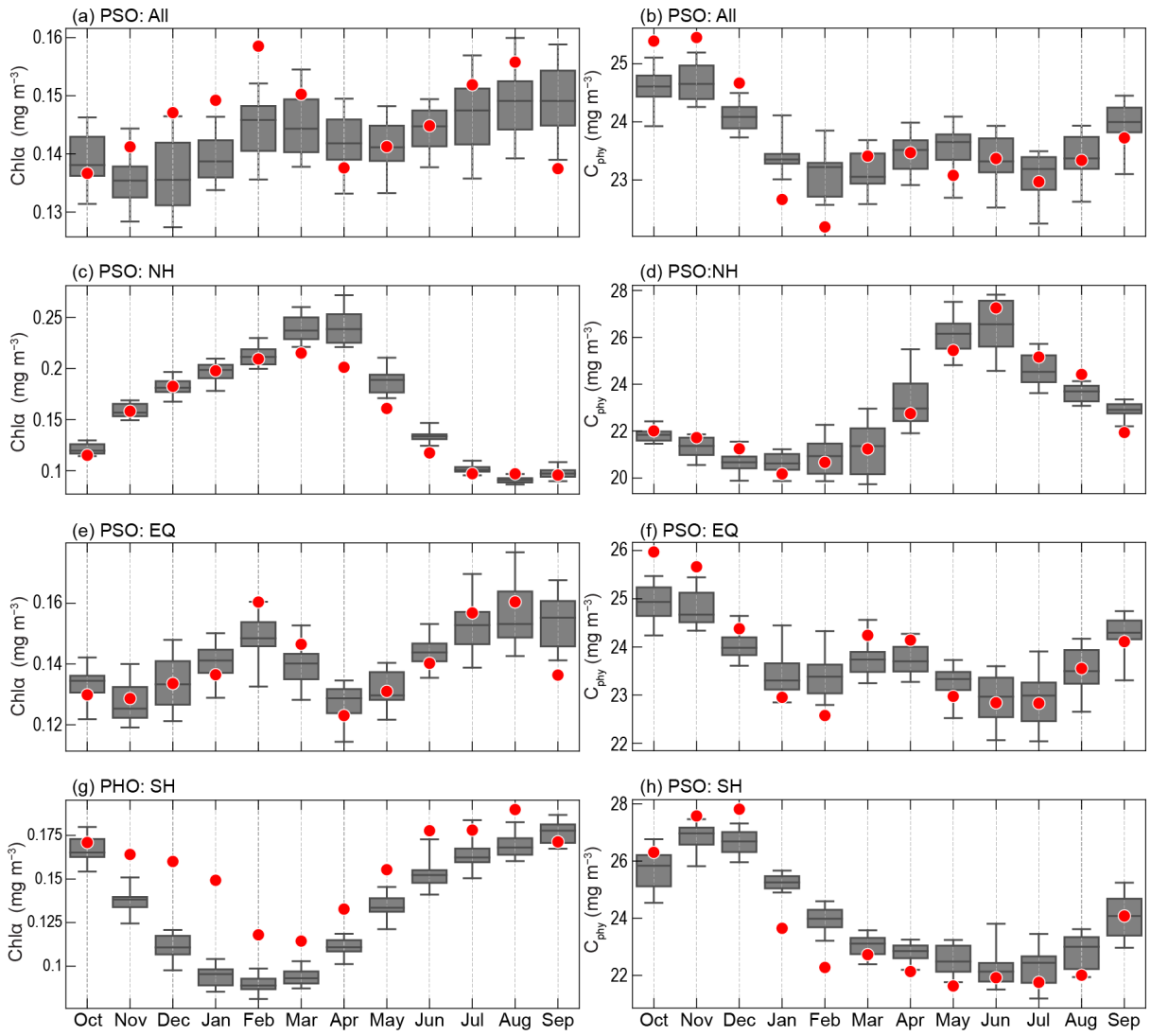

Fig. 3.25. Distribution of Oct 2019–Sep 2020 monthly means (red circles) for (a) MODIS-A Chl*a* and (b) MODIS-A C_{phy} for the PSO region, superimposed on the climatological values as derived from the combined time series of SeaWiFS and MODIS-A over the 22-year period 1998–2019. Gray boxes show the interquartile range of the climatology, with a black line for the median value and whiskers extending to the 5th and 95th percentiles. Subsequent panels show latitudinally segregated subsets of the PSO for the (c),(d), Northern Hemisphere, (e),(f), tropical ±23.5° latitude subregion, EQ, and (g),(h), Southern Hemisphere.

anomalies (Fig. 3.24b) show a reduction in phytoplankton biomass of 5%–10% in these elevated Chl*a* (Fig. 3.24a) regions of the subtropical southern PSO, supporting this hypothesis. A weaker but opposite change in Chl*a* and C_{phy} is observed in the subtropical North Pacific PSO region, with Chl*a* generally depressed (0%–10%) and C_{phy} concentrations neutral to elevated (0%–5%) within anomalously warmer ocean waters (Fig. 3.24c; Sidebar 3.1). Large increases in C_{phy} were also observed in the Arabian Sea and Bay of Bengal, as well as the tropical Atlantic. In the tropical Pacific, both Chl*a* and C_{phy} were weakly elevated, consistent with a transition to La Niña conditions. Outside the PSO, phytoplankton anomalies (Figs. 3.24a,b) showed larger spatial variability and patchiness, including some large patches of highly elevated (>50%) phytoplankton biomass anomalies in the Southern Ocean, but with Chl*a* and C_{phy} generally covarying in these well-mixed waters, consistent with previous studies (e.g., Franz et al. 2020). The higher spatial variability typically observed poleward of the PSO is indicative of the episodic and intense nature of phytoplankton blooms in these regions, but the relatively poor sampling at high latitudes due to clouds and polar night also contributes to higher noise in the ocean color signal, thus limiting confidence in the interpretation of interannual changes.

Seasonal changes in phytoplankton biomass in the PSO typically display two pronounced peaks, reflecting vernal increases in biomass in the Northern Hemisphere (NH) and SH (Fig. 3.25). Peaks in monthly climatological C_{phy} tend to lag peaks in Chl*a* by roughly two to three months, reflecting a reduction in phytoplankton chlorophyll-to-carbon ratios as the seasonal bloom progresses (e.g., Westberry et al. 2016). During 2020, the NH peak in Chl*a* (Fig. 3.25c) occurred in March, followed by C_{phy} maximum in June (Fig. 3.25d), consistent with previous observations (Franz et al. 2020). Generally, monthly mean values of Chl*a* and C_{phy} fell within the range of climatological norms, with the exception of depressed Chl*a* concentrations observed during March–June. In the SH, however, Chl*a* concentrations were well above the climatological norms for much of the analysis period, with a delayed transition from the austral spring peak in October (2019) to the autumn minimum in March, while a weaker but inverse deviation from the climatology was observed in the C_{phy} seasonal cycle. These SH seasonal trend deviations from the climatology are consistent with the

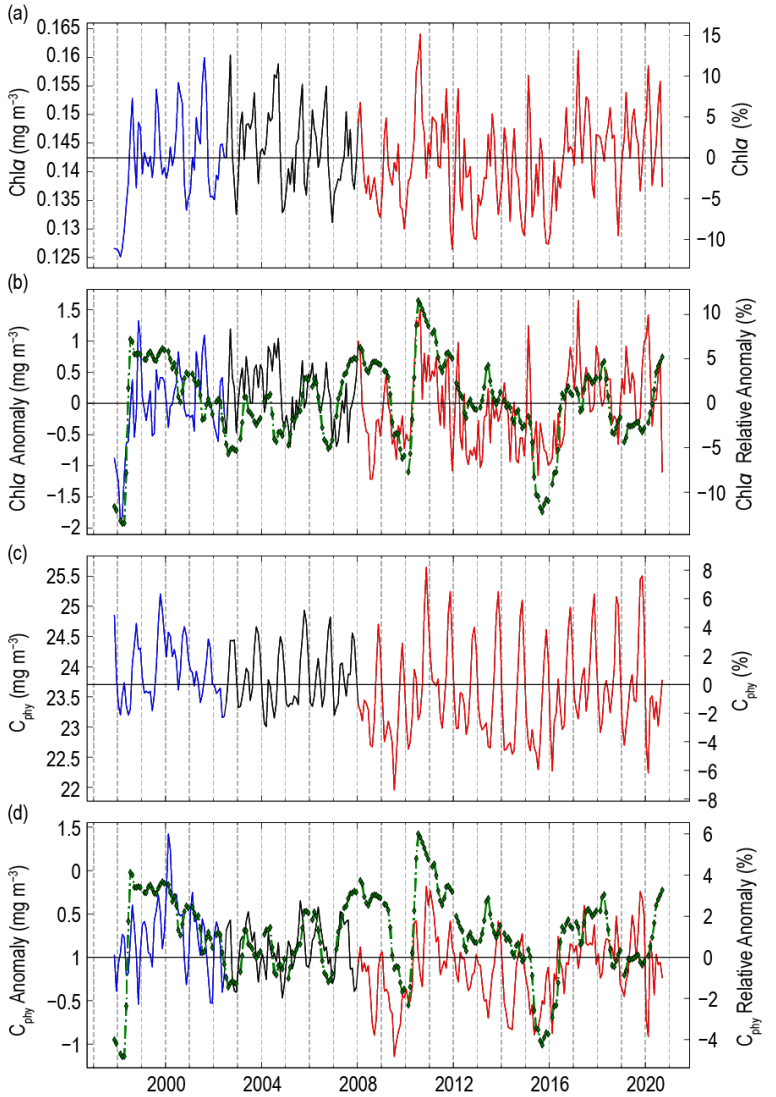

Fig. 3.26. 23-year, multi-mission record of Chl*a* (mg m^{-3}) and C_{phy} (%) averaged over the PSO for SeaWiFS (blue), MODIS-A (red), and combined (black). (a) Chl*a* from each mission, with the horizontal line indicating the multi-mission mean Chl*a* concentration for the region. (b) Monthly Chl*a* anomalies from SeaWiFS and MODIS-A after subtraction of the 22-year multi-mission climatological mean (Fig. 3.25). (c),(d) Same as (a),(b), respectively, but for C_{phy}. Green diamonds show the Multivariate ENSO Index, inverted and scaled to match the range of the Chl*a* and C_{phy} anomalies.

mean anomalies observed in Fig. 3.24, and provide additional context for the progression of the anomaly through the year.

Over the 23-year time series of spatially integrated monthly mean Chl*a* within the PSO (Fig. 3.26a), concentrations vary by ~15% (±0.02 mg m^{-3}) around a long-term average of 0.142 mg m^{-3} (Fig. 3.26a). This variability includes significant seasonal cycles in Chl*a* distributions and responses to climatic events, as has been observed previously (e.g., Behrenfeld et al. 2006; Franz et al. 2020). C_{phy} over the same 23-year period varies by ~7% (±1.5 mg m^{-3}) around an average of 23.7 mg m^{-3} (Fig. 3.26c). Seasonal cycles in C_{phy} are more clearly defined than those of Chl*a*, consistent with the assertion that C_{phy} better represents variability of phytoplankton biomass, independent of the confounding influence of physiology.

Chl*a* monthly anomalies within the PSO (Fig. 3.26b) vary by ±10% (±0.015 mg m^{-3}) over the multi-mission time series, with the largest deviations generally associated with ENSO events, as demonstrated by the correspondence of Chl*a* anomaly variations with the Multivariate ENSO Index (MEI; Wolter and Timlin 1998; presented in the inverse to illustrate the covariation). Pearson correlation coefficients between MEI and the Chl*a* and C_{phy} monthly anomalies calculated for the 23-year record were 0.36 and 0.30, respectively. Over the last year, variability in monthly Chl*a* anomalies was modest (–2% to +10%) and generally elevated, consistent with weak La Niña conditions (Fig. 3.26b). Similar observations cannot be made of the C_{phy} anomalies, which were more constrained than the Chl*a* anomalies and generally do not follow the MEI over the last year (Fig. 3.26d). Our findings suggest that the effect of the 2020 La Niña on phytoplankton populations within the PSO was generally to increase Chl*a*:C_{phy} ratios while leaving phytoplankton biomass largely unchanged.

Observed trends and variability in C_{phy} reflect changes in phytoplankton biomass, while Chl*a* variability can indicate changes in biomass, physiology, and community composition (e.g., Dierssen 2010). These properties are mechanistically linked to physical conditions of the upper ocean, as well as to ecological interactions between phytoplankton and their zooplankton predators. Our ability to track subtle variations in the distribution of Chl*a* and C_{phy} on the global scale can help unravel the diversity and covariation of climate-driven changes in phytoplankton distributions. Future satellite missions, such as the upcoming hyperspectral Plankton, Aerosol, Cloud, ocean Ecosystem (PACE) mission, will enable a more precise identification of phytoplankton absorption features (Werdell et al. 2019) and separation of those features from non-algal optical contributions (Siegel et al. 2005), and thereby facilitate the assessment of changes in phytoplankton species or community composition. Such data will further advance our ability to disentangle the impacts of climate forcing on global phytoplankton communities that drive biogeochemical processes, govern the role of the oceans in the global carbon cycle, and through their productivity exert a controlling influence on marine ecosystems, food webs, and fisheries.

Sidebar 3.2: **Ocean acidification status in Pacific Ocean surface seawater in 2020**—S. R. ALIN, A. U. COLLINS, B. R. CARTER, AND R. A. FEELY

While the Pacific Ocean north of ~20°S has the lowest column inventory of anthropogenic carbon dioxide (CO_2) outside of the Southern Ocean (Gruber et al. 2019), background dissolved inorganic carbon content is high as a result of respiration that occurs in the ocean's interior and old "ages" of deep Pacific waters. Consequently, the northern Pacific Ocean, where deep water resurfaces, has naturally steep vertical gradients in buffering capacity (Egleston et al. 2010; Jiang et al. 2019), CO_2 fugacity (fCO_2; see section 3j), pH—a measure of acidity (Jiang et al. 2019), and calcium carbonate saturation states (Jiang et al. 2015) with many Pacific marine ecosystems vulnerable to ocean acidification impacts (Christian and Ono 2019). In combination with projected deoxygenation, sea surface temperature (SST) change, and a recent propensity for strong, lasting, large-scale marine heatwaves (Bopp et al. 2013; Sidebar 3.1), ocean acidification in the northern Pacific Ocean poses an accelerating threat to marine species and ecosystems that underpin economically important industries from fishing to tourism.

Underway CO_2 observations collected by M/V *Bluefin* provide a synoptic look at carbonate chemistry and pH status in surface waters of the Pacific Ocean north of 15°S during 2020 (Alin et al. 2021). Here we combined the underway fCO_2, temperature, and salinity measurements with total alkalinity estimates generated using the locally interpolated alkalinity regression (LIARv2) method to calculate pH on the total scale (pH_{total}) using CO_2SYS (Carter et al. 2018; van Heuven et al. 2011), creating a 2020 snapshot of ocean acidification status in Pacific surface waters (Fig. SB3.2b). We compared calculated values with published climatological average fCO_2 and pH_{total} values to 2020 observations to determine how 2020 acidification conditions around the Pacific compared to climatological conditions and variability typical of each region.

Because it is an upwelling system, the California Current System (CCS) has high spatial variability in biogeochemical parameters. The Strait of Juan de Fuca (SJDF) is a major source of freshwater to the northern CCS. Winter, spring, and autumn 2020 observations in CCS and SJDF regions revealed average surface fCO_2 values in the CCS below atmospheric values, with relatively high variability, and SJDF fCO_2 averages and variability both higher than in the CCS due to strong mixing of the water column (Feely et al. 2010). Average winter SJDF fCO_2 and pH_{total} values were higher and lower, respectively, than climatological averages but just within seasonal amplitudes for the region; spring observations agreed with climatological averages for both parameters; and autumn average values were substantially

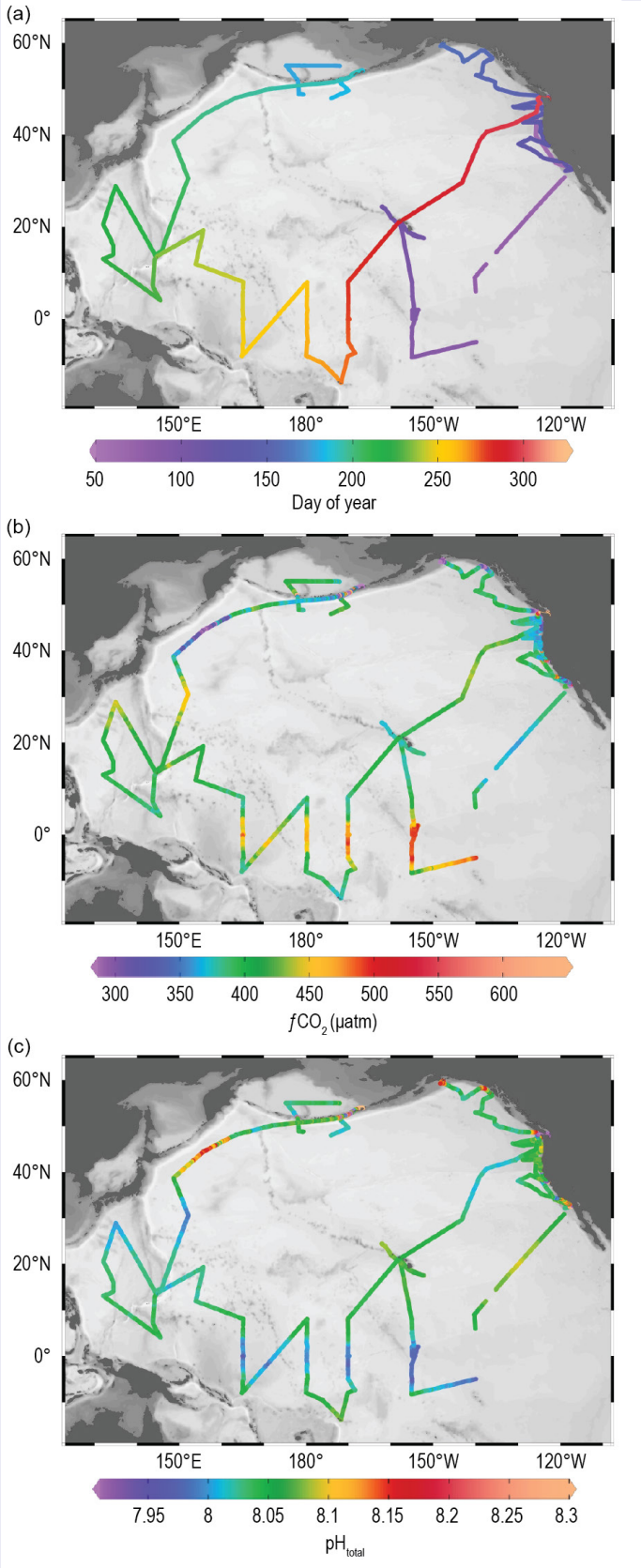

Fig. SB3.2. Pacific Ocean maps for 2020 of (a) day of year, (b) CO_2 fugacity (fCO_2, µatm), and (c) pH_{total}.

higher for fCO_2 and lower for pH_{total} than monthly averages (Fassbender et al. 2018). Seasonal CCS observations for fCO_2 and pH_{total} variability fell within historical bounds as calculated by Fassbender et al. (2018) and Sutton et al. (2019). Most of the highest highs and lowest lows in this 2020 dataset occurred in the CCS or SJDF.

In the subarctic waters (>48°N) of the Gulf of Alaska and south of the Aleutian Archipelago (to 165°E), summer 2020 observations showed moderate to high variability in carbonate chemistry, with average fCO_2 values below atmospheric levels and average pH_{total} values >8.0. Outside of the CCS and SJDF, the lowest and highest fCO_2 and pH_{total} values were recorded near the Aleutians, which reflect strong physical mixing of the water column and resulting biological productivity as water masses pass from the North Pacific into the Bering Sea. Regional average values of fCO_2 and pH_{total} were on the high and low ends, respectively, of published climatological values for summer (Takahashi et al. 2014; Jiang et al. 2019; Sutton et al. 2019).

During mid-summer, the Oyashio Current was a region of strong undersaturation of CO_2 relative to the atmosphere, with the lowest average fCO_2 and highest average pH_{total} values during this synoptic 2020 survey. However, these values were relatively high for fCO_2 and low for pH_{total} compared to climatological values for this region, which is known for strong primary production (Jiang et al. 2019; Midorikawa et al. 2010; Ono et al. 2019), suggesting that the positive 2020 SST anomalies of the northwestern Pacific (cf. Figs. 3.2 and SB3.1) may have resulted in either earlier phytoplankton bloom timing than normal and/or an increase of fCO_2 driven by thermodynamics. The reduced drawdown during these mid-summer observations is consistent with the slightly reduced air–sea CO_2 flux anomaly for 2020 relative to 2019 in this region (cf. Fig. 3.28b).

In the western tropical–subtropical Pacific, relatively low variability in fCO_2 and pH_{total} values were typical of the region, with average values above and below annual climatological values, respectively (Jiang et al. 2019). However, on central equatorial Pacific transects (10°S–10°N, 165°E–140°W), steep meridional gradients in surface carbonate chemistry due to equatorial upwelling resulted in moderately high variability in both fCO_2 and pH_{total}. Peak fCO_2 and minimum pH_{total} were centered near or just south of the equator on each transect. The equatorial upwelling of high-CO_2, low-pH water during La Niña conditions that developed late in 2020 extended farther westward than normal (see section 4b).

In the oligotrophic subtropical North Pacific Gyre (NPG), the lowest fCO_2 and pH variability was recorded during all 2020 cruises. Waters surrounding Hawaii (10°–30°N) and in the northeastern subtropical to temperate Pacific had fCO_2 cruise averages mostly below or near atmospheric values, and pH_{total} averages >8.0. While spring NPG fCO_2 and pH_{total} were within range of climatological values, autumn values of fCO_2 and pH_{total} were somewhat elevated and depressed, respectively, relative to climatological values, likely also reflecting the late 2020 onset of La Niña conditions (Takahashi et al. 2014; Jiang et al. 2019; Sutton et al. 2019).

Overall, 2020 fCO_2 and pH_{total} observations around the northern Pacific Ocean were consistent with historical observations in showing the highest variability and averages in northeastern Pacific ecosystems, followed by the central and eastern equatorial Pacific, and the lowest variability and moderate averages in the western Pacific low latitudes and the subtropical NPG. These differences in mean conditions and variability largely reflect the buffering effects of higher alkalinity in the southwestern Pacific compared to the northeastern North Pacific. Moderately anomalous ocean acidification conditions associated with SST anomalies and La Niña conditions were observed during the second half of 2020.

j. Global ocean carbon cycle—R. A. Feely, R. Wanninkhof, P. Landschützer, B. R. Carter, J. A. Triñanes, and C. Cosca

1) Introduction

The oceans play major roles in the global carbon cycle, including taking up a substantial fraction of the excess carbon dioxide (CO_2) that humans release into the atmosphere. As a consequence of humankind's collective CO_2 emissions into the atmosphere, referred to as "anthropogenic CO_2" (C_{anth}) emissions, atmospheric CO_2 concentrations have risen from pre-industrial levels of about 278 ppm (parts per million) to 412 ppm in 2020. Marine C_{anth} is the major cause of anthropogenic ocean acidification, with riverine C_{anth} and other atmospheric trace gases (e.g., nitrogen and sulfur gases) being other sources. Over the last decade, the global ocean has continued taking up a substantial fraction of the C_{anth} emissions and therefore is a major mediator of global climate change. Of the 11.5 (±0.9) Pg C yr^{-1} C_{anth} released from 2010 to 2019, about 2.5 (±0.6) Pg C yr^{-1} (23%) accumulated in the ocean, 3.4 (±0.6) Pg C yr^{-1} (29%) accumulated on land, and 5.1 (±0.02) Pg C yr^{-1} (44%) remained in the atmosphere with an imbalance of −0.1 Pg C yr^{-1} (4%; Table 6 in Friedlingstein

et al. 2020). This decadal ocean carbon uptake consensus estimate combines measured decadal CO_2 inventory changes, models, and global air–sea CO_2 flux estimates based on surface ocean fugacity of CO_2 (fCO_{2w}) measurements[1] from ships and moorings. The oceanic anthropogenic carbon sink has grown from 1.0 (±0.3) Pg C yr^{-1} in the decade of the 1960s to 2.6 (±0.6) Pg C yr^{-1} in 2019 (Friedlingstein et al. 2020).

2) Air–sea carbon dioxide fluxes

Ocean uptake of CO_2 is estimated from the net air–sea CO_2 flux derived from the bulk flux formula with air (a) minus surface seawater (w) differences in CO_2 fugacity ($\Delta fCO_2 = fCO_{2w} - fCO_{2a}$) and gas transfer coefficients as input. Gas transfer is parameterized with wind as described in Wanninkhof (2014). This provides a net flux estimate. To determine the C_{anth} fluxes into the ocean, several other processes need to be considered. A steady contribution of carbon from riverine runoff, originating from organic and inorganic detritus from land, with estimates ranging from 0.45 to 0.78 Pg C yr^{-1} (Resplandy et al. 2018) needs to be included. We use 0.6 Pg C yr^{-1} as the riverine adjustment. We assume other factors such as natural carbon deposition into the sea floor and margins are small. C_{anth} flux is therefore defined here as the sum of the net flux minus the riverine adjustment. The data sources for fCO_{2w} are annual updates of observations from the Surface Ocean CO_2 Atlas (SOCAT) composed of mooring, uncrewed surface vehicle, and ship-based observations (Bakker et al. 2016), and the database with ship-based observations (Takahashi et al. 2020). The increased observations and improved mapping techniques, including neural network methods summarized in Rödenbeck et al. (2015), now provide global fCO_{2w} fields on a 1° latitude × 1° longitude grid at monthly time scales. This allows investigation of variability on monthly to decadal time scales.

The monthly 2020 ΔfCO_2 maps are based on the observation-trained neural network (NN; artificial intelligence) approach of Landschützer et al. (2013, 2014). The 2020 values are projections using the NN predictor variables based on sea surface temperatures (SST), sea surface salinity (SSS), satellite chlorophyll-a (Chl*a*), and atmospheric CO_2 for 2020; a climatological mixed layer depth product (de Boyer Montegut et al. 2004); and an NN approach for fCO_{2w} developed using SOCAT data from 1982 through December 2019. The 2020 estimate uses the monthly ERA5 wind fields for the fluxes, as the cross-calibrated multi-platform winds (Atlas et al. 2011) used for previous years are not available (Fig. 3.27).

The NN results show an increasing ocean sink in the first part of the record from 1982 to 1994, followed by a period of rapidly decreasing uptake from 1995 to 2000 with no definite attribution. Thereafter, the NN results show a strong

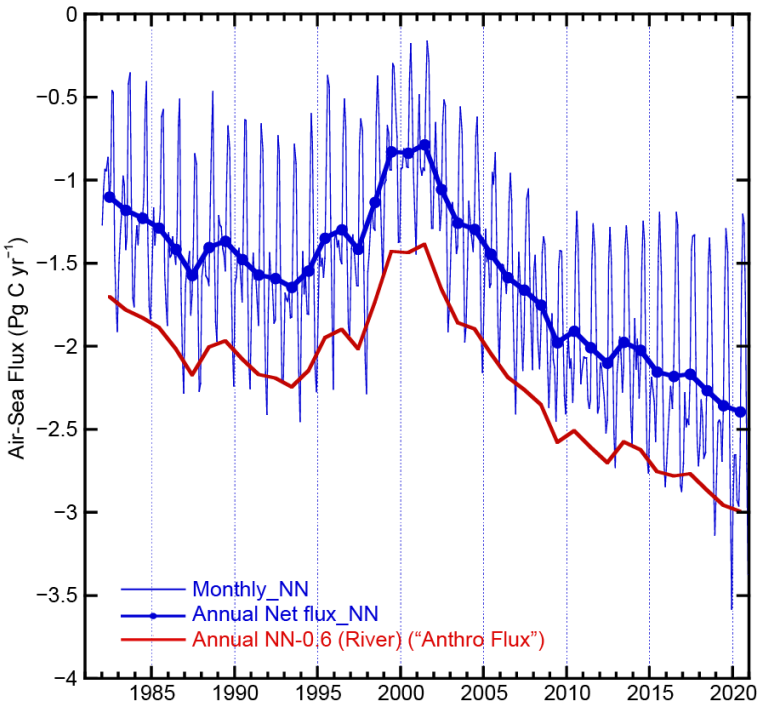

Fig. 3.27. Global annual (thick blue line) and monthly (thin blue line) net CO_2 fluxes (Pg C yr^{-1}) for 1982–2020 using a Neural Network (NN) approach. The red line is the anthropogenic CO_2 flux, that is the net flux including a riverine adjustment of −0.6 Pg C. Negative values indicate CO_2 uptake by the ocean.

[1] The fugacity is the partial pressure of CO_2 (pCO_2) corrected for non-ideality. They are numerically similar for surface waters with $fCO_2 \approx 0.997\ pCO_2$.

increase in the ocean sink from 2001 onward that continues through 2020 with a 0.03 Pg C yr^{-1} increase for the NN in 2020 over 2019. The amplitude of seasonal variability for the NN approach is ≈1 Pg C with minimum uptake from June to September, with a seasonal cycle amplitude exceeding interannual uptake variations. The C_{anth} flux of 3.0 Pg C yr^{-1} for 2020 from the NN approach in 2020 is 29% above the 1999–2019 average of 2.33 (±0.52) Pg C yr^{-1}.

The annual average flux map for 2020 (Fig. 3.28a) shows the characteristic pattern of effluxes (ocean-to-air CO_2 fluxes) in the tropics as well as coastal and open ocean upwelling zones. Coastal upwelling regions include the Arabian Sea and off the west coasts of North and South America. The western Bering Sea in the northwest Pacific was a strong CO_2 source as well in 2020. The region with the largest efflux is the upwelling region of the eastern and central equatorial Pacific. Cumulatively, the regions of effluxes are significant CO_2 sources to the atmosphere (≈ 1 Pg C). The primary uptake regions are in the subtropical and subpolar regions. The largest sinks are observed poleward of the subtropical fronts. The frontal positions determine the location of the maximum uptake. This sink is weaker in the Pacific sector of the Southern Ocean compared to the other basins.

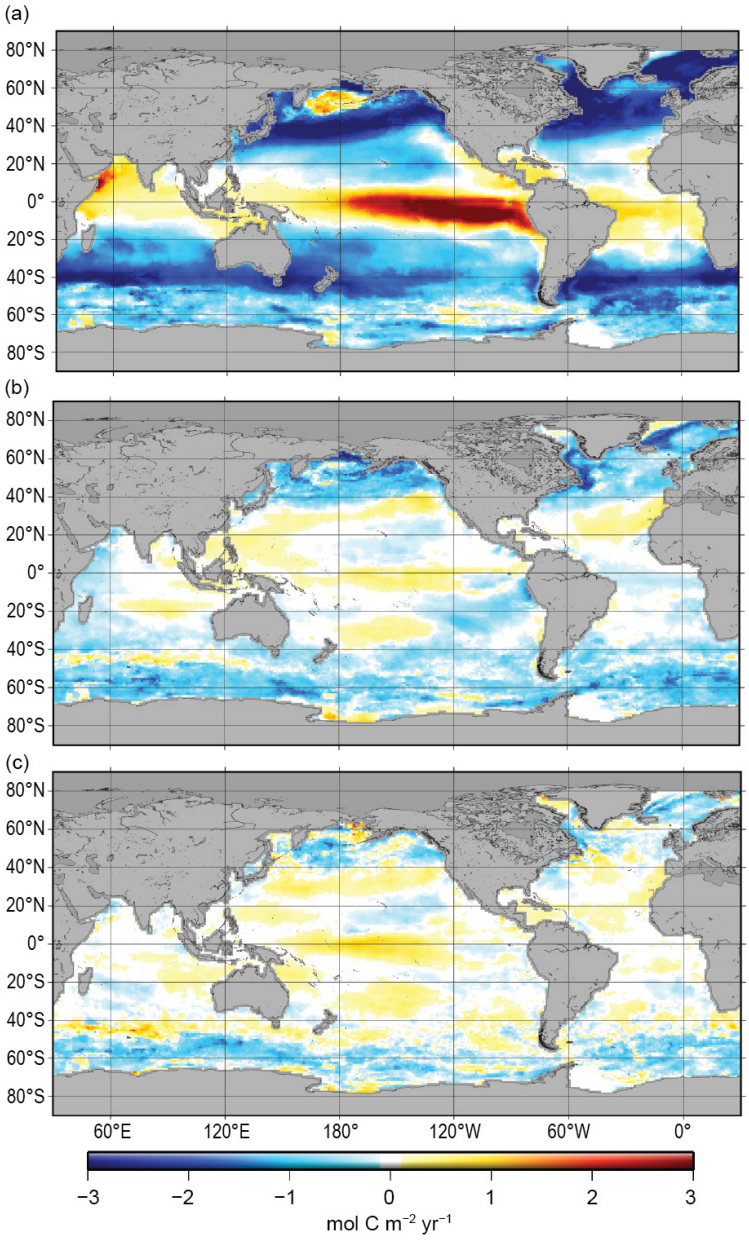

Fig. 3.28. Global map of (a) net air–sea CO_2 fluxes for 2020, with ocean CO_2 uptake regions shown in blue. (b) Net air–sea CO_2 flux anomalies for 2020 relative to the 1997–2018 average using the NN approach of Landschützer et al. (2013), and (c) net air–sea CO_2 flux anomalies for 2020 minus 2019. All maps have units of mol C m^{-2} yr^{-1}.

In the Northern Hemisphere, there is a significant asymmetry in fluxes in the sub-Arctic gyres, with the North Atlantic being a large CO_2 sink while the North Pacific's Bering Sea is a CO_2 source. This difference is partly due to the position of the western boundary currents whose cooling waters are known to contribute to CO_2 sinks at high latitudes: the Gulf Stream/North Atlantic Drift in the Atlantic extends farther north than the Kuroshio in the Pacific (Takahashi et al. 2009).

The ocean carbon uptake anomalies (Fig. 3.28b) in 2020 relative to the 1997–2018 average are attributed to the increasing ocean CO_2 uptake with time due to atmospheric CO_2 increases (Fig. 3.27) and to variations in large-scale climate modes. The long-term air–sea flux trend since the minimum uptake in 2000 is −0.72 Pg C $decade^{-1}$ (blue shading in Fig. 3.28c). Despite this trend, there are several large regions showing positive anomalies for 2020. Notably large positive anomalies are seen in the central equatorial Pacific; in a broad band running northwest across the subtropical northwest Pacific (from ≈20° to 40°N) attributed in the northeastern edge of the band to the North Pacific marine heat wave (Sidebar 3.1, see section 2b3); and in the western central to eastern subtropical Atlantic. The increased effluxes in the central equatorial Pacific are related to

the Oceanic Niño Index (ONI) turning negative in 2020, indicating La Niña conditions following a period of predominantly positive ONI (i.e., more El Niño-like conditions) in the preceding two years. The negative SST anomalies (Fig. 3.1a) indicate increased upwelling of waters with high CO_2 content in the central Pacific returning after a period of lower-than-normal upwelling. Of note, the eastern equatorial Pacific southeast of the Galapagos shows a negative CO_2 flux anomaly. The positive anomalies in fluxes (i.e., more efflux/less influx in 2020 compared to the long-term mean) in the subtropics closely correspond to positive temperature anomalies (Fig. 3.1), showing that the flux anomalies in these regions are temperature driven. The difference in fluxes between 2020 and 2019 (Fig. 3.28c) are similar to the anomalies (Fig. 3.28b).

The oceanic variability of the air–sea exchange fluxes in the tropical Pacific are largely controlled by the surface ocean variability and wind forcing influenced by the type and phasing of the El Niño-Southern Oscillation events (e.g., Feely et al. 1999, 2002, 2006, 2019; Ishii et al. 2009, 2014, 2020; Takahashi et al. 2009; Wanninkhof et al. 2013; Landschützer et al. 2014, 2016). The central and eastern equatorial Pacific is a major source of CO_2 to the atmosphere during neutral and La Niña periods, a weak source during weak El Niño periods, and near-neutral during strong El Niño periods. El Niño is characterized by a large-scale weakening of the trade winds, a decrease in upwelling of CO_2 and nutrient-rich subsurface waters, and a corresponding warming of SST in the eastern and central equatorial Pacific. La Niña is characterized by strong trade winds, cold tropical SSTs, and enhanced upwelling along the equator. During the strong eastern Pacific El Niño events of 1982–83, 1997–98, and 2015–16, the cold waters of the eastern equatorial Pacific disappear and fCO_2 values are close to equilibrium with the atmosphere (FIG. 3.29), whereas during the weaker central Pacific El Niños of 1991–94, 2002–05, 2006–07, and 2009–10, the equatorial

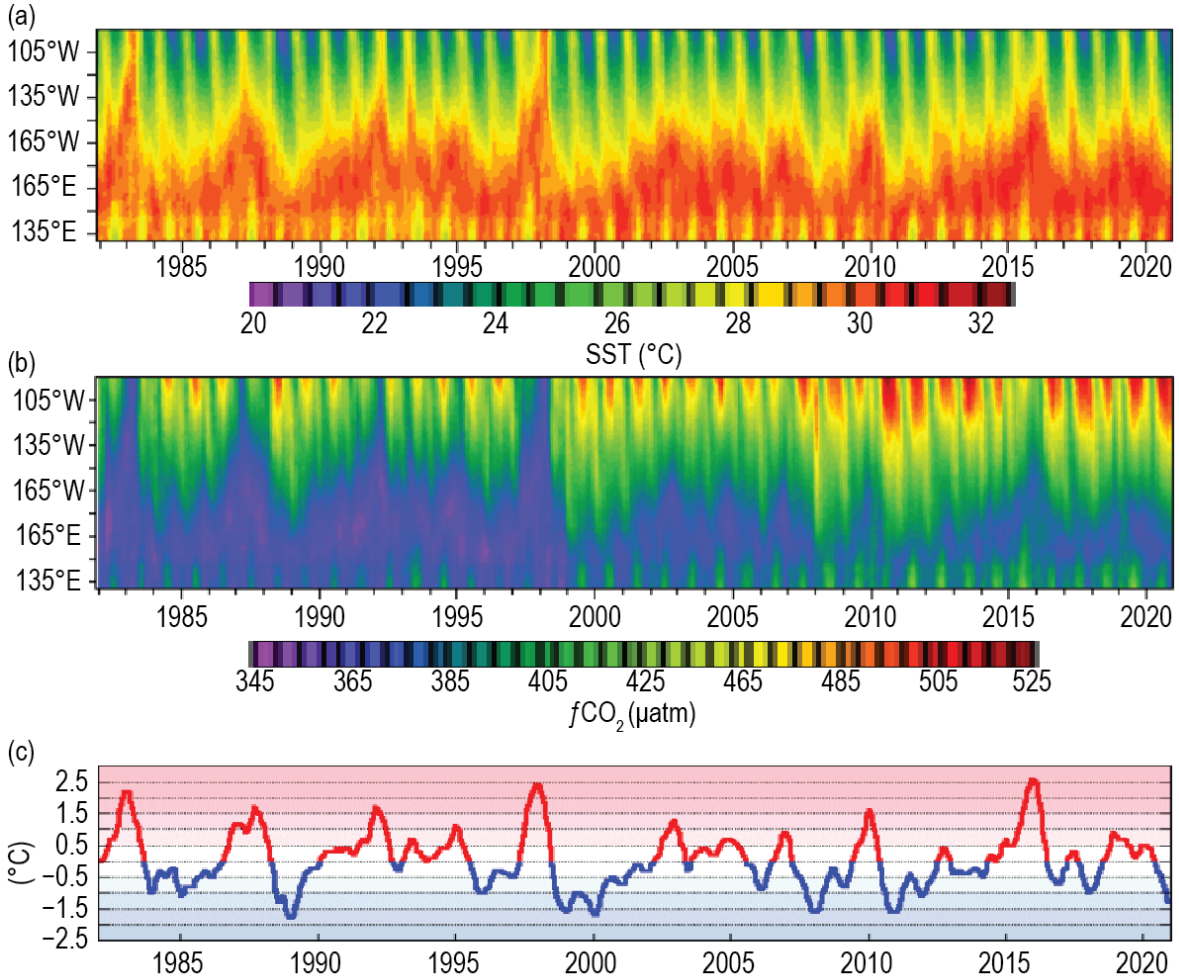

Fig. 3.29. Time–longitude plots of (a) SST (°C), (b) fCO_2 (µatm) from 1982–2020 in the equatorial Pacific, and (c) the Oceanic Niño Index (°C).

cold tongue is present but less pronounced, and fCO_2 values are higher than atmospheric values but lower than corresponding values for non-El Niño periods. The strong 1997–98 El Niño has SST anomalies exceeding 4°C and the lowest fCO_2 values throughout most of the equatorial Pacific. In contrast, the 2015–16 El Niño has SST anomalies that are similar to those seen during the 1997–98 event, yet the fCO_2 values were significantly higher because the upwelling-favorable winds were stronger in the easternmost and westernmost parts of the region. La Niña conditions returned in summer and autumn of 2020 (see section 4b) and were characterized by low SST and high fCO_2 levels throughout the entire tropical Pacific, but were mostly enriched in the central portion of the equatorial belt relative to previous years.

3) Large-scale carbon changes in the ocean interior

Global-scale CO_2 emissions from human activities are causing ocean interior C_{anth} increases and acidification. Delineating how the biogeochemical processes in the ocean interior will be affected by the changing heat content and C_{anth} uptake is essential for developing future mitigation and adaptation responses to climate change. Anthropogenic carbon accumulation occurs against a backdrop of vigorous natural marine carbon cycling. In the well-lit surface ocean, photosynthesizing organisms take up dissolved inorganic carbon to form organic matter, and some organisms form their shells and hard parts out of carbonate minerals. A portion of the organic matter and carbonate mineral matter that is formed or precipitated sinks into the interior ocean where it is remineralized, releasing the carbon back into the interior ocean. This biological transport of dissolved inorganic carbon from the surface ocean into the interior ocean is called the "soft" and "hard" tissue pumps. Several recently produced data products—i.e., interior ocean data products (Olsen et al. 2016, 2020), seawater property estimation algorithms (Carter et al. 2017), and circulation fields based on model simulations that assimilate interior-ocean observations (DeVries et al. 2017)—were combined to produce a new carbon data product containing estimates of the properties that seawater would have in the absence of this natural interior ocean biogeochemical cycling (Fig. 3.30; Carter et al. 2021). The dissolved inorganic carbon accumulated from the hard and soft tissue pumps can be quantified as the difference between the observed values and those estimated from several seawater properties. These estimates suggest the ocean holds 1300 Pg C of carbon from remineralized organic matter and 560 Pg C from dissolution of carbonate mineral phases. This is ~500 Pg C less carbon from organic matter than would be calculated using the assumption that all interior ocean water masses were initially 100% saturated with oxygen. The carbonate mineral dissolution accumulations found in this study are more evenly spread across the water column than those from previous estimates, suggesting a more uniform carbonate mineral dissolution rate with depth than was previously found.

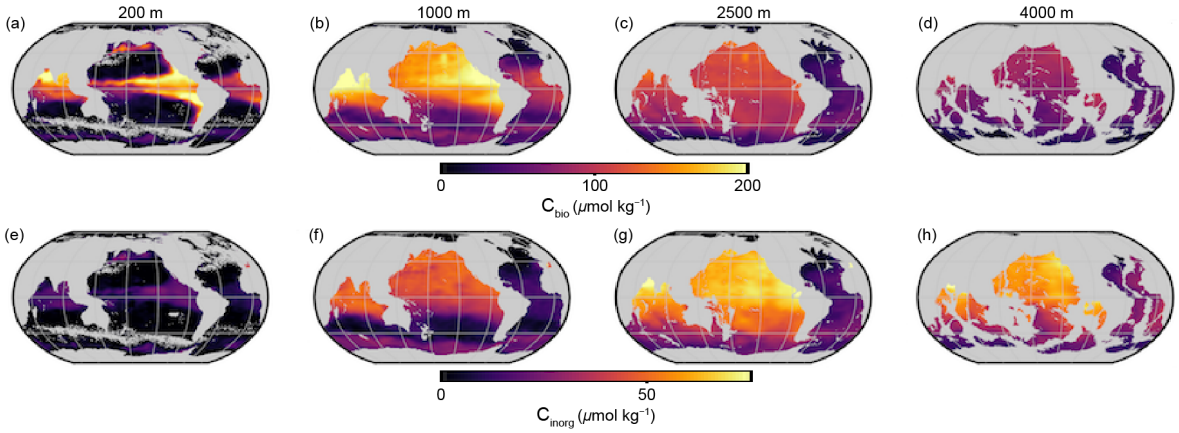

Fig. 3.30. Maps of the accumulation of dissolved inorganic carbon (μmol kg^{-1}) from (a–d) remineralized organic matter (C_{bio}) and from (e–h) dissolution of carbonate minerals (C_{inorg}) at (a,e) 200 m, (b,f) 1000 m, (c,g) 2500 m, and (d,h) 4000 m.

Acknowledgments

- Sandra Bigley provided invaluable editorial support for Chapter 3. Internal reviewers, external reviews, and report editors all provided comments that helped to improve the chapter.
- Argo data used in the chapter were collected and made freely available by the International Argo Program and the national programs that contribute to it. (https://argo.ucsd.edu, https://www.ocean-ops.org). The Argo Program is part of the Global Ocean Observing System. Many authors of the chapter are supported by NOAA Research, the NOAA Global Ocean Monitoring and Observing Program, or the NOAA Ocean Acidification Program.
- L. Cheng is supported by National Natural Science Foundation of China (42076202) and Strategic Priority Research Program of the Chinese Academy of Sciences (XDB42040402.
- R. E. Killick is supported by the Met Office Hadley Centre Climate Programme funded by BEIS and Defra. PMEL contribution numbers 5214, 5215, 5216, 5217, and 5247.

Chapter 3 – Acronyms

ACC	Antarctic Circumpolar Current
AMOC	Atlantic meridional overturning circulation
BASS	Blended Analysis of Surface Salinity
C_{anth}	anthropogenic CO_2
CCS	California Current System
CERES	Clouds and the Earth's Radiant Energy System
Chl*a*	chlorophyll-*a*
CO_2	carbon dioxide
COARE	Coupled Ocean-Atmosphere Response Experiment
C_{phy}	phytoplankton carbon
DJF	December–February
DOISST	Daily Optimum Interpolation ST version 2.1
E	evaporation
E–*P*	evaporation minus precipitation
EBAF	Energy Balanced and Filled
EKE	eddy kinetic energy
ENSO	El Niño–Southern Oscillation
ERSSTv5	Extended Reconstruction Sea Surface Temperature version 5
FC	Florida Current
FLASHFlux	Fast Longwave And Shortwave Radiative Fluxes
GMSL	global mean sea level
GPCP	Global Precipitation Climatology Project
GRACE	Gravity Recovery and Climate Experiment
GRACE-FO	Gravity Recovery and Climate Experiment Follow-On
HadSST	Hadley Centre SST
IO	Indian Ocean
IOD	Indian Ocean dipole
ITCZ	Intertropical Convergence Zone
JJA	June–August
LH	latent heat
LIARv2	Locally Interpolated Alkalinity Regression
LW	longwave
MAM	March–May
MEI	Multivariate ENSO Index
MHHW	mean higher high water
MHT	meridional heat transport
MHW	marine heat wave
MOC	meridional overturning circulation
MODIS	Moderate Resolution Imaging Spectroradiometer
MODIS-A	MODIS on *Aqua*
NAC	North Atlantic Current
NECC	North Equatorial Countercurrent
NH	Northern Hemisphere
NN	Neural Network
NPG	North Pacific Gyre
NPP	net primary production
OAFlux	Objectively Analyzed air-sea Fluxes

OHCA	ocean heat content anomaly
ONI	Oceanic Niño Index
OSNAP	Overturning in the Subpolar North Atlantic Program
P	precipitation
PACE	Plankton, Aerosol, Cloud, ocean Ecosystem
P – *E*	precipitation minus evaporation
PIES	Pressure-equipped inverted echo sounder
PNA	Pacific/North American
ppm	parts per million
PSO	permanently stratified ocean
RAPID/MOCHA/WBTS	Rapid Climate Change/MOC and Heatflux Array/Western Boundary Time Series
RF	Random Forest
SAMBA	South Atlantic MOC Basin-wide Array
Sea-WiFS	Sea-viewing Wide Field-of-view Sensor
SEC	South Equatorial Current
SH	sensible heat flux
SH	Southern Hemisphere
SJDF	Strait of Juan de Fuca
SMAP	Soil Moisture Active Passive
SMOS	Soil Moisture and Ocean Salinity
SOCAT	Surface Ocean CO_2 Atlas
SON	September–November
SPCZ	South Pacific Convergence Zone
SSM/I	Special Sensor Microwave/Imager
SSS	sea surface salinity
SST	sea surface temperature
SSTA	sea surface temperature anomaly
std. dev.	standard deviation
SW	shortwave
TRACOS	Tropical Atlantic Circulation and Overturning at 11°S
XBT	eXpendable BathyThermograph

References

Abraham, J. P., and Coauthors, 2013: A review of global ocean temperature observations: Implications for ocean heat content estimates and climate change. *Rev. Geophys.*, **51**, 450–483, https://doi.org/10.1002/rog.20022.

Adler, R. F., and Coauthors, 2018: The Global Precipitation Climatology Project (GPCP) monthly analysis (new version 2.3) and a review of 2017 global precipitation. *Atmosphere*, **9**, 138, https://doi.org/10.3390/atmos9040138.

Alexander, M. A., J. D. Scott, K. D. Friedland, K. E. Mills, J. A. Nye, A. J. Pershing, and A. C. Thomas, 2018: Projected sea surface temperatures over the 21st century: Changes in the mean, variability and extremes for large marine ecosystem regions of northern oceans. *Elementa*, **6**, 9, https://doi.org/10.1525/elementa.191.

Alin, S. R., R. A. Feely, A. Collins, and C.E. Cosca, 2021: Fugacity of carbon dioxide (fCO2), temperature, salinity and other variables collected from surface underway observations using shower head equilibrator, carbon dioxide gas detector and other instruments from the M/V Bluefin cruises in the Tropical and North Pacific Ocean from 2020-02-26 to 2020-10-26 (NCEI Accession 0225428). NOAA National Centers for Environmental Information, accessed 24 April 2021, https://doi.org/10.25921/kk66-zz33.

Amaya, D. J., A. J. Miller, S. P. Xie, and Y. Kusaka, 2020: Physical drivers of the summer 2019 North Pacific marine heatwave. *Nat. Commun.*, **11**, 1903, https://doi.org/10.1038/s41467-020-15820-w.

——, M. A. Alexander, A. Capotondi, C. Deser, K. B. Karnauskas, A. J. Miller, and N. J. Mantua, 2021: Are long-term changes in mixed layer depth influencing North Pacific marine heatwaves? [in "Explaining Extremes of 2019 from a Climate Perspective"]. *Bull. Amer. Meteor. Soc.*, **102** (1), S59–S66, https://doi.org/10.1175/BAMS-D-20-0144.1.

Atlas, R., R. N. Hoffman, J. Ardizzone, S. M. Leidner, J. C. Jusem, D. K. Smith, and D. Gombos, 2011: A cross-calibrated multiplatform ocean surface wind velocity product for meteorological and oceanographic applications. *Bull. Amer. Meteor. Soc.*, **92**, 157–174, https://doi.org/10.1175/2010BAMS2946.1.

Babcock, R. C., and Coauthors, 2019: Severe continental-scale impacts of climate change are happening now: Extreme climate events impact marine habitat forming communities along 45% of Australia's coast. *Front. Mar. Sci.*, **6**, 411, https://doi.org/10.3389/fmars.2019.00411.

Bakker, D. C. E., and Coauthors, 2016: A multi-decade record of high quality fCO2 data in version 3 of the surface ocean CO2 Atlas (SOCAT). *Earth Syst. Sci. Data*, **8**, 383–413, https://doi.org/10.5194/essd-8-383-2016.

Balaguru, K., P. Chang, R. Saravanan, L. R. Leung, Z. Xu, M. Li, and J. S. Hsieh, 2012: Ocean barrier layers' effect on tropical cyclone intensification. *Proc. Natl. Acad. Sci. USA*, **109**, 14343–14347, https://doi.org/10.1073/pnas.1201364109.

Baumgartner, A., and E. Reichel, 1975: *The World Water Balance*. Elsevier, 179 pp.

Behrenfeld, M. J., and Coauthors, 2006: Climate-driven trends in contemporary ocean productivity. *Nature*, **444**, 752–755, https://doi.org/10.1038/nature05317.

——, and Coauthors, 2015: Revaluating ocean warming impacts on global phytoplankton. *Nat. Climate Change*, **6**, 323–330, https://doi.org/10.1038/nclimate2838.

Boening, C., J. K. Willis, F. W. Landerer, R. S. Nerem, and J. Fasullo, 2012: The 2011 La Niña: So strong, the oceans fell. *Geophys. Res. Lett.*, **39**, L19602, https://doi.org/10.1029/2012GL053055.

Bond, N. A., M. F. Cronin, H. Freeland, and N. Mantua, 2015: Causes and impacts of the 2014 warm anomaly in the NE Pacific. *Geophys. Res. Lett.*, **42**, 3414–3420, https://doi.org/10.1002/2015GL063306.

Bopp, L., and Coauthors, 2013: Multiple stressors of ocean ecosystems in the 21st century: projections with CMIP5 models. *Biogeosciences*, **10**, 6225–6245, https://doi.org/10.5194/bg-10-6225-2013.

Boyer, T. P., and Coauthors, 2013: *World Ocean Database 2013*. S. Levitus, Ed., NOAA Atlas NESDIS 72, 209 pp.

——, and Coauthors, 2018: *World Ocean Database 2018*. A.V. Mishonov, Ed., NOAA Atlas NESDIS 87, 207 pp.

Broecker, W. S., 1991: The Great Ocean Conveyor. *Oceanography*, **4**, 79–89, https://doi.org/10.5670/oceanog.1991.07.

Bulgin, C. E., C. J. Merchant, and D. Ferreira, 2020: Tendencies, variability and persistence of sea surface temperature anomalies. *Sci. Rep.*, **10**, 7986, https://doi.org/10.1038/s41598-020-64785-9.

Caesar, L., S. Rahmstorf, A. Robinson, G. Feulner, and V. Saba, 2018: Observed fingerprint of a weakening Atlantic Ocean overturning circulation. *Nature*, **556**, 191–196, https://doi.org/10.1038/s41586-018-0006-5.

Carter, B. R., and Coauthors, 2017: Two decades of Pacific anthropogenic carbon storage and ocean acidification along GO-SHIP Sections P16 and P02. *Global Biogeochem. Cycles*, **31**, 306–327, https://doi.org/10.1002/2016GB005485.

——, R. A. Feely, N. L. Williams, A. G. Dickson, M. B. Fong, and Y. Takeshita, 2018: Updated methods for global locally interpolated estimation of alkalinity, pH, and nitrate. *Limnol. Oceanogr. Methods*, **16**, 119–131, https://doi.org/10.1002/lom3.10232.

——, ——, S. K. Lauvset, A. Olsen, T. DeVries, and R. Sonnerup, 2021: Preformed properties for marine organic matter and carbonate mineral cycling quantification. *Global Biogeochem. Cycles*, **35**, e2020GB006623, https://doi.org/10.1029/2020GB006623.

Castro de la Guardia, L., X. Hu, and P. G. Myers, 2015: Potential positive feedback between Greenland Ice Sheet melt and Baffin Bay heat content on the west Greenland shelf. *Geophys. Res. Lett.*, **42**, 4922–4930, https://doi.org/10.1002/2015GL064626.

Chambers, D. P., A. Cazenave, N. Champollion, H. Dieng, W. Llovel, R. Forsberg, K. von Schuckmann, and Y. Wada, 2017: Evaluation of the global mean sea level budget between 1993 and 2014. *Surv. Geophys.*, **38**, 309–327, https://doi.org/10.1007/s10712-016-9381-3.

Chen, J., B. Tapley, C. Wilson, A. Cazenave, K. W. Seo, and J. S. Kim, 2020: Global ocean mass change from GRACE and GRACE follow-on and altimeter and Argo measurements. *Geophys. Res. Lett.*, **47**, e2020GL090656, https://doi.org/10.1029/2020GL090656.

Cheng, L., and Coauthors, 2020: Record-setting ocean warmth continued in 2019. *Adv. Atmos. Sci.*, **37**, 137–142, https://doi.org/10.1007/s00376-020-9283-7.

Chiang, J. C. H., and D. J. Vimont, 2004: Analagous meridional modes of atmosphere-ocean variability in the tropical Pacific and tropical Atlantic. *J. Climate*, **17**, 4143–4158, https://doi.org/10.1175/JCLI4953.1.

Christian, J. R., and T. Ono, Eds., 2019: Ocean acidification and deoxygenation in the North Pacific Ocean. PICES Special Publication 5, 116 pp.

Cornwall, W., 2019: A new 'Blob' menaces Pacific ecosystems. *Science*, **365**, 1233, https://doi.org/10.1126/science.365.6459.1233.

de Boyer Montegut, C., G. Madec, A. S. Fischer, A. Lazar, and D. Iudicone, 2004: Mixed layer depth over the global ocean: An examination of profile data and a profile-based climatology. *J. Geophys. Res.*, **109**, C12003, https://doi.org/10.1029/2004JC002378.

Deser, C., M. A. Alexander, S. P. Xie, and A. S. Phillips, 2010: Sea surface temperature variability: Patterns and mechanisms. *Annu. Rev. Mar. Sci.*, **2**, 115–143, https://doi.org/10.1146/annurev-marine-120408-151453.

DeVries, T., M. Holzer, and F. Primeau, 2017: Recent increase in oceanic carbon uptake driven by weaker upper-ocean overturning. *Nature*, **542**, 215–218, https://doi.org/10.1038/nature21068.

Dierssen, H. M., 2010: Perspectives on empirical approaches for ocean color remote sensing of chlorophyll in a changing climate. *Proc. Natl. Acad. Sci. USA*, **107**, 17073–17078, https://doi.org/10.1073/pnas.0913800107.

Dima, M., and G. Lohmann, 2010: Evidence for two distinct modes of large-scale ocean circulation changes over the last century. *J. Climate*, **23**, 5–16, https://doi.org/10.1175/2009JCLI2867.1

Domingues, R., and Coauthors, 2015: Upper ocean response to Hurricane Gonzalo (2014): Salinity effects revealed by sustained and targeted observations from underwater gliders. *Geophys. Res. Lett.*, **42**, 7131–7138, https://doi.org/10.1002/2015GL065378.

——, M. Baringer, and G. Goni, 2016: Remote sources for year-to-year changes in the seasonality of the Florida Current transport. *J. Geophys. Res. Oceans*, **121**, 7547–7559, https://doi.org/10.1002/2016JC012070.

Dong, S., G. Goni, and F. Bringas, 2015: Temporal variability of the meridional overturning circulation in the South Atlantic between 20°S and 35°S. *Geophys. Res. Lett.*, **42**, 7655–7662, https://doi.org/10.1002/2015GL065603.

——, H. Lopez, S.-K. Lee, C. S. Meinen, G. J. Goni, and M. O. Baringer, 2020: What caused the large-scale heat deficit in the subtropical South Atlantic Ocean during 2009-2012? *Geophys. Res. Lett.*, **47**, e2020GL088206, https://doi.org/10.1029/2020GL088206.

Durack, P. J., 2015: Ocean salinity and the global water cycle. *Oceanography*, **28**, 20–31, https://doi.org/10.5670/oceanog.2015.03.

——, and S. E. Wijffels, 2010: Fifty-year trends in global ocean salinities and their relationship to broad-scale warming. *J. Climate*, **23**, 4342–4362, https://doi.org/10.1175/2010JCLI3377.1.

——, ——, and R. J. Matear, 2012: Ocean salinities reveal strong global water cycle intensification during 1950 to 2000. *Science*, **336**, 455–458, https://doi.org/10.1126/science.1212222.

Egleston, E. S., C. L. Sabine, and F. M. M. Morel, 2010: Revelle revisited: Buffer factors that quantify the response of ocean chemistry to changes in DIC and alkalinity. *Global Biogeochem. Cycles*, **24**, GB1002, https://doi.org/10.1029/2008GB003407.

Esaias, W. E., and Coauthors, 1998: An overview of MODIS capabilities for ocean science observations. *IEEE Trans. Geosci. Remote Sens.*, **36**, 1250–1265, https://doi.org/10.1109/36.701076.

Ezer, T., and L. P. Atkinson, 2014: Accelerated flooding along the U.S. East Coast: On the impact of sea-level rise, tides, storms, the Gulf Stream, and the North Atlantic Oscillations. *Earth's Future*, **2**, 362–382, https://doi.org/10.1002/2014EF000252.

Fairall, C. W., E. F. Bradley, J. E. Hare, A. A. Grachev, and J. B. Edson, 2003: Bulk parameterization of air–sea fluxes: Updates and verification for the COARE algorithm. *J. Climate*, **16**, 571–591, https://doi.org/10.1175/1520-0442(2003)016<0571:BPOASF>2.0.CO;2.

Falkowski, P. G., R. T. Barber, and V. Smetacek, 1998: Biogeochemical controls and feedbacks on ocean primary production. *Science*, **281**, 200–206, https://doi.org/10.1126/science.281.5374.200.

Fassbender, A. J., and Coauthors, 2018: Seasonal carbonate chemistry variability in marine surface waters of the Pacific Northwest. *Earth Syst. Sci. Data*, **10**, 1367–1401, https://doi.org/10.5194/essd-10-1367-2018.

Fasullo, J. T., and P. R. Gent, 2017: On the relationship between regional ocean heat content and sea surface height. *J. Climate*, **30**, 9195–9211, https://doi.org/10.1175/JCLI-D-16-0920.1.

——, and R. S. Nerem, 2018: Altimeter-era emergence of the patterns of forced sea-level rise in climate models and implications for the future. *Proc. Natl. Acad. Sci. USA*, **115**, 12 944–12 949, https://doi.org/10.1073/pnas.1813233115.

——, R. S. Nerem, and B. Hamlington, 2016: Is the detection of accelerated sea level rise imminent? *Sci. Rep.*, **6**, 31245, https://doi.org/10.1038/srep31245.

Feely, R. A., R. Wanninkhof, T. Takahashi, and P. Tans, 1999: Influence of El Niño on the equatorial Pacific contribution of atmospheric CO2 accumulation. *Nature*, **398**, 597–601, https://doi.org/10.1038/19273.

——, and Coauthors, 2002: Seasonal and interannual variability of CO2 in the equatorial Pacific. *Deep-Sea Res. II*, **49**, 2443–2469, https://doi.org/10.1016/S0967-0645(02)00044-9.

——, T. Takahashi, R. Wanninkhof, M. J. McPhaden, C. E. Cosca, S. C. Sutherland, and M.-E. Carr, 2006: Decadal variability of the air-sea CO2 fluxes in the equatorial Pacific Ocean. *J. Geophys. Res.*, **111**, C08S90, https://doi.org/10.1029/2005JC003129.

——, S. R. Alin, J. Newton, C. L. Sabine, M. Warner, A. Devol, C. Krembs, and C. Maloy, 2010: The combined effects of ocean acidification, mixing, and respiration on pH and carbonate saturation in an urbanized estuary. *Estuarine Coastal Shelf Sci.*, **88**, 442–449, https://doi.org/10.1016/j.ecss.2010.05.004.

——, R. Wanninkhof, B. R. Carter, P. Landschützer, A. J. Sutton, C. Cosca, and J. A. Triñanes, 2019: Global ocean carbon cycle [in "State of the Climate in 2018"]. *Bull. Amer. Meteor. Soc.*, **100** (9), S94–S99, https://doi.org/10.1175/2019BAMSStateoftheClimate.1.

Ffield, A., 2007: Amazon and Orinoco River plumes and NBC rings: Bystanders or participants in hurricane events? *J. Climate*, **20**, 316–333, https://doi.org/10.1175/JCLI3985.1.

Field, C. B., M. J. Behrenfeld, J. T. Randerson, and P. Falkowski, 1998: Primary production of the biosphere: Integrating terrestrial and oceanic components. *Science*, **281**, 237–240, https://doi.org/10.1126/science.281.5374.237.

Fofonoff, N. P., and E. L. Lewis, 1979: A practical salinity scale. *J. Oceanogr. Soc. Japan*, **35**, 63–64, https://doi.org/10.1007/BF02108283.

Font, J., and Coauthors, 2013: SMOS first data analysis for sea surface salinity determination. *Int. J. Remote Sens.*, **34**, 3654–3670, https://doi.org/10.1080/01431161.2012.716541.

Fore, A. G., S. H. Yueh, W. Q. Tang, B. W. Stiles, and A. K. Hayashi, 2016: Combined active/passive retrievals of ocean vector wind and sea surface salinity with SMAP. *IEEE Trans. Geosci. Remote Sens.*, **54**, 7396–7404, https://doi.org/10.1109/TGRS.2016.2601486.

Frajka-Williams, E., and Coauthors, 2019: Atlantic meridional overturning circulation: Observed transports and variability. *Front. Mar. Sci.*, **6**, 260, https://doi.org/10.3389/fmars.2019.00260.

Franz, B. A., I. Cetinić, J. P. Scott, D. A. Siegel, and T. K. Westberry, 2020: Global ocean phytoplankton [in "State of the Climate in 2019"]. *Bull. Amer. Meteor. Soc.*, **101** (8), S163–S169, https://doi.org/10.1175/BAMS-D-20-0105.1.

Frederikse, T., and Coauthors, 2020: The causes of sea-level rise since 1900. *Nature*, **584**, 393–397, https://doi.org/10.1038/s41586-020-2591-3.

Friedlingstein, P., and Coauthors, 2020: Global carbon budget 2020. *Earth Syst. Sci. Data*, **12**, 3269–3340, https://doi.org/10.5194/essd-12-3269-2020.

Geider, R. J., H. L. MacIntyre, and T. M. Kana, 1997: Dynamic model of phytoplankton growth and acclimation: Responses of the balanced growth rate and the chlorophyll a:carbon ratio to light, nutrient limitation and temperature. *Mar. Ecol. Prog. Ser.*, **148**, 187–200, https://doi.org/10.3354/meps148187.

Gentemann, C. L., M. R. Fewings, and M. García-Reyes, 2017: Satellite sea surface temperatures along the West Coast of the United States during the 2014–2016 northeast Pacific marine heat wave. *Geophys. Res. Lett.*, **44**, 312–319, https://doi.org/10.1002/2016GL071039.

Goni, G. J., and W. E. Johns, 2003: Synoptic study of warm rings in the North Brazil Current retroflection region using satellite altimetry. *Interhemispheric Water Exchange in the Atlantic Ocean*, G. J. Goni, and P. Malanotte-Rizzoli, Eds., Elsevier Oceanography Series, Vol. 68, Elsevier, 335–356, https://doi.org/10.1016/S0422-9894(03)80153-8.

——, and Coauthors, 2009: Applications of satellite-derived ocean measurements to tropical cyclone intensity forecasting. *Oceanography*, **22**, 190–197, https://doi.org/10.5670/oceanog.2009.78.

——, F. Bringas, and P. N. Di Nezio, 2011: Observed low frequency variability of the Brazil Current front. *J. Geophys. Res.*, **116**, C10037, https://doi.org/10.1029/2011JC007198.

Gordon, A. L., 1986: Interocean exchange of thermocline water. *J. Geophys. Res.*, **91**, 5037–5046, https://doi.org/10.1029/JC091iC04p05037.

Graff, J. R., and Coauthors, 2015: Analytical phytoplankton carbon measurements spanning diverse ecosystems. *Deep-Sea Res. I*, **102**, 16–25, https://doi.org/10.1016/j.dsr.2015.04.006.

Gruber, N., and Coauthors, 2019: The oceanic sink for anthropogenic CO2 from 1994 to 2007. *Science*, **363**, 1193–1199, https://doi.org/10.1126/science.aau5153.

Hamlington, B. D., J. T. Fasullo, R. S. Nerem, K. Kim, and F. W. Landerer, 2019: Uncovering the pattern of forced sea level rise in the satellite altimeter record. *Geophys. Res. Lett.*, **46**, 4844–4853, https://doi.org/10.1029/2018GL081386.

——, C. G. Piecuch, J. T. Reager, H. Chandanpurkar, T. Frederikse, R. S. Nerem, J. T. Fasullo, and S.-H. Cheon, 2020: Origin of interannual variability in global mean sea level. *Proc. Natl. Acad. Sci. USA*, **117**, 13983–13990, https://doi.org/10.1073/pnas.1922190117.

Han, W., G. A. Meehl, D. Stammer, A. Hu, B. Hamlington, J. Kenigson, H. Palanisamy, and P. Thompson, 2017: Spatial patterns of sea level variability associated with natural internal climate modes. *Surv. Geophys.*, **38**, 217–250, https://doi.org/10.1007/s10712-016-9386-y.

Held, I. M., and B. J. Soden, 2006: Robust responses of the hydrological cycle to global warming. *J. Climate*, **19**, 5686–5699, https://doi.org/10.1175/JCLI3990.1.

Herrford, J., P. Brandt, T. Kanzow, R. Hummels, M. Araujo, and J. V. Durgadoo, 2021: Seasonal variability of the Atlantic Meridional Overturning Circulation at 11°S inferred from bottom pressure measurements. *Ocean Sci.*, **17**, 265–284, https://doi.org/10.5194/os-17-265-2021.

Hobday, A. J., and Coauthors, 2016: A hierarchical approach to defining marine heatwaves. *Prog. Oceanogr.*, **141**, 227–238, https://doi.org/10.1016/j.pocean.2015.12.014.

Hu, C., Z. Lee, and B. A. Franz, 2012: Chlorophyll a algorithms for oligotrophic oceans: A novel approach based on three-band reflectance difference. *J. Geophys. Res.*, **117**, C01011, https://doi.org/10.1029/2011JC007395.

Hu, Z.-Z., A. Kumar, B. Huang, Y. Xue, W. Wang, and B. Jha, 2011: Persistent atmospheric and oceanic anomalies in the North Atlantic from summer 2009 to summer 2010. *J. Climate*, **24**, 5812–5830, https://doi.org/10.1175/2011JCLI4213.1.

Huang, B., and Coauthors, 2015: Extended reconstructed sea surface temperature version 4 (ERSST.v4). Part I: Upgrades and intercomparisons. *J. Climate*, **28**, 911–930, https://doi.org/10.1175/JCLI-D-14-00006.1.

——, and Coauthors, 2017: Extended reconstructed sea surface temperature version 5 (ERSSTv5): Upgrades, validations, and intercomparisons. *J. Climate*, **30**, 8179–8205, https://doi.org/10.1175/JCLI-D-16-0836.1.

——, and Coauthors, 2020: Uncertainty estimates for sea surface temperature and land surface air temperature in NOAAGlobalTemp version 5. *J. Climate*, **33**, 1351–1379, https://doi.org/10.1175/JCLI-D-19-0395.1.

——, C. Liu, V. Banzon, E. Freeman, G. Graham, B. Hankins, T. Smith, and H.-M. Zhang, 2021: Improvements of the Daily Optimum Interpolation Sea Surface Temperature (DOISST) version 2.1. *J. Climate*, **34**, 2923–2939, https://doi.org/10.1175/JCLI-D-20-0166.1.

Hummels, R., P. Brandt, M. Dengler, J. Fischer, M. Araujo, D. Veleda, and J. V. Durgadoo, 2015: Interannual to decadal changes in the western boundary circulation in the Atlantic at 11°S. *Geophys. Res. Lett.*, **42**, 7615–7622, https://doi.org/10.1002/2015GL065254.

Ishii, M., and Coauthors, 2009: Spatial variability and decadal trend of the oceanic CO2 in the western equatorial Pacific warm/fresh water. *Deep-Sea Res. II*, **56**, 591–606, https://doi.org/10.1016/j.dsr2.2009.01.002.

——, and Coauthors, 2014: Air-sea CO2 flux in the Pacific Ocean for the period 1990-2009. *Biogeosciences*, **11**, 709–734, https://doi.org/10.5194/bg-11-709-2014.

——, Y. Fukuda, S. Hirahara, S. Yasui, T. Suzuki, and K. Sato, 2017: Accuracy of global upper ocean heat content estimation expected from present observational datasets. *SOLA*, **13**, 163–167, https://doi.org/10.2151/sola.2017-030.

——, and Coauthors, 2020: Ocean acidification from below in the tropical Pacific. *Global Biogeochem. Cycles*, **34**, e2019GB006368, https://doi.org/10.1029/2019GB006368.

Jiang, L.-Q., R. A. Feely, B. R. Carter, D. J. Greeley, D. K. Gledhill, and K. M. Arzayus, 2015: Climatological distribution of aragonite saturation state in the global oceans. *Global Biogeochem. Cycles*, **29**, 1656–1673, https://doi.org/10.1002/2015GB005198.

——, B. R. Carter, R. A. Feely, S. K. Lauvset, and A. Olsen, 2019: Surface ocean pH and buffer capacity: Past, present and future. *Sci. Rep.*, **9**, 18624, https://doi.org/10.1038/s41598-019-55039-4.

Johnson, G. C., and J. M. Lyman, 2012: Sea surface salinity [in "State of the Climate in 2011"]. *Bull. Amer. Meteor. Soc.*, **93**, S68–S69, S72, https://doi.org/10.1175/2012BAMSStateoftheClimate.1

——, and A. N. Birnbaum, 2017: During El Niño, Pacific Warm Pool expands, ocean gains more heat. *Geophys. Res. Lett.*, **44**, 438–445, https://doi.org/10.1002/2016GL071767.

——, and J. M. Lyman, 2020: Warming trends increasingly dominate global ocean. *Nat. Climate Change*, **10**, 757–761, https://doi.org/10.1038/s41558-020-0822-0.

——, B. M. Sloyan, W. S. Kessler, and K. E. McTaggart, 2002: Direct measurements of upper ocean currents and water properties across the tropical Pacific Ocean during the 1990s. *Prog. Oceanogr.*, **52**, 31–61, https://doi.org/10.1016/S0079-6611(02)00021-6.

——, J. M. Lyman, J. K. Willis, T. Boyer, J. Antonov, S. A. Good, C. M. Domingues, and N. Bindoff, 2014: Ocean heat content [in "State of the Climate in 2013"]. *Bull. Amer. Meteor. Soc.*, **95** (7), S54–S57, https://doi.org/10.1175/2014BAMSStateoftheClimate.1.

——, and Coauthors, 2015: Ocean heat content [in "State of the Climate in 2014"]. *Bull. Amer. Meteor. Soc.*, **96** (7) , ES64–ES66, ES68, https://doi.org/10.1175/2015BAMSStateoftheClimate.1.

——, and Coauthors, 2020: Ocean heat content [in "State of the Climate in 2019"]. *Bull. Amer. Meteor. Soc.*, **101** (8), S140–S144, https://doi.org/10.1175/2020BAMSStateoftheClimate.1.

Josey, S. A., and Coauthors, 2018: The recent Atlantic cold anomaly: Causes, consequences, and related phenomena. *Annu. Rev. Mar. Sci.*, **10**, 475–501, https://doi.org/10.1146/annurev-marine-121916-063102.

Kato, S., and Coauthors, 2018: Surface irradiances of edition 4.0 Clouds and the Earth's Radiant Energy System (CERES) Energy Balanced and Filled (EBAF) data product. *J. Climate*, **31**, 4501–4527, https://doi.org/10.1175/JCLI-D-17-0523.1.

Kennedy, J. J., N. A. Rayner, R. O. Smith, D. E. Parker, and M. Saunby, 2011a: Reassessing biases and other uncertainties in sea surface temperature observations measured in situ since 1850: 1. Measurement and sampling errors. *J. Geophys. Res.*, **116**, D14103, https://doi.org/10.1029/2010JD015218.

——, ——, ——, ——, and ——, 2011b: Reassessing biases and other uncertainties in sea surface temperature observations measured in situ since 1850: 2: Biases and homogenization. *J. Geophys. Res.*, **116**, D14104, https://doi.org/10.1029/2010JD015220.

——, ——, C. P. Atkinson, and R. E. Killick, 2019: An ensemble data set of sea surface temperature change from 1850: The Met Office Hadley Centre HadSST.4.0.0.0 data set. *J. Geophys. Res. Atmos.*, **124**, 7719–7763, https://doi.org/10.1029/2018JD029867.

Kent, E. C., and Coauthors, 2017: A call for new approaches to quantifying biases in observations of sea surface temperature. *Bull. Amer. Meteor. Soc.*, **98**, 1601–1616, https://doi.org/10.1175/BAMS-D-15-00251.1.

Kersalé, M., and Coauthors, 2020: Highly variable upper and abyssal overturning cells in the South Atlantic. *Sci. Adv.*, **6**, eaba7573, https://doi.org/10.1126/sciadv.aba7573.

Kopte, R., P. Brandt, M. Dengler, P. C. M. Tchipalanga, M. Macuéria, and M. Ostrowski, 2017: The Angola Current: Flow and hydrographic characteristics as observed at 11°S. *J. Geophys. Res. Oceans*, **122**, 1177–1189, https://doi.org/10.1002/2016JC012374.

Lambert, H. R., 2019: 2019 albacore catch blows old record out of the water. KOIN.com, Accessed 11 February 2021, www.koin.com/news/oregon/2019-albacore-catch-blows-old-record-out-of-the-water/.

Landschützer, P., N. Gruber, D. C. E. Bakker, U. Schuster, S. Nakaoka, M. R. Payne, T. P. Sasse, and J. Zeng, 2013: A neural network-based estimate of the seasonal to inter-annual variability of the Atlantic Ocean carbon sink. *Biogeosciences*, **10**, 7793–7815, https://doi.org/10.5194/bg-10-7793-2013.

Landschützer, P., N. Gruber, D. C. E. Bakker, and U. Schuster, 2014: Recent variability of the global ocean carbon sink. *Global Biogeochem. Cycles*, **28**, 927–949, https://doi.org/10.1002/2014GB004853.

——, ——, and ——, 2016: Decadal variations and trends of the global ocean carbon sink. *Global Biogeochem. Cycles*, **30**, 1396–1417, https://doi.org/10.1002/2015GB005359.

Lankhorst, M., and U. Send, 2020: Uncertainty of North Atlantic Current observations from altimetry, floats, moorings, and XBT. *Prog. Oceanogr.*, **187**, 102402, https://doi.org/10.1016/j.pocean.2020.102402.

Laufkötter, C., J. Zscheischler, and T. L. Frölicher, 2020: High-impact marine heatwaves attributable to human-induced global warming. *Science*, **369**, 1621–1625, https://doi.org/10.1126/science.aba0690.

Leuliette, E. W., and J. K. Willis, 2011: Balancing the sea level budget. *Oceanography*, **24**, 122–129, https://doi.org/10.5670/oceanog.2011.32.

Le Vine, D. M., E. P. Dinnat, G. S. E. Lagerloef, P. de Matthaeis, S. Abraham, C. Utku, and H. Kao, 2014: Aquarius: Status and recent results. *Radio Sci.*, **49**, 709–720, https://doi.org/10.1002/2014RS005505.

Levitus, S., and Coauthors, 2012: World ocean heat content and thermosteric sea level change (0–2000 m), 1955–2010. *Geophys. Res. Lett.*, **39**, L10603, https://doi.org/10.1029/2012GL051106.

Li, G., L. Cheng, J. Zhu, K. Trenberth, M. Mann, and J. Abraham, 2020: Increasing ocean stratification over the past half-century. *Nat. Climate Change*, **10**, 1116–1123, https://doi.org/10.1038/s41558-020-00918-2.

Liu, W., S.-P. Xie, Z. Liu, and J. Zhu, 2017: Overlooked possibility of a collapsed Atlantic Meridional Overturning Circulation in warming climate. *Sci. Adv.*, **3**, e1601666, https://doi.org/10.1126/sciadv.1601666.

Llovel, W., and L. Terray, 2016: Observed southern upper-ocean warming over 2005–2014 and associated mechanisms. *Environ. Res. Lett.*, **11**, 124023, https://doi.org/10.1088/1748-9326/11/12/124023.

Loeb, N. G., and Coauthors, 2018: Clouds and the Earth's Radiant Energy System (CERES) Energy Balanced and Filled (EBAF) Top-of-Atmosphere (TOA) edition-4.0 data product. *J. Climate*, **31**, 895–918, https://doi.org/10.1175/JCLI-D-17-0208.1.

Long, X., M. J. Widlansky, F. Schloesser, P. R. Thompson, H. Annamalai, M. A. Merrifield, and H. Yoon, 2020: Higher sea levels at Hawaii caused by strong El Niño and weak trade winds. *J. Climate*, **33**, 3037–3059, https://doi.org/10.1175/JCLI-D-19-0221.1.

Lozier, M. S., and Coauthors, 2017: Overturning in the Subpolar North Atlantic Program: A new international ocean observing system. *Bull. Amer. Meteor. Soc.*, **98**, 737–752, https://doi.org/10.1175/BAMS-D-16-0057.1.

——, and Coauthors, 2019: Meridional overturning circulation and the associated heat and freshwater transports observed by the OSNAP (Overturning in the Subpolar North Atlantic Program) Array from 2014 to 2016. Duke Digital Repository, accessed 29 January 2021, https://doi.org/10.7924/r4z60gf0f.

Lumpkin, R., and S. Garzoli, 2011: Interannual to decadal changes in the western South Atlantic's surface circulation. *J. Geophys. Res.*, **116**, C01014, https://doi.org/10.1029/2010JC006285.

——, and G. C. Johnson, 2013: Global ocean surface velocities from drifters: Mean, variance, El Nino–Southern Oscillation response, and seasonal cycle. *J. Geophys. Res. Oceans*, **118**, 2992–3006, https://doi.org/10.1002/jgrc.20210.

——, G. Goni, and K. Dohan, 2011: State of the ocean in 2010: Surface currents [in "State of the Climate in 2010"]. *Bull. Amer. Meteor. Soc.*, **92** (6), S92–S95, https://doi.org/10.1175/1520-0477-92.6.S1.

Lyman, J. M., and G. C. Johnson, 2014: Estimating global ocean heat content changes in the upper 1800 m since 1950 and the influence of climatology choice. *J. Climate*, **27**, 1946–1958, https://doi.org/10.1175/JCLI-D-12-00752.1.

Majumder, S., C. Schmid, and G. Halliwell, 2016: An observations and model-based analysis of meridional transports in the South Atlantic. *J. Geophys. Res. Oceans*, **121**, 5622–5638, https://doi.org/10.1002/2016JC011693.

McCarthy, G. D., and Coauthors, 2020: Sustainable observations of the AMOC: Methodology and technology. *Rev. Geophys.*, **58**, e2019RG000654, https://doi.org/10.1029/2019RG000654.

McClain, C. R., 2009: A decade of satellite ocean color observations. *Annu. Rev. Mar. Sci.*, **1**, 19–42, https://doi.org/10.1146/annurev.marine.010908.163650.

Meinen, C. S., and Coauthors, 2013: Temporal variability of the meridional overturning circulation at 34.5°S: Results from two pilot boundary arrays in the South Atlantic. *J. Geophys. Res. Oceans*, **118**, 6461–6478, https://doi.org/10.1002/2013JC009228.

——, and Coauthors, 2018: Meridional overturning circulation transport variability at 34.5°S during 2009–2017: Baroclinic and barotropic flows and the dueling influence of the boundaries. *Geophys. Res. Lett.*, **45**, 4180–4188, https://doi.org/10.1029/2018GL077408.

——, R. H. Smith, and R. F. Garcia, 2021: Evaluating pressure gauges as a potential future replacement for electromagnetic cable observations of the Florida Current transport at 27°N. *J. Oper. Oceanogr.*, 14, 166–176, https://doi.org/10.1080/1755876X.2020.1780757.

Merrifield, M., 2011: A shift in western tropical Pacific sea level trends during the 1990s. *J. Climate*, **24**, 4126–4138, https://doi.org/10.1175/2011JCLI3932.1.

Midorikawa, T., and Coauthors, 2010: Decreasing pH trend estimated from 25-yr time-series of carbonate parameters in the western North Pacific. *Tellus*, **62B**, 649–659, https://doi.org/10.1111/j.1600-0889.2010.00474.x.

Moat, B. I., and Coauthors, 2020a: Pending recovery in the strength of the meridional overturning circulation at 26°N. *Ocean Sci.*, **16**, 863–874, https://doi.org/10.5194/os-16-863-2020.

——, and Coauthors, 2020b: Atlantic meridional overturning circulation observed by the RAPID-MOCHA-WBTS (RAPID-Meridional Overturning Circulation and Heatflux Array-Western Boundary Time Series) array at 26N from 2004 to 2018 (v2018.2). British Oceanographic Data Centre, National Oceanography Centre, accessed 29 January 2021, https://doi.org/10/d3z4.

Nagura, M., and M. J. McPhaden, 2010: Wyrtki jet dynamics: Seasonal variability. *J. Geophys. Res.*, **115**, C07009, https://doi.org/10.1029/2009JC005922.

Nerem, R. S., B. D. Beckley, J. T. Fasullo, B. D. Hamlington, D. Masters, and G. T. Mitchum, 2018: Climate-change-driven accelerated sea-level rise detected in the altimeter era. *Proc. Natl. Acad. Sci. USA*, **115**, 2022–2025, https://doi.org/10.1073/pnas.1717312115.

NOAA, 2019: New marine heatwave emerges off West Coast, resembles "the Blob." NOAA, accessed 11 February 2021, www.fisheries.noaa.gov/feature-story/new-marine-heatwave-emerges-west-coast-resembles-blob.

——, 2020: String of marine heatwaves continues to dominate Northeast Pacific. NOAA, accessed 11 February 2021, www.fisheries.noaa.gov/feature-story/string-marine-heatwaves-continues-dominate-northeast-pacific.

Oliver, E. C. J., 2019: Mean warming not variability drives marine heatwave trends. *Climate Dyn.*, **53**, 1653–1659, https://doi.org/10.1007/s00382-019-04707-2.

——, J. A. Benthuysen, N. L. Bindoff, A. J. Hobday, N. J. Holbrook, C. N. Mundy, and S. E. Perkins-Kirkpatrick, 2017: The unprecedented 2015/16 Tasman Sea marine heatwave. *Nat. Commun.*, **8**, 16101 https://doi.org/10.1038/ncomms16101.

Olsen, A., and Coauthors, 2016: The Global Ocean Data Analysis Project version 2 (GLODAPv2) – An internally consistent data product for the world ocean. *Earth Syst. Sci. Data*, **8**, 297–323, https://doi.org/10.5194/essd-8-297-2016.

——, and Coauthors, 2020: An updated version of the global interior ocean biogeochemical data product, GLODAPv2.2020. *Earth Syst. Sci. Data*, **12**, 3653–3678, https://doi.org/10.5194/essd-12-3653-2020.

Ono, H., and Coauthors, 2019: Acceleration of ocean acidification in the western North Pacific. *Geophys. Res. Lett.*, **46**, 13 161–13 169, https://doi.org/10.1029/2019GL085121.

Palmer, M. D., K. Haines, S. F. B. Tett, and T. J. Ansell, 2007: Isolating the signal of ocean global warming. *Geophys. Res. Lett.*, **34**, L23610, https://doi.org/10.1029/2007GL031712.

Perkins-Kirkpatrick, S. E., A. D. King, E. A. Cougnon, N. J. Holbrook, M. R. Grose, E. C. J. Oliver, S. C. Lewis, and F. Pourasghar, 2019: The role of natural variability and anthropogenic climate change in the 2017/18 Tasman Sea marine heatwave. *Bull. Amer. Meteor. Soc.*, **100**, S105–S110, https://doi.org/10.1175/BAMS-D-18-0116.1.

Pond, S., and G. L. Pickard, 1983: *Introductory Dynamical Oceanography*. 2nd ed. Pergamon Press, 349 pp.

Purkey, S. G., and G. C. Johnson, 2010: Warming of global abyssal and deep Southern Ocean waters between the 1990s and 2000s: Contributions to global heat and sea level rise budgets. *J. Climate*, **23**, 6336–6351, https://doi.org/10.1175/2010JCLI3682.1.

Qiu, B., and S. Chen, 2005: Variability of the Kuroshio extension jet, recirculation gyre, and mesoscale eddies on decadal time scales. *J. Phys. Oceanogr.*, **35**, 2090–2103, https://doi.org/10.1175/JPO2807.1.

Qu, T., S. Gao, and I. Fukumori, 2011: What governs the sea surface salinity maximum in the North Atlantic? *Geophys. Res. Lett.*, **38**, L07602, https://doi.org/10.1029/2011GL046757.

Reagan, J., T. Boyer, C. Schmid, and R. Locarnini, 2019: Subsurface salinity [in "State of the Climate in 2018"]. *Bull. Amer. Meteor. Soc.*, **100** (9), S79–S81, https://doi.org/10.1175/2019BAMSStateoftheClimate.1.

——, ——, ——, and ——, 2020: Subsurface salinity [in "State of the Climate in 2019"] . *Bull. Amer. Meteor. Soc.*, **101** (8), S144–S148, https://doi.org/10.1175/2020BAMSStateoftheClimate.1.

Ren, L., K. Speer, and E. P. Chassignet, 2011: The mixed layer salinity budget and sea ice in the Southern Ocean. *J. Geophys. Res.*, **116**, C08031, https://doi.org/10.1029/2010JC006634.

Resplandy, L., and Coauthors, 2018: Revision of global carbon fluxes based on a reassessment of oceanic and riverine carbon transport. *Nat. Geosci.*, **11**, 504–509, https://doi.org/10.1038/s41561-018-0151-3.

Rhein, M., and Coauthors, 2013: Observations: Ocean. *Climate Change 2013: The Physical Science Basis*, T. F. Stocker et al., Eds., Cambridge University Press, 255–315

Riser, S. C., and Coauthors, 2016: Fifteen years of ocean observations with the global Argo array. *Nat. Climate Change*, **6**, 145–153, https://doi.org/10.1038/nclimate2872.

Rödenbeck, C., and Coauthors, 2015: Data-based estimates of the ocean carbon sink variability—First results of the Surface Ocean pCO2 Mapping intercomparison (SOCOM). *Biogeosciences*, **12**, 7251–7278, https://doi.org/10.5194/bg-12-7251-2015.

Roemmich, D., and J. Gilson, 2009: The 2004–2008 mean and annual cycle of temperature, salinity, and steric height in the global ocean from the Argo Program. *Prog. Oceanogr.*, **82**, 81–100, https://doi.org/10.1016/j.pocean.2009.03.004.

——, and ——, 2011: The global ocean imprint of ENSO. *Geophys. Res. Lett.*, **38**, L13606, https://doi.org/10.1029/2011GL047992.

Saji, N. H., B. N. Goswami, P. N. Vinayachandran, and T. Yamagata, 1999: A dipole mode in the tropical Indian Ocean. *Nature*, **401**, 360–363, https://doi.org/10.1038/43854.

Sanchez-Franks, A., E. Frajka-Williams, B. I. Moat, and D. A. Smeed, 2021: A dynamically based method for estimating the Atlantic overturning circulation at 26° N from satellite altimetry. *Ocean Sci. Discuss*, https://doi.org/10.5194/os-2021-10.

Scannell, H. A., A. J. Pershing, M. A. Alexander, A. C. Thomas, and K. E. Mills, 2016: Frequency of marine heatwaves in the North Atlantic and North Pacific since 1950. *Geophys. Res. Lett.*, **43**, 2069–2076, https://doi.org/10.1002/2015GL067308.

——, G. C. Johnson, L. Thompson, J. M. Lyman, and S. C. Riser, 2020: Subsurface evolution and persistence of marine heatwaves in the Northeast Pacific. *Geophys. Res. Lett.*, **47**, e2020GL090548, https://doi.org/10.1029/2020GL090548.

Schlesinger, M. E., and N. Ramankutty, 1994: An oscillation in the global climate system of period 65–70 years. *Nature*, **367**, 723–726, https://doi.org/10.1038/367723a0.

Schmidtko, S., K. J. Heywood, A. F. Thompson, and S. Aoki, 2014: Multidecadal warming of Antarctic waters. *Science*, **346**, 1227–1231, https://doi.org/10.1126/science.1256117.

Schmitt, R. W., 1995: The ocean component of the global water cycle. *Rev. Geophys.*, **33**, 1395–1409, https://doi.org/10.1029/95RG00184.

——, 2008: Salinity and the global water cycle. *Oceanography*, **21**, 12–19, https://doi.org/10.5670/oceanog.2008.63.

Siegel, D. A., S. Maritorena, N. B. Nelson, M. J. Behrenfeld, and C. R. McClain, 2005: Colored dissolved organic matter and its influence on the satellite-based characterization of the ocean biosphere. *Geophys. Res. Lett.*, **32**, L20605, https://doi.org/10.1029/2005GL024310.

——, and Coauthors, 2013: Regional to global assessments of phytoplankton dynamics from the SeaWiFS mission. *Remote Sens. Environ.*, **135**, 77–91, https://doi.org/10.1016/j.rse.2013.03.025.

Skliris, N., R. Marsh, S. A. Josey, S. A. Good, C. Liu, and R. P. Allan, 2014: Salinity changes in the World Ocean since 1950 in relation to changing surface freshwater flux. *Climate Dyn.*, **43**, 709–736, https://doi.org/10.1007/s00382-014-2131-7.

Smale, D. A., and Coauthors, 2019: Marine heatwaves threaten global biodiversity and the provision of ecosystem services. *Nat. Climate Change*, **9**, 302–312, https://doi.org/10.1038/s41558-019-0412-1.

Stackhouse, P. W., D. P. Kratz, G. R. McGarragh, S. K. Gupta, and E. B. Geier, 2006: Fast longwave and shortwave radiative flux (FLASHFlux) products from CERES and MODIS measurements. 12th Conf. on Atmospheric Radiation, Amer. Meteor. Soc., Madison, WI, P1.10, https://ams.confex.com/ams/Madison2006/techprogram/paper_113479.htm.

Sutton, A. J., and Coauthors, 2019: Autonomous seawater pCO2 and pH time series from 40 surface buoys and the emergence of anthropogenic trends. *Earth Syst. Sci. Data*, **11**, 421–439, https://doi.org/10.5194/essd-11-421-2019.

Sweet, W.V., J. Park, J. J. Marra, C. Zervas, and S. Gill, 2014: Sea level rise and nuisance flood frequency changes around the United States. NOAA Tech. Rep. NOS CO-OPS 073, 58 pp., https://tidesandcurrents.noaa.gov/publications/NOAA_Technical_Report_NOS_COOPS_073.pdf.

Takahashi, T., and Coauthors, 2009: Climatological mean and decadal change in surface ocean pCO2, and net sea-air CO2 flux over the global oceans. *Deep-Sea Res. II*, **56**, 554–577, https://doi.org/10.1016/j.dsr2.2008.12.009.

——, S. C. Sutherland, D. W. Chipman, J. G. Goddard, C. Ho, T. Newberger, C. Sweeney, and D. R. Munro, 2014: Climatological distributions of pH, pCO2, total CO2, alkalinity, and CaCO3 saturation in the global surface ocean, and temporal changes at selected locations. *Mar. Chem.*, **164**, 95–125, https://doi.org/10.1016/j.marchem.2014.06.004.

——, ——, and A. Kozyr, 2020: Global ocean surface water partial pressure of CO2 database: Measurements performed during 1957–2019 (LDEO database version 2019) (NCEI accession 0160492). Version 9.9, NOAA National Centers for Environmental Information, accessed 17 December 2020, https://doi.org/10.3334/CDIAC/OTG.NDP088(V2015).

van Heuven, S., D. Pierrot, J. W. B. Rae, E. Lewis, and D. W. R. Wallace, 2011: MATLAB program developed for CO2 system calculations. ORNL/CDIAC-105b. Carbon dioxide Information Analysis Center, Oak Ridge National Laboratory, accessed 25 September 2014, https://doi.org/10.3334/CDIAC/otg.CO2SYS_MATLAB_v1.1.

Volkov, D. L., S.-K. Lee, F. W. Landerer, and R. Lumpkin, 2017: Decade-long deep-ocean warming detected in the subtropical South Pacific. *Geophys. Res. Lett.*, **44**, 927–936, https://doi.org/10.1002/2016GL071661.

——, R. Domingues, C. S. Meinen, R. Garcia, M. Baringer, G. Goni, and R. H. Smith, 2020a: Inferring Florida current volume transport from satellite altimetry. *J. Geophys. Res. Oceans*, **125**, e2020JC016763, https://doi.org/10.1029/2020JC016763.

——, and Coauthors, 2020b: Atlantic meridional overturning circulation and associated heat transport [in "State of the Climate 2019"]. *Bull. Amer. Meteor. Soc.*, **101** (8), S159–S163, https://doi.org/10.1175/2020BAMSStateoftheClimate.1.

Von Storch, H., and F. W. Zwiers, 1999: *Statistical Analysis in Climate Research*. Cambridge University Press, 484 pp.

Wallace, J. M., and D. S. Gutzler, 1981: Teleconnections in the geopotential height field during the Northern Hemisphere Winter. *Mon. Wea. Rev.*, **109**, 784–812, https://doi.org/10.1175/1520-0493(1981)109<0784:TITGHF>2.0.CO;2.

Wang, J., and B. Yang, 2017: Internal and external forcing of multidecadal Atlantic climate variability over the past 1,200 years. *Nat. Geosci.*, **10**, 512–517, https://doi.org/10.1038/ngeo2962.

Wanninkhof, R., 2014: Relationship between wind speed and gas exchange over the ocean revisited. *Limnol. Oceanogr. Methods*, **12**, 351–362, https://doi.org/10.4319/lom.2014.12.351.

——, and Coauthors, 2013: Global ocean carbon uptake: Magnitude, variability, and trends. *Biogeosciences*, **10**, 1983–2000, https://doi.org/10.5194/bg-10-1983-2013.

WCRP Global Sea Level Budget Group, 2018: Global sea-level budget 1993–present. *Earth Syst. Sci. Data*, **10**, 1551–1590, https://doi.org/10.5194/essd-10-1551-2018.

Werdell, P. J., and Coauthors, 2013: Generalized ocean color inversion model for retrieving marine inherent optical properties. *Appl. Opt.*, **52**, 2019–2037, https://doi.org/10.1364/AO.52.002019.

——, and Coauthors, 2019: The Plankton, Aerosol, Cloud, Ocean Ecosystem mission: Status, science, advances. *Bull. Amer. Meteor. Soc.*, **100**, 1775–1794, https://doi.org/10.1175/BAMS-D-18-0056.1.

Westberry, T. K., and Coauthors, 2016: Annual cycles of phytoplankton biomass in the subarctic Atlantic and Pacific Ocean. *Global Biogeochem. Cycles*, **30**, 175–190, https://doi.org/10.1002/2015GB005276.

Widlansky, M. J., X. Long, and F. Schloesser, 2020: Increase in sea level variability with ocean warming associated with the nonlinear thermal expansion of seawater. *Commun. Earth Environ.*, **1**, 9, https://doi.org/10.1038/s43247-020-0008-8.

Willis, J. K., D. Roemmich, and B. Cornuelle, 2004: Interannual variability in upper ocean heat content, temperature, and thermosteric expansion on global scales. *J. Geophys. Res.*, **109**, C12036, https://doi.org/10.1029/2003JC002260.

Wolter, K., and M. S. Timlin, 1998: Measuring the strength of ENSO events: How does 1997/98 rank? *Weather*, **53**, 315–324, https://doi.org/10.1002/j.1477-8696.1998.tb06408.x.

Wu, L. X., and Coauthors, 2012: Enhanced warming over the global subtropical western boundary currents. *Nat. Climate Change*, **2**, 161–166, https://doi.org/10.1038/nclimate1353.

Wüst, G., 1936: Oberflächensalzgehalt, Verdunstung und Niederschlag auf dem Weltmeere. Länderkundliche Forschung: Festschrift zur Vollendung des sechzigsten Lebensjahres Norbert Krebs, J. Engelhorns Nachfahren, 347–359.

Xie, P., and Coauthors, 2014: An in situ-satellite blended analysis of global sea surface salinity. *J. Geophys. Res. Oceans*, **119**, 6140–6160, https://doi.org/10.1002/2014JC010046.

Yu, L., and R. A. Weller, 2007: Objectively analyzed air–sea heat fluxes for the global ice-free oceans (1981–2005). *Bull. Amer. Meteor. Soc.*, **88**, 527–540, https://doi.org/10.1175/BAMS-88-4-527.

——, X. Jin, P. W. Stackhouse, A. C. Wilber, S. Kato, N. G. Loeb, and R. A. Weller, 2019: Global ocean heat, freshwater, and momentum fluxes [in "State of the Climate in 2018"]. *Bull. Amer. Meteor. Soc.*, **100** (9), S81–S84, https://doi.org/10.1175/2019BAMSStateoftheClimate.1.

Zebiak, S. E., 1993: Air–sea interaction in the Equatorial Atlantic region. *J. Climate*, **6**, 1567–1568, https://doi.org/10.1175/1520-0442(1993)006<1567:AIITEA>2.0.CO;2.

Zhang, R., and Coauthors, 2019: A review of the role of the Atlantic meridional overturning circulation in Atlantic multidecadal variability and associated climate impacts. *Rev. Geophys.*, **57**, 316–375, https://doi.org/10.1029/2019RG000644.

Zweng, M. M., and Coauthors, 2013: Salinity. Vol. 2, World Ocean Atlas 2013, NOAA Atlas NESDIS 74, 39 pp., http://data.nodc.noaa.gov/woa/WOA13/DOC/woa13_vol2.pdf.